Title
Excitatory Inputs to Starburst Amacrine Cells: Adaptation, Computations, Development

Author
Vlasits, Anna Louise

Publication Date
2017

Peer reviewed|Thesis/dissertation

Excitatory Inputs to Starburst Amacrine Cells: Adaptation, Computations, Development

by

Anna Louise Vlasits

A dissertation submitted in partial satisfaction of the
requirements for the degree of
Doctor of Philosophy

in

Neuroscience

in the

Graduate Division

of the

University of California, Berkeley

Committee in charge:

Professor Marla B. Feller, Chair
Professor Ehud Y. Isacoff
Professor Hillel Adesnik
Professor Polina V. Lishko

Spring 2017

Excitatory Inputs to Starburst Amacrine Cells: Adaptation, Computations, Development

Abstract

Excitatory Inputs to Starburst Amacrine Cells: Adaptation, Computations, Development

by

Anna Louise Vlasits

Doctor of Philosophy in Neuroscience

University of California, Berkeley

Professor Marla B. Feller, Chair

The retina in our eyes is full of tiny neuronal computers, cells with diversely elaborate dendritic arbors that transform, sort, and integrate information about light bouncing off of objects in the world. The focus of this dissertation was to understand how dendrites of one type of cell in the retina, called the starburst amacrine cell, perform computations on visual information. The starburst amacrine cell is a part of the retina's "direction selective circuit", a model system for studying the cellular and synaptic implementation of a neural computation. Within this circuit, the starburst amacrine cells are responsible for detecting the direction of motion in the environment—right, left, up, or down—and cueing downstream cells, which pass on this information about motion direction to the brain. To begin, Chapter I presents the recent advances in our understanding of how the direction selective circuit works. Then, the experimental investigations presented in this dissertation attempt to clarify three issues about starburst amacrine cells. First, I examined the precise role of starburst amacrine cells in the direction selective circuit by altering their response properties and investigating how the performance of the circuit changes (Chapter II). I found that perturbations to the excitatory inputs to starburst amacrine cells using either visual adaptation of the retina or a chemo-genetic manipulation substantially altered the computational output of the entire circuit. Second, I described how the cells' excitatory synaptic inputs are organized and contribute to the cells' computations (Chapter III). I discovered that the precise distribution of excitatory inputs to the starburst amacrine cells shapes the cells' ability to detect motion direction. Because of the elaborate structure of the dendrites, this precise arrangement is necessary for the electrical signals coming at different times and onto different dendritic locations to be integrated together in a direction-dependent fashion. Third, I investigated the development of the excitatory inputs to starburst amacrine cells and starburst amacrine cells' velocity tuning (Chapter IV). These preliminary experiments provide a framework for further inquiry in these areas. Together, these experiments reveal how anatomical wiring and electrical properties of neurons in the retina produce exquisite computational abilities.

For my family and for you

Contents

List of Figures

List of Tables

Acknowledgements

Science is never the act of a single person. Many scientists, family members, friends, and American and French taxpayers contributed to the work presented here.

For Chapter I, I am grateful to my coauthors Alex Mauss, Axel Borst, and Marla Feller for a clarifying and fruitful melding of the mouse and fly literature on direction selectivity.

For Chapter II, I want first to acknowledge my coauthors Michal Rivlin-Etzion, Marla Feller, Remi Bos, Ryan Morrie, Cecile Fortuny and John Flannery. They all contributed extensively to this confounding set of results. In particular, Michal did the foundational work that prompted this study and was by my side for the experiments and analysis. She is a role model of tenacity in the face of the unexpected. In addition, we thank Scott Sternson (Janelia Farms) for the generous gift of PSEM ligand. This work was supported by grants NIH RO1EY019498, RO1EY013528, and P30EY003176, National Science Foundation Grant No. DGE 1106400, NIH/NEI 1R01EY022975, the Foundation Fighting Blindness, USA, the Human Frontier Science Program Organization, the National Postdoctoral Award Program for Advancing Women in Science, and NIH NRSA grant T32 GM 007232.

For Chapter III, I am extremely grateful to my coauthors Ryan Morrie, Alex Tran-Van-Minh, Adam Bleckert, Christian Gainer, David DiGregorio, and Marla Feller. This paper represented a true international collaboration between multiple labs and could not have been accomplished without each of these people. First, I was extremely lucky to be welcomed into the DiGregorio Lab at Institut Pasteur in Paris by David and his lab members, especially Alex, whose curiosity and scientific rigor made me a better scientist. Second, I am grateful to Adam Bleckert, whose insistence on quantitative rigor made the paper more precise. Third, I want to thank Ryan and Chris for helping me do incredible, challenging experiments when I was at my most vulnerable, physically and emotionally. I would not have finished this without you. In addition, I am grateful to Kevin Briggman for providing previously published SBEM data, members of the Feller Lab and DiGregorio lab for discussion and technical support, Rachel Wong for helpful comments on the manuscript and Melissa Panlasigui for microscopy support. Members of the team were supported by the following government and private funding sources: NSF Grant No. DGE 1106400, NIH F31 NS089197-01, ROI1EY019498, RO1EY013528, P30EY003176, and EY10699, the French National Agency for Research (ANR-2010-BLANC-1411, ANR-13-SAMA-0006-05, ANR-13-BSV4-0016), the Fondation de Recherche Medicale (Team grant), the Ecole des Neurosciences de Paris, EMBO Long-Term Fellowship 1582-2011, a Roux-Howard-Cantarini post-doctoral fellowship, a Marie Curie Individual Fellowship 301362 within the 7th European Community Framework Program (FP7-PEOPLE-2011-IEF), NIH P30EY003176, and last but not least, the France-Berkeley Fund.

For Chapter IV, Ryan B. Morrie, Alexandra Tran-Van-Minh, Vasha DuTell, David A. DiGregorio, and Marla B. Feller conceptualized and performed these experiments with me. We received support from NSF Grant DGE 1106400, NIH F31 NS089197-01, NIH ROI1EY019498, NIH RO1EY013528, P30EY003176, NIH EY10699, ANR-2010-BLANC-1411, ANR-13-SAMA- 0006-05, ANR-13-BSV4-0016, Fondation de Recherche Medicale (Team grant), Ecole des Neurosciences de Paris, EMBO Long-Term Fellowship 1582-2011, Roux-Howard-Cantarini

post-doctoral fellowship, Marie Curie Individual Fellowship 301362, and the France Berkeley Fund.

The common factor among all of these chapters is my advisor Marla Feller. Thank you for the gift of a dissertation of which I am proud.

Many other intellectuals at UC Berkeley and elsewhere contributed to this journey. My Feller Lab mates: Georgeann Sack, Michal Rivlin, Alana Firl, Lowry Kirkby, Juli Rosa, Remi Bos, David Arroyo, Paley Han, Alex Tiriac, Mathew Summers, Ryan Morrie, Melanie Lee, Malak El Quessny, and Franklin Caval-Holme. My qualifying exam and committee members Hillel Adesnik, Udi Isacoff, Polina Lishko, and Yang Dan. The professors who taught my classes. My graduate school cohort. The post-docs I worked with during rotations. The scientists at Cold Spring Harbor. The many post-docs and graduate students who asked amazing questions at conferences, Brain Lunch, and seminars. The members of the UC Berkeley philosophy department who question all assumptions. Thank you for making this community diverse and challenging. I wouldn't have wanted it any other way.

I want to thank my family: Glenda, Nate, Mike, Ellen, Joanne, George, and David for your kindness, patience, and support while Justin and I went to graduate school and had a baby at the same time. In particular, thank you to my mother Glenda for emotional support and for taking care of Arthur for thousands of hours while this work was completed.

Last and most, thank you to my husband Justin, for giving more than you receive.

Chapter I

The Mammalian Circuit for Direction Selectivity

This Chapter is a selection from Mauss et al., *Ann. Rev. Neurosci.* (2017), in which I was co-primary author. The original review paper discusses recent progress in understanding direction selectivity in flies and mammals. I have included the sections about mammals, which are relevant to this thesis. The work is included with permission from all authors.

Relevant publication:

Mauss, A., Vlasits A., Borst A., Feller M. (2017) Visual Circuits for Direction Selectivity. Annu. Rev. Neurosci. *In press.*

Abstract

Images projected onto the retina of an animal eye are rarely still. Instead, they usually contain motion signals originating either from moving objects or from retinal slip caused by self-motion. Accordingly, motion signals tell the animal in which direction a predator, prey, or the animal itself is moving. At the neural level, visual motion detection has been proposed to extract directional information by a delay-and-compare mechanism, representing a classic example of neural computation. Neurons responding selectively to motion in one but not in the other direction have been identified in many systems, including in the mammalian retina. Technological advances have now allowed researchers to characterize these neurons' upstream circuits in exquisite detail. Focusing on these upstream circuits, we review recent progress in understanding the mechanisms that generate direction selectivity in the early visual system of mammals.

Introduction

Neurons that signal the direction of visual motion are pervasive in animals that see and have been the focus of neuroscience research for over 100 years (Exner, 1894). Such neurons were first recorded in primary visual cortex of the awake cat by David Hubel (1959) and are considered a basic computational unit of cortex of all mammalian species, including primate (Livingstone & Hubel, 1988, Priebe & Ferster, 2008). Direction-selective cells can also be found earlier in visual processing 2-3 synapses downstream of photoreceptors. Their contribution to cortical processing is yet unclear (Cruz-Martin, et al. 2014). However, due to their experimental accessibility such early direction-selective neurons hold great promise to reach a comprehensive understanding of the fundamental cellular mechanisms underlying visual motion detection.

Direction-selective ganglion cells (DSGCs) in the mammalian retina were first observed more than 50 years ago in rabbit, and encode the direction of motion in their spiking patterns (Fig. 1.1A) (Barlow & Hill, 1963). DSGCs have been extensively studied in mouse and in rabbit, where they comprise a large percentage of retinal ganglion cells. Regardless of the animal, neurons with different directional preferences receive signals from the same array of photoreceptors. Therefore, directional information must be computed in the interjacent circuits.

Because visual motion involves the displacement of brightness profiles across a retina over time, both spatial and temporal information must be encoded (Fig. 1.1B). To detect the sequence of photoreceptor activation, signals need to be compared across space and time. Two simple models have been conceived for how neurons generate direction-selective output, both of which are based on a delay-and-compare mechanism (Fig. 1.1C). First, delays between neighboring inputs, when activated in sequence during motion, are reduced by an asymmetric filtering operation (t). Next, coincidence is detected through a nonlinear processing step: In one model, one signal is enhanced by the other (Hassenstein & Reichardt, 1956), and in the other model, it is suppressed by the other (Barlow & Levick, 1965). The site of the relative temporal delay (in visual space) and the nature of the nonlinearity determine the directional preference of the detector. In order to understand visual motion detection at the cellular level, three issues need to be addressed: 1) Which is the underlying algorithm endowing neurons with direction selectivity (Fig. 1.1C)? 2) Where and how do the asymmetric filtering operations take place (Fig. 1.1D)? 3) How are asymmetrically filtered signals integrated in a non-linear way?

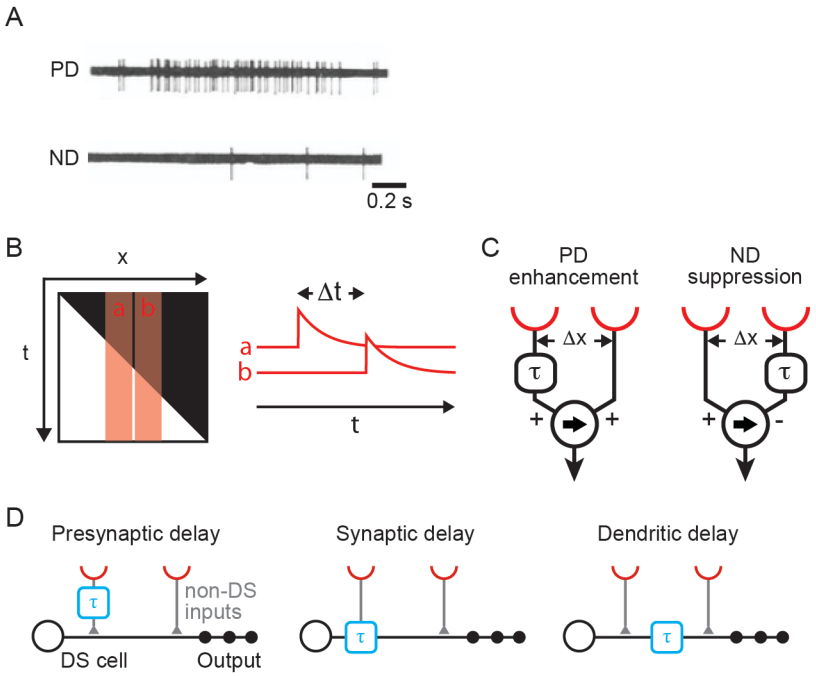

Figure 1.1 **Cells and models for visual motion detection.** (A) Spiking response of a direction-selective unit in the rabbit retina to a moving light spot. Panel adapted with permission from Barlow and Levick (1965). (B) The brightness profile of a light edge moving to the right shown in space-time (x-t). a and b represent the receptive fields of two adjacent photoreceptors, which are activated sequentially with a delay Dt. The traces a and b depict a high-pass-filtered version of a signal, highlighting illumination changes. (C) Two alternative motion detector models. Both generate direction-selective responses by a delay-and-compare mechanism but differ in their nonlinear integration. In the Hassenstein-Reichardt model on the left, a delayed signal (denoted by t) enhances a direct signal, for instance by a multiplication. In the Barlow-Levick model on the right, a delayed signal suppresses a direct signal, for instance by a division. In both models, the arrow indicates the preferred direction. (D) Potential cellular implementations of local motion detection (not mutually exclusive). Spatially offset signals are conveyed through different cell types or different synaptic receptors with different dynamics (left and middle, respectively). Temporal delays might also arise by dendritic filtering (right). Note that "presynaptic delay" could be generated by an arbitrary mechanism in the upstream circuit. Abbreviations: DS, direction-selective; ND, null-direction; PD, preferred-direction.

The mammalian retina has been studied extensively in this context. Across species of animals, many design principles are shared, such as a retinotopic representation of visual space intersected by synaptic laminae and horizontal connections (Sanes & Zipursky, 2010). Signals from each point in visual space are processed in parallel channels---for instance, for increments and decrements of light separately (Borst & Helmstaedter, 2015)---forming the basis for visual feature extraction. Historically, the underlying mechanism for direction selectivity in DSGCs in mammals was suggested to involve null-direction suppression at the level of DSGCs, with spatially offset inhibitory suppression of excitation establishing the null-direction (Barlow & Levick, 1965). Despite decades of research, the neuronal and synaptic underpinnings of this model are still not fully understood. Here, focusing on the mouse and rabbit, we review recent surprising findings about the circuits and mechanisms leading to direction selectivity in the mammalian visual system.

Integration of Excitation and Inhibition in Direction-Selective Ganglion Cells

DSGCs fall into two main classes, ON and ON-OFF, which respond to light increments or both increments and decrements, respectively. DSGCs receive excitatory inputs from glutamatergic bipolar cells, which themselves receive their primary inputs from cones. DSGCs also receive inhibitory and excitatory input from a class of interneurons called starburst amacrine cells (SACs) (Fig. 1.2A). The SAC is radially symmetric, GABAergic, and cholinergic, with dendrites stratifying in either the OFF or ON layer of the inner plexiform layer (Fig. 1.2B). Recent research has led to several hypotheses of how directional information is computed in the retina. As originally conceived by Barlow and Levick (1965), direction selectivity may arise in the ganglion cell itself, though not necessarily by their postulated mechanism. Furthermore, it has become clear that direction selectivity also emerges at the level of SACs which in turn convey direction-selective inhibition to DSGCs. Evidence now suggests that several of these mechanisms may function in parallel, under different stimulus conditions, or both. Here, we review evidence for these different mechanisms at the level of the DSGC and then examine closely the presynaptic mechanisms in SACs and bipolar cells.

In the main model of how DSGCs integrate their inputs to produce direction-selective firing, during null side stimulation, the inhibition from SACs provides a strong shunt of excitation from bipolar cells and thus prevents spiking. This shunting process during null stimulation relies on the relative timing of excitatory and inhibitory inputs (as in the Barlow-Levick model) (Fig. 1.1C, right) as well as the strength or direction selectivity of the inhibitory inputs. Active properties of the DSGC dendrites are thought to further enhance direction selectivity.

The relative importance of the input timing versus input strength mechanism likely depends on features of the stimulus, such as spatial frequency (Lipin et al., 2015). Input timing appears crucial to direction-selective tuning of DSGCs at low contrast (when cholinergic signaling dominates), as GABAergic currents lag cholinergic currents significantly in the preferred-direction (Sethuramanujam et al., 2016). Two recent studies altered the relative timing of excitation and inhibition onto DSGCs, which resulted in DSGCs being tuned to motion in what was originally their null-direction (Rivlin-Etzion et al., 2012, Vlasits et al., 2014). Whether these circuit dynamics are used endogenously remains to be determined but could underlie adaptation to motion stimuli such as described by Masland (1969).

DSGCs respond in a direction-selective manner across many orders of magnitude of light intensity. Thus, maintaining a balance between the strength of excitation and inhibition for a given motion direction across this stimulus space is important for the direction selectivity. This was recently shown in studies that explored DSGC spiking as a function of stimulus contrast. Poleg-Polsky & Diamond (2016a) showed that the excitatory inputs to SACs have higher contrast sensitivity than the excitatory inputs to DSGCs, leading to apparently matched contrast sensitivity after the SAC dendrite's nonlinearity. Rabbit and guinea pig use another strategy: SACs have a low contrast threshold for activation and saturate at high contrast (Lipin et al., 2015). These properties lead to E-I imbalances at high contrast and therefore a preference for medium contrast—an example of a species difference that may relate to differences in the ratio of nocturnal to diurnal behavior.

In addition to the role of synaptic input timing and strength, several active properties of DSGC dendrites enhance the difference between preferred- and null-direction firing. In rabbit, recordings of dendritic spikes from rabbit DSGCs revealed that DSGCs have active, voltage-

gated sodium conductances necessary for sharp directional tuning (Oesch et al., 2005). Current clamp recordings directly from the dendrites of rabbit DSGCs confirmed the presence of dendritic sodium spikes and demonstrated that excitation and inhibition compete locally within the dendrites, with GABAergic inputs capable of silencing dendritic spikes (Sivyer & Williams, 2013). Thus, at the level of the dendrite, the absence of spiking during null-direction stimulation likely results from suppression of dendritic spikes by GABA receptors opening in DSGC dendrites.

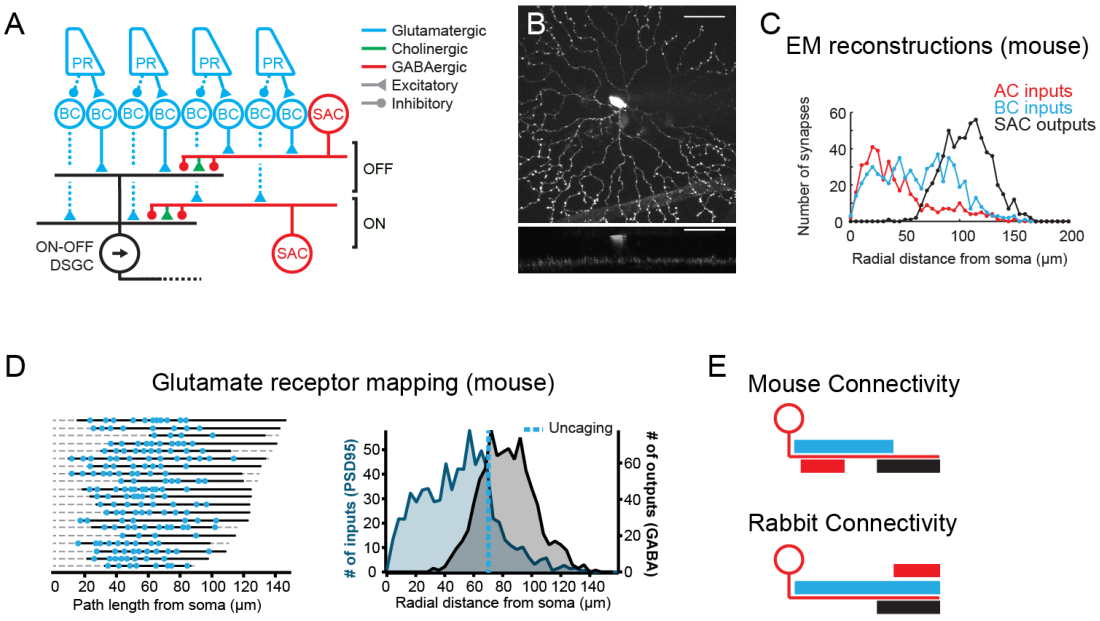

Figure 1.2 **Visual motion detection in the mammalian retina.** (A) Schematic of the mammalian retinal circuit elements for direction selectivity. Photoreceptor signals are split into an ON and an OFF pathway at the level of bipolar cells via different glutamate receptors. ON and OFF bipolar cells synapse individually onto direction-selective ON and OFF SACs, respectively, and jointly onto ON-OFF DSGCs. DSGC receive additional asymmetric GABAergic and symmetric cholinergic input from SACs. Note that only selected aspects of the connectivity are captured in this simplified schematic. (B) A z-projection of an ON SAC filled with a fluorescent dye showing the radial dendrites and stratification. (C) Distribution of inputs and outputs determined by serial electron microscopy reconstructions of mouse ON SACs as well as their pre- and postsynaptic partners. Panel adapted with permission from Ding et al. (2016). (D) (left) Distributions of glutamatergic inputs on SAC dendrites determined using glutamate uncaging. Each row is a different SAC dendrite, the solid line is the mapped region of the dendrite, and blue dots are glutamatergic synapses as revealed by glutamate uncaging. (right) Comparison of glutamatergic inputs determined by labeling SACs with the postsynaptic marker for glutamatergic synapses, PSD95-YFP (blue) and outputs determined using serial electron microscopy reconstructions. The average location of the most distal synapse measured with uncaging is represented by the dotted line. Panel adapted with permission from Vlasits et al. (2016). (E) Schematic of dendritic locations of inputs (blue, bipolar cells; red, neighboring SACs) and outputs (black) in mouse and rabbit SACs. Abbreviations: AC, amacrine cell; BC, bipolar cell; DSGC, direction-selective ganglion cell; EM, electron microscopy; PR, photoreceptor; SAC, starburst amacrine cell.

N-methyl-D-aspartate (NMDA) receptors (NMDARs) are another active component of DSGC dendrites. In rabbit, NMDA is the primary glutamatergic conductance onto DSGCs and important for producing direction-selective tuning (Tjepkes & Amthor, 2000). In mouse, one

surprising finding is that NMDARs may be primed to open due to depolarization of the DSGC by acetylcholine receptor (AChR) activation in some stimulus conditions (Sethuramanujam, et al. 2016). Poleg-Polsky & Diamond (2016b) described a role for NMDARs in enhancing direction-selective signals: Local interactions between GABA receptors and voltage-dependent NMDARs lead to a balance between excitation and inhibition that aids DSGCs in maintaining directional tuning in noisy stimulus conditions.

Beyond active channels enhancing direction selectivity, one type of DSGC, the Hb9+ type, relies in part on asymmetric anatomy of its dendrites for selectivity (Trenholm et al., 2014). In addition to the usual SAC-mediated direction-selective tuning, the asymmetric dendrites confer direction-selective tuning at slow velocities by integrating excitatory inputs preferentially during motion stimulation in the preferred-direction---a putative Hassenstein-Reichardt motif. In addition, Hb9+ DSGCs are gap-junction coupled to one another. This syncytium of DSGCs leads to correlated firing in the Hb9+ DSGC population, a property that may enhance coding in ambiguous stimulus conditions.

The Emergence of Direction Selectivity in Starburst Amacrine Cells

The SAC's central role in the direction-selective circuit has been demonstrated unequivocally. Several studies have now shown that SACs provide the asymmetric inhibition that DSGCs use to produce direction-selective spiking, both through manipulations that perturb SAC development and morphology (Kostadinov & Sanes, 2015, Sun et al., 2013) and through manipulations that remove the SAC's participation in the circuit, either reversibly using pharmacogenetics (Vlasits et al., 2014) or irreversibly by killing SACs (Amthor et al., 2002, Yoshida et al., 2001). Thus, numerous recent studies have focused on the wiring and computational properties of SACs.

SACs have both inputs and outputs on their dendrites. They provide direction-selective inhibition to DSGCs through a combination of two properties. First, SAC release sites prefer stimuli moving outward from the soma toward the end of the dendrites (centrifugally) to motion inward toward the soma (centripetally), as first shown by Euler et al. (2002) through two-photon calcium imaging. Thus, quadrants of SAC dendrites behave like local motion detectors. Second, Briggman et al. (2011) used calcium imaging and electron microscopy (EM) to reveal that DSGCs receive inhibition predominantly from SAC dendrites pointing in their null-direction. For example, a nasally preferring DSGC receives more inputs from SAC dendrites pointing in the temporal direction. Thus, DSGCs receive inputs from SAC dendrites that have the largest influx of calcium during stimulation in a DSGC's null-direction, presumably providing the largest amount of GABA release to the null stimulus.

To understand how SAC dendrites accomplish direction detection, researchers have elucidated the specific connectivity of the mouse SACs' presynaptic partners. Dense EM reconstructions revealed the specific bipolar cell types that contact SAC dendrites (Ding et al., 2016, Kim et al., 2014). These EM reconstructions also showed that inputs from bipolar cells are excluded from the distal dendrites of mouse SACs (Fig. 1.2C), also observed as a shift in the distribution of a fluorescently labeled PSD95, a scaffolding protein that marks the location of excitatory synapses (Fig. 1.2D) (Vlasits et al., 2016). Functional mapping of excitatory inputs based on whole-cell recordings paired with either glutamate uncaging or light stimulation confirmed that the skewed distribution of receptors observed anatomically corresponds to a skewed distribution of functional receptors (Vlasits et al., 2016). EM reconstructions also described the inhibitory inputs to SACs, revealing that contacts from neighboring SACs occur in

the proximal third of the dendritic arbor (Fig. 1.2C) (Ding et al., 2016). The inhibition from SACs onto the proximal dendrites of neighboring SACs was functionally confirmed in a study that determined the intersoma distances of pairs of SACs (Kostadinov & Sanes, 2015).

Using this detailed connectivity pattern to create computer simulations of SAC dendrites, one can now describe how the distribution of synaptic inputs influences the direction selectivity of SAC dendrites. One simulation based entirely on excitatory inputs (Vlasits et al., 2016) suggests that direction selectivity across the release site region of the SAC dendrite is conferred by the high input-impedance of the narrow-diameter (approximately 200--300 nm) dendrites and the fact that the presynaptic release sites are located near the end of the dendrites, where the sealed end of the dendrite creates a high-resistance compartment. When excitatory inputs in this simulation are stimulated sequentially, summation is augmented for outward motion and the depolarization is consistent across the output region because of the spatial offset of the excitatory and inhibitory input regions.

However, this model does not appear to apply to rabbit SACs, which have excitatory inputs across the entire length of their dendrites (Fig. 1.2E) (Famiglietti, 1991; Koizumi et al., 2011; Lee & Zhou, 2006). This alternative was addressed by a second computer simulation that included inhibition onto SACs (Ding et al., 2016), which is confined to the proximal part of the SACs in mice and distributed more distally in rabbits. This second simulation suggests that both the mouse and the rabbit arrangements produce direction-selective responses and that the different arrangements might serve to optimize each animal's motion detection to different velocity ranges experienced on the retina as a direct consequence of these species' different eye diameters. Thus, throughout mammalian evolution, different solutions to the computation of direction in the SAC dendrites may have evolved.

Two papers have hypothesized an alternative mechanism for SAC direction selectivity based on bipolar cell release kinetics (Greene et al., 2016, Kim et al., 2014). As they radiate outward, SAC dendrites traverse different depths of the inner plexiform layer. EM studies indicate that the bipolar cells they contact reflect this change in depth: OFF SACs receive more contacts from bipolar cell types 1 and 2 near the soma and types 3a and 3b further from the soma; ON SACs receive more contacts from bipolar cell type 7 near the soma and from the several type 5s further from the soma. Because bipolar cells differ in the kinetics of their calcium transients and glutamate release (Baden et al., 2013, Borghuis et al., 2013), researchers have proposed they represent spatially offset and asymmetrically filtered inputs to SAC dendrites---a potential basis for preferred-direction enhancement (Fig. 1.1D, left). However, an additional EM reconstruction using conventional staining methods, allowing the identification of synapses, questioned the clear proximal versus distal delineation of the bipolar cell types (Ding et al., 2016). Furthermore, two papers have failed to find differences in excitatory input kinetics when stimulating proximal versus distal dendrites (Stincic et al., 2016, Vlasits et al., 2016). These data also argue against the possibility that delays are generated by synaptic receptors with different temporal properties in SACs (Fig. 1.1D, middle). Bipolar cell--SAC paired recordings will be needed to determine whether bipolar cell release or synaptic receptor kinetics play a role in the computation.

In addition to the excitatory inputs, researchers have debated the role of inhibition in shaping the direction-selective computation in SAC dendrites. First, we will review evidence for a role for inhibition in general, followed by the evidence of a role for mutual inhibition between SACs (SAC-SAC inhibition) specifically. Pharmacological results in rabbit showed that SACs lose direction selectivity in the absence of inhibition, suggesting that inhibition is necessary for

producing direction selectivity in their dendrites (Lee & Zhou, 2006). However, two studies in rabbit observed direction-selective responses in the absence of inhibition, suggesting that inhibition was not necessary for the computation at all (Euler et al., 2002, Hausselt et al., 2007). One possible explanation for the discrepancies in these experiments was suggested by Ding et al. (2016). They demonstrated that blocking inhibition in mouse reduces the direction-selective response to a high-contrast stimulus but has a more modest effect at low contrast. Thus, the importance of SAC-SAC inhibition in the direction-selective computation may depend heavily on stimulus conditions.

More recent experiments in mouse suggest that GABAergic inhibition plays a role in enhancing direction-selective responses. Blocking GABA pharmacologically greatly reduces the centrifugal preference of calcium responses in ON SAC dendrites, but some residual direction selectivity remains (Ding et al., 2016, Vlasits et al., 2016). Another study showed that knocking out the GABA a2 receptor from SACs resulted in reduced direction selectivity in OFF SACs, but not ON SACs (Chen et al., 2016), suggesting a difference between the computation in the ON and OFF channels. However, that study also showed that ON responses in DSGCs are impaired in noisy conditions, again suggesting that the importance of inhibition in the ON SAC computation depends on stimulus conditions.

One classic theory was that mutual inhibition between SACs was the origin of the direction selectivity in the circuit. SACs cofasiculate extensively and synapse onto one another. A modeling study showed that direction selectivity could originate from SAC-SAC inhibition (Münch & Werblin, 2006), and many studies that used pharmacology to block GABA receptors in the retina globally assumed that this perturbation primarily influenced SAC-SAC inhibition. However, a recent study in mouse that knocked out GABA release from SACs demonstrated that SAC release sites remained strongly direction-selective (Chen et al., 2016), suggesting that SAC-SAC inhibition plays no role in the computation. Thus, other inhibitory inputs may be contributing to this computation, which remains to be investigated.

Overall, these results suggest that SACs produce a direction-selective response independent of inhibition that is then augmented by inhibition. Thus, the mouse SAC dendrite appears to have features of a Hassenstein-Reichardt detector (preferential summing of excitatory inputs for outward motion) (Fig. 1.1D, left) but also relies on spatially offset, direction-selective inhibition from neighboring SACs to produce strong direction-selective signals.

Having described the connectivity between SACs and their presynaptic partners, we can now address how dendritic properties of SACs transform these inputs into the direction-selective GABAergic output. Beyond the role of the dendrites' passive membrane properties in supporting a direction-selective computation (Ding et al., 2016; Tukker et al., 2004; Vlasits et al., 2016), several mechanisms for producing nonlinearities in the dendrite have been investigated, including voltage-gated channels (Hausselt et al., 2007) and gradients of ion pumps (Dmitriev et al., 2012; Gavrikov et al., 2006). Most simulations agree that some nonlinearity, at the very least the voltage-gated calcium channel that triggers GABA release, will be necessary to produce the strong centrifugal selectivity observed experimentally (Hausselt et al., 2007; Tukker et al., 2004).

Excitatory Inputs to Direction-Selective Ganglion Cells

Although SACs' role in producing direction-selective inhibition has been well described, it remains difficult to determine whether DSGCs receive direction-selective excitation. Voltage clamp recordings from DSGCs during motion stimulation often produce tuned excitation (Borg-

Graham, 2001; Taylor & Vaney, 2002; Taylor et al., 2000), but this tuning may be due to voltage clamp errors produced by a strong and varying inhibitory shunt (Poleg-Polsky & Diamond, 2011). In addition, the relative contributions of cholinergic and glutamatergic input to DSGCs' computations has remained a puzzle. Recent work has begun to address these issues.

One classic hypothesis was that SACs would synapse onto bipolar cells, providing direction-selective inhibition to their axons and thereby decreasing glutamate release in the null-direction (Taylor & Vaney, 2002). This would lead to both asymmetric inhibition (more in the null-direction) and asymmetric excitation (more in the preferred-direction) onto DSGCs. However, EM reconstructions do not reveal such connections (Ding et al., 2016). In addition, several papers have failed to detect either direction-selective glutamate release using a glutamate sensor expressed on DSGCs or direction-selective calcium signals from bipolar cell terminals (Chen et al., 2014; Park et al., 2014; Yonehara et al., 2013). However, a recent study using a mouse lacking the vesicular GABA transporter in SACs suggests that DSGCs remain direction selective in the absence of direction-selective inhibition. Pei et al. (2015) demonstrated that, with GABAergic inputs from SACs diminished and symmetric, some DSGCs are still direction selective owing to direction-selective cholinergic signaling from SACs onto DSGCs. This suggests that excitation alone can provide direction information to DSGCs.

One puzzling aspect of ACh transmission is that SACs' specific wiring and centrifugal motion preference would lead to more ACh release in the null compared to the preferred-direction (Fig. 1.2A). Work in the rabbit retina showed that SACs release both ACh and GABA onto DSGCs but that kinetics and mechanisms of release differ (Lee et al., 2010), suggesting that ACh and GABA are released from separate synapses. A recent study in mouse provided further clues to answer this cholinergic puzzle. Sethuramanujam et al. (2016) demonstrated that cholinergic signaling is required for excitatory drive to DSGCs during visual stimulation with natural scenes, in which the motion edges were primarily low contrast. They further showed that stimulating SACs with Channelrhodopsin was sufficient to produce direction-selective firing in DSGCs without participation of bipolar cells. Using conductance analysis, they showed that in low-contrast conditions, roughly equal amounts of ACh are released during stimulation in either direction. Others have also observed that ACh transmission onto DSGCs is symmetric to motion (Park et al. 2014). This suggests either that SACs' cholinergic synapses with DSGCs are symmetric or that paracrine ACh release dominates cholinergic signaling. How these results relate to the finding that ACh can provide asymmetric excitation in the absence of inhibition from SACs (Pei et al., 2015) remains to be determined.

Recent findings in mouse have revealed that the simple circuit of bipolar cells, SACs, and DSGCs is not complete (Ding et al., 2016). Elucidating the precise identity of these additional synaptic partners, their roles in circuit function, and their modulation are exciting areas for future research.

Conclusions

Since the first identification of direction-selective neurons in rabbits, research in the past decades---afforded by technological advances such as two-photon microscopy, genetic manipulations, and dense EM reconstructions---has made tremendous progress in identifying the upstream circuit elements and their properties. Nonetheless, the conceptually modest problem of local motion detection has been remarkably resilient to an understanding at the biophysical level.

Theoretical models posit an asymmetry in the organization of inputs to local motion detectors, such that signals from different points in space are differently temporally filtered. In retinotopically organized neuropils, spatial integration is already given for neurons that receive inputs in multiple adjacent locations, as is the case for direction-selective SAC branches.

Asymmetric filtering could originate in different presynaptic neuron types, differentially connected to direction-selective cells depending on retinotopic location (Fig. 1.1D, left). In mammals, the evidence for space-time wiring of bipolar cells to different parts of SAC dendrites seems less likely based on updated EM reconstructions and recordings from SACs. Instead, a delay seems to be implemented in the SAC dendrite itself by electrotonic filtering (Fig. 1.1D, right). An asymmetry is given by distally located release sites, where centrifugally moving signals summate optimally. Direction selectivity is further enhanced by the precise wiring of excitatory inputs to the proximal portion of the dendritic tree, at least in mouse, as well as by reciprocal inhibition among neighboring SACs. As a third possibility, differential delays could also be implemented in direction-selective cells by asymmetrically distributed synapses with receptors of different dynamics, though as yet there is no direct evidence for this (Fig. 1.1D, middle).

Models of motion detection further require nonlinear integration in direction-selective cells, which can be of an enhancing or suppressing type. SACs appear to integrate nondirection-selective inputs in a purely enhancing fashion but also rely on suppression in some stimulus conditions. Although the physiological bases for these nonlinear interactions remain to be identified, a plausible implementation for a superlinear preferred-direction enhancement could be an amplification of coinciding signals through voltage-gated Ca^+ or Na^+ channels. Null-direction suppression could in turn be achieved by a shunting inhibition through opening of K^+ or Cl^- conductances.

In addition to the first local computation of motion direction performed by SACs, signals are further processed in their downstream circuits via additional circuit motifs. There is evidence for spatially offset excitatory enhancement and inhibitory suppression to DSGCs and additional evidence of nonlinearities in DSGC dendrites that enhance signals in the preferred-direction. These mechanisms support robust detection of motion direction that persists in varying stimulus conditions and behavioral settings.

Chapter II

Visual Stimulation Switches the Polarity of Excitatory Input to Starburst Amacrine Cells

This Chapter is a full reprint of Vlasits et al., *Neuron* (2014), in which I was the primary author. The work is included with permission from all authors.

Relevant publication:

Vlasits, A.L., Bos, R., Morrie, R.D., Fortuny, C., Flannery, J.G., Feller, M.B., and Rivlin-Etzion, M. (2014). Visual Stimulation Switches the Polarity of Excitatory Input to Starburst Amacrine Cells. *Neuron* 83, 1172–1184.

Abstract

Direction-selective ganglion cells (DSGCs) are tuned to motion in one direction. Starburst amacrine cells (SACs) are thought to mediate this direction selectivity through precise anatomical wiring to DSGCs. Nevertheless, we previously found that visual adaptation can reverse DSGCs' directional tuning, overcoming the circuit anatomy. Here we explore the role of SACs in the generation and adaptation of direction selectivity. First, using pharmaco-genetics and two-photon calcium imaging, we validate that SACs are necessary for direction selectivity. Next, we demonstrate that exposure to an adaptive stimulus dramatically alters SACs' synaptic inputs. Specifically, after visual adaptation, On-SACs lose their excitatory input during light onset but gain an excitatory input during light offset. Our data suggest that visual stimulation alters the interactions between rod and cone-mediated inputs that converge on the terminals of On cone BCs. These results demonstrate how the sensory environment can modify computations performed by anatomically-defined neuronal circuits.

Introduction

The retina is a highly organized set of circuits with well-defined cell types and patterns of connections (Masland, 2012). At the same time, the retina is known for its ability to adjust its sensitivity to ambient light levels (Enroth-Cugell and Shapley, 1973; Farrow et al., 2013; Grimes et al., 2014; Ke et al., 2014; Rieke and Rudd, 2009), stimulus contrast (Ke et al., 2014; Manookin and Demb, 2006; Nikolaev et al., 2013), and motion (Olveczky et al., 2007). These adjustments are accomplished through diverse circuit-level mechanisms, which change the roles and receptive fields of individual cells according to the visual environment. Recently, several examples of changes in receptive fields of cells involved in basic computations have been described, including the preferred direction of image motion (Münch et al., 2009; Rivlin-Etzion et al., 2012) and polarity (whether the cell responses to increases or decreases in light intensity) (Gao et al., 2013; Geffen et al., 2007). These adaptations are counter to the retina's well-defined anatomical wiring and suggest that circuit perturbations can dramatically change the computations performed by these neurons.

Previously we have shown that On-Off direction selective retinal ganglion cells (DSGCs) reverse their directional preference following visual stimulation with drifting gratings (Rivlin-Etzion et al., 2012). Here we study the effect of the same visual stimulation (referred to as "repetitive stimulation") on starburst amacrine cells (SACs), inhibitory interneurons that are responsible for mediating the direction selective receptive field of DSGCs (Fried et al., 2002; Lee et al., 2010; Wei et al., 2011). There are two populations of SACs. On-SACs, whose somas reside in the ganglion cell layer and whose processes stratify in the On sublamina of the inner plexiform layer, receive inputs from the On-cone bipolar cells (BCs). Off-SACs, whose somas are located in the inner-nuclear layer and whose processes stratify in the Off sublamina of the inner plexiform layer, receive inputs from Off-cone BCs. Surprisingly, we show that following visual stimulation, excitatory inputs to both classes of cells switch their polarity, resulting in On-SACs responding to decreases in light intensity and Off-SACs responding to increases in light intensity. This polarity switch does not rely upon inhibitory surround circuits in the inner retina; rather the switch originates presynaptic to BCs via surround circuits in the outer retina. Our results show that visual responses of multiple retinal cell types can vary dramatically within the confines of their strict anatomical wiring.

Methods

Animals

All animal procedures were approved by the UC Berkeley Institutional Animal Care and Use Committee and conformed to the NIH Guide for the Care and Use of Laboratory Animals, the Public Health Service Policy, and the SFN Policy on the Use of Animals in Neuroscience Research. Adult mice (P21-P40) of either sex were anesthetized with isoflurane and decapitated. Retinas were dissected from enucleated eyes under infrared illumination and orientation was determined based on stereotyped landmarks in the choroid as described previously (Wei et al., 2010). For calcium imaging of DSGCs, isolated retinas were mounted photoreceptor layer side down on a ring-supported hydrophilic PTFE membrane (Millipore) (Ivanova et al., 2013). For whole cell recordings, isolated retinas were mounted over a 1-2 mm2 hole in filter paper (Millipore) with the photoreceptor layer side down. Mounted retinas were stored in oxygenated Ames' media (US Biological) in the dark at room temperature prior to imaging or recording. Retinas from C57BL/6 mice were used for calcium imaging. To target SACs for whole cell recordings, we used two mouse lines that express fluorescent protein in starburst amacrine cells. On- and Off-SACs were targeted with mGluR2-GFP mice that contain a transgene insertion of interleukin-2 receptor fused to GFP under control of the mGluR2 promoter (Watanabe et al., 1998). On SACs were also targeted with ChAT-Cre/TdTomato mice generated by crossing a mouse in which IRES-Cre recombinase was knocked in downstream of the endogenous choline acetyltransferase gene (Ivanova et al., 2010) (Chat-cre) with a mouse line containing a loxP-flanked STOP cassette upstream of the tdTomato gene (B6.129S6-ChATtm1(cre)lowl/J × B6.129S6-Gt(ROSA)26Sortm9(CAG-tdTomato)Hze/J, Jackson Labs). Connexin-36 knockout mice in which the Cx36 coding sequence was replaced by a LacZ-IRES-PLAP reporter cassette were a generous gift from David Paul at Harvard Medical School (Deans et al., 2002).

Simultaneous Calcium Imaging and Visual Stimulation of DSGCs

The calcium dye Oregon Green 488 BAPTA-1 hexapotassium salt (OGB-1, Invitrogen) was electroporated using the ECM-830 Square Wave electroporation System (BTX Harvard apparatus) to uniformly label neurons within the ganglion cell layer of retinas mounted on ring-supported hydrophilic PTFE membranes. 8 µl of Ames's medium was placed on the lower caliper electrode, the mounted retina was placed over the lower electrode, and 5 µl of OGB-1 (5mM) was directly pipetted onto the tissue. Based on (Briggman and Euler, 2011), the following parameters were applied: ten 13-14 V (top electrode, on ganglion cell layer side), 10-ms-pulse-width, 1-Hz-pulse-frequency squarewave pulses. The distance between the two electrodes was fixed at 1.5 mm. The time to transfer the tissue to the recording chamber after electroporation was < 20 s. All of these procedures were performed under dim red illumination.

Two-photon fluorescence images were obtained with a modified movable objective microscope (MOM) (Sutter Instruments) using a 60x objective (Olympus LUMPlanFLN/IR360/1W). Two-photon excitation of the green calcium dye OGB-1 was evoked with an ultrafast pulsed laser (Chameleon Ultra II; Coherent) tuned to 800 nm. The microscope system was controlled by ScanImage software (www.scanimage.org). Scan parameters were [pixels/line * lines/frame (frame rate in Hz)]: [256 * 256 (1.5)], at 2 ms/line. This MOM was equipped with through-the-objective light stimulation and two detection channels for

fluorescence imaging. Visual stimuli were generated using MATLAB software and projected to the photoreceptor layer using a modified video projector (HP AX325AA Notebook Projector Companion; HP) displaying a UV light (single LED NC4U134A, peak wavelength 385 nm; Nichia). The intensity for the UV stimulus was 1.81 x 104 R*/cone/s. To decrease the noise entering the photon multiplier tubes due to the UV stimulation, we placed an emission filter (HQ535/50m-2P-18°AOI; Chroma Technology) in front of the green detection channel and a GG475 Schott glass filter (Chroma Technology) in front of the whole detector path. We used two kinds of stimuli: a series of flashed spots (231 μm diameter) and a bar (200 * 350 μm) moving in eight different directions across the field of view at 0.5 mm/s. Each direction was repeated three times. In both cases, the stimulus had a positive contrast (bright on darker background).

PSAM-PSEM neuronal silencing

The PSAML141F,Y115F:GlyR-IRES-GFP construct was subcloned from rAAV-syn::FLEX-rev::PSAML141F,Y115F:GlyR-IRES-GFP (Addgene #32481) into an AAV serotype 2 virus backbone (Dalkara et al., 2013). Vectors were packaged with the 7m8 capsid variant (Dalkara et al., 2013) according to methods in (Flannery and Visel, 2013). For viral injections, P6-8 ChAT-Cre mice (Ivanova et al., 2010) were anaesthetized with 3% isoflurane/2% O2. After applying lidocaine to the eyelid, the eyelid was opened with fine forceps, and an entry hole was made at the limbus with a sharp 30 gauge needle. 1-1.5μL of 1013 vg/mL 7m8-AAV2::FLEX-rev::PSAML141F,Y115F:GlyR-IRES-GFP was then intravitreally injected through this opening using a Borghuis Syringe (borghuisinstruments.com) and eyes were treated with opthalamic antibiotic drops before being returned to the cage. Light response of animals was assessed ≥3 weeks post-injection. To activate PSAM, 2mM PSEM89S (kind gift of Scott Sternson) stocks in dH2O were diluted 1:100 in Ames' media. Retinas were perfused with 20μM PSEM89S for at least 15 minutes prior to assessing PSAM activation (Fig. 2.4A). To measure the effect of PSEM89S on the input resistance of On-SACs, we performed voltage clamp recordings on PSAM-expressing cells by targeting GFP-positive cells using 2-photon microscopy as described below. Cells were stepped to at least two holding potentials to create an I-V curve of the holding current. Then, we calculated the input resistance from the slope of the linear fit to the I-V curve. All linear fits had R-squared > 0.94.

Retinal Histology

Whole mount retinas were fixed in 4% PFA for 3 hours at 4oC, then washed 5 times with PBT (.1% Triton-X 100 in PBS), and left in block solution (4% bovine serum albumin (Sigma) in PBT) for 4 hours at 4oC. Retinas were then incubated in primary antibody (1:250 Goat anti-ChAT, Millipore, AB144P and 1:1000 rabbit anti-GFP, Life Technologies, A11122) diluted in block solution for 4 days at 4oC. After washing retinas with PBT (3 times, 10 minutes) and block solution (2 times, 10 minutes), they were incubated in secondary antibody (1:1000 donkey anti-Rabbit Alexa Flour 488, Life Technologies; 1:1000 donkey anti-goat Alexa Fluor 568, Invitrogen) diluted in block solution overnight at 4oC. After washing 5 times with PBT and twice with PBS, retinas were mounted and coverslipped with Vectashield (Vector Laboratories).

Two-photon Targeted Electrophysiology

Retinas mounted on filter paper were placed under the microscope and perfused with oxygenated (95% O2 – 5% CO2), bicarbonate-buffered Ames' media at 32-34°C. To avoid bleaching the photoreceptors, fluorescently labeled retinal cells were targeted for whole cell recordings using two-photon microscopy at 920 nm to visualize fluorescence; and infrared illumination (>800 nm) to visualize cell morphology and guide the patch pipette (Wei et al., 2010). The inner limiting membrane above the targeted fluorescent cell was removed using a glass pipette before targeting a new pipette for recording. For whole cell voltage clamp recordings, borosilicate glass electrodes pulled to a 5-7MΩ tip were filled with an internal solution containing (in mM): 110 CsMeSO3, 2.8 NaCl, 4 EGTA, 5 TEA-Cl, 4 adenosine 5'-triphosphate (magnesium salt), 0.3 guanosine 5'-triphosphate (trisodium salt), 20 HEPES, and 10 phosphocreatine (disodium salt) with pH 7.2. For recordings from Off-SACs, 0.03 mM Alexa Fluor 594 hydrazide (Life Technologies, #A-10438) was included in internal solution for collecting 2-photon images of dendritic morphology after the visual stimulation protocol was complete. To target On-SACs in connexin-36 knock-out mice, we filled cells with small, round somas (Petit-Jacques et al. 2005) with Alexa Fluor 594 in the internal solution and imaged the dendritic morphology using a 2-photon microscope to determine cell identity before recording. A gigaohm seal was obtained before breaking in. Data were acquired at 10 KHz and filtered at 2 KHz with a Multiclamp 700A amplifier (Molecular Devices) using pCLAMP 10 recording software and a Digidata 1440 digitizer. The series resistance was measured during each sweep of the recordings using a -5 mV step and series resistance compensation was completed offline as described below in Data Analysis. For measuring synaptic currents, we recorded 5 sweeps at 4 different holding potentials (-72 mV, -32 mV, -12 mV and +8 mV) and averaged across the sweeps. For Fig. 2.4B-C, 2.6E-F and Fig. 2.9F-G, currents were recorded at only one holding potential (-72 mV). All holding potentials reported here are after correction for the junction potential (-12 mV). For pharmacology experiments, the following concentrations of neurotransmitter blockers were included in the Ames' media (in μM): 5 L-AP4, 5 gabazine, 100 MFA, 1 strychnine, or 50 TPMPA. The protocol for pharmacology experiments was the following: (1) perform repetitive stimulation, (2) record in adapted condition, (3) wash in pharmacological agent, then wait 10 min before recording drug condition. In some cases, we recorded from an adapted SAC in the control media and then recorded from a nearby SAC in the drug-containing media. For Fig. 2.5, 2.8 and 2.11, unstimulated responses to drug application were recorded 10 minutes after pharmacological agents were added.

Fluorescence Image Acquisition

For Fig. 2.1A, confocal images of immunostained whole mount retinas were taken with a Zeiss inverted AxioOberver Z1 with a LSM 710 confocal scanhead using a 20x/0.8 Plan-Apochromat air objective and 488nm and 561nm laser lines. Z-stacks were acquired with a 0.86μm step size using ZEN software.

To image the dendritic morphology of Off-SACs (Fig. 2.3) and verify On-SAC identity in Cx36 KO mice (Fig. 2.10 and Fig. 2.11), fluorescence images of Alexa-594 dye-filled SACs were collected using a custom-modified two-photon microscope ((Wei et al., 2010); Fluoview 300, Olympus America Inc.) at 810 nm. Images were collected over the depth of the ganglion cell layer, inner plexiform layer, and inner nuclear layer at 1 μm increments. For the image of Off-SAC in Fig. 2.3A brightness and contrast were adjusted to more easily visualize the dendritic morphology.

Visual Stimulation of SACs

Visual stimuli were transmitted through a 60x objective (Olympus LUMPlanFL N/60x /1.00W) using an OLED display mirroring a monitor displaying custom stimuli created using MATLAB software with the Psychophysics Toolbox as described previously (Huberman et al., 2009). The emission spectrum of the OLED was cut below 470 nm and therefore did not stimulate the UV-sensitive ventral cones (Wang et al., 2011). Display images were centered on the soma of the recorded cell and were focused on the photoreceptor layer. All experiments were carried out in the photopic light range: background light intensity of the OLED was 1.15 x 104 R*/rod/s, which we defined as the "light off" or "light offset" period. Light spot stimuli consisted of a 225 μm diameter white spot with intensity 2.2 x 105 R*/rod/s presented for 2 s unless otherwise stated.

For measuring synaptic currents, the light spot was presented 5x at 6 or 8 s intervals at the 4 different holding potentials listed above. For the repetitive stimulus, we used a protocol that efficiently reversed directional preference of On-Off direction selective ganglion cells (Rivlin-Etzion et al., 2012). The stimulus consisted of symmetric drifting gratings with 225 μm/cycle, 4 cycle/s, corresponding to 30 deg/s. The light intensity of the gratings was at 100% contrast for the OLED display; the mean intensity (grey) was 1.15 x 105 R*/rod/s. First, gratings drifting in 8 different directions were presented for 3 s either 4x or 8x in a row; next gratings drifting in the nasal direction were presented for 40 s followed by 40 s drifting in the temporal direction; finally we repeated the stimulation of gratings in 8 directions. For Fig. 2.6E-F, bouts of gratings were alternated with light spot stimuli at -72 mV to measure the excitatory current during the repetitive stimulation. For Fig. 2.9F-G, the duration of the light flash was varied and the light was flashed 5x times in a row for each duration. To verify that changes in conductance of adapted SACs do not emerge as a result of prolonged whole-cell recordings, we stimulated a subset of cells in each experiment before attaching onto them (Table 2.1).

Table 2.1 **Sample sizes for experiments in Chapter II**
Characterization of SAC polarity.

Figure	Experiment	Control	Adapted	Both
2.1D	Dorsal On SACs	12	13	9
2.1D	Off SAC	9	9	9
2.3B	Ventral On SACs	11	12	6
2.4H	PSAM	4	6	2
2.6F	Cx36 KO	11	11	7

Pharmacological manipulations

Figure	Experiment	Adapted	Drug	Both
2.6B	L-AP4	6	6	4
2.6C	Gabazine	6	6	4
2.6C	Strychnine	6	6	6
2.6C	TPMPA	2	4	2
2.6E	L-AP4	5	5	5
2.6F	MFA		10	

Data analysis

Data analysis was performed in MATLAB (MathWorks), ImageJ, and IgorPro (WaveMetrics). Conductance analysis to determine excitatory and inhibitory synaptic inputs was performed in MATLAB using the algorithm described in Taylor & Vaney (Taylor and Vaney, 2002). Briefly, sweeps at each holding potential were downsampled by calculating the average current in 10 ms bins and then downsampled sweeps were averaged. The baseline holding current (I_h) was defined as the average current during the 2 s before the light flash and was subtracted from each average trace. We compensated for the series resistance (R_s) by measuring the series and input resistance (R_{in}) from a -5 mV pulse at the end of each trace. Because SACs have a large amount of spontaneous activity at rest (Fig. 2.9B-E), we selected the values to use for series resistance compensation from the holding potential with the least amount of spontaneous activity as determined by visual inspection offline for each cell. We used the following equations for compensation of the recorded current (I_m) and the holding potential (V_h):

(1) $$I_{m,compensated} = I_m * \frac{R_{in}+R_s}{R_{in}}$$

(2) $$V_{h,compensated} = V_h - I_h * R_s$$

Then we fit a line to the IV data ($I_{m,compensated}$ vs. $V_{h,compensated}$) for the four holding potentials at each time point in the trace. The slopes and intercepts of these lines were used to calculate the total conductance g_T (the slope) and the reversal potential V_{rev} (-intercept/slope). We assumed that the excitatory reversal potential V_e = 0 mV and calculated the inhibitory reversal potential Vi = -73 mV based on the ionic compositions of our external and internal solutions. Then, the following equations were used to calculate the excitatory (g_e) and inhibitory (g_i) conductances as a function of time (t):

(3) $$g_i(t) = \frac{g_T(t)*(V_{rev}(t)-V_e)}{V_i-V_e}$$

(4) $$g_e(t) = g_T(t) - g_i(t)$$

For Figs. 2.3, 2.6C-D, 2.5, 2.8, 2.11, we quantified the resulting conductance traces with respect to the light spot stimulus during two time periods by integrating over an 800 ms time window from 50-850 ms after light onset and from 100-900 ms after light offset. Tonic responses in Fig. 2.7 were measured by integrating over the time period from 1050 to 1850 ms after light onset. For Fig. 2.4C-D, 2.6F, 2.9A and G, 2.10C and 2.14, we quantified the charge transfer by integrating over the excitatory current recorded at -72 mV in the same time windows. We chose these specific time windows based on the population response onset and duration.

Analysis of the experiments in Fig. 2.4B-C, 2.6E-F and Fig. 2.9B-G were performed in IgorPro (Wavemetrics, Inc) using NeuroMatic functions. Five sweeps at each condition were averaged. For Fig. 2.9F-G, charge transfer was calculated by integrating over the 400 ms following the time of the maximum current. For Fig. 2.9C and E, the variance was calculated from 5 raw current sweeps (unaveraged) over two 1800 ms time windows when the light is off (100-1900 ms from beginning of the recording) and when the light was on (100-1900 ms after light onset). Then we calculated the average variance of the 5 current sweeps for five different cells.

For calcium imaging, images were analyzed offline using custom MATLAB software. The regions of interest (ROIs) of cells were determined using the Trainable Weka Segmentation (Waikato Environment for Knowledge Analysis) (Fiji) on all cells in a field-of-view, and the pixel intensities within an ROI were averaged at each time step. The fluorescence intensity of a neuron is reported throughout as the average intensity of all pixels over its soma, including the nucleus. The mean intensity value for each cell was filtered with a rolling ball filter to eliminate any wandering baseline. Fluorescence responses are reported as normalized increases as follows:

$$\frac{\Delta F}{F} = \frac{F - F_{\circ}}{F_{\circ}}$$

where F is instantaneous fluorescence induced by UV light stimulation and Fo is the baseline fluorescence when visual stimulation is absent.

The directionally selective index (DSI) was calculated for the two-photon OGB-1 signals as:

$$DSI = \frac{\frac{\Delta F}{F}_{pref} - \frac{\Delta F}{F}_{null}}{\frac{\Delta F}{F}_{pref} + \frac{\Delta F}{F}_{null}}$$

Where $[\Delta F/F]_{pref}$ and $[\Delta F/F]_{null}$ are the mean amplitudes of [ΔF/F] evoked by the bars moving in the preferred and null directions, respectively. The preferred direction of the cells was indicated by the direction of the vector sum of [ΔF/F] to all directions. The null direction was 180 degree rotated from preferred. The trial-averaged values are given as the mean ± SD. Cells were considered direction selective if DSI>0.4.

Statistics

Unless otherwise stated in the Results, to compare between control and test populations, we ran a Wilcoxon rank-sum test in MATLAB. Significance levels of the difference between median values of the two populations are reported by the p value.

Simulation of Changes in DSGCs' Directional Tuning Following Polarity Switch in SACs

Excitatory and inhibitory conductances onto DSGCs in response to PD and ND grating stimulation were simulated as rectified sinusoids. For simplification, the simulation included responses mediated only by the On pathway. The relative timing between excitation and inhibition was changed to estimate the effect of a phase shift in the inhibitory conductance onto DSGCs on their directional preference. Excitatory conductance did not depend on the direction of stimulation, while inhibitory conductance in response to ND stimulation preceded inhibitory conductance in response to PD stimulation by half a cycle (π). This time difference between inhibitory conductance towards PD and ND stimulation remained constant throughout the simulation, and the inhibitory conductances in response to both directions were shifted together in the simulation.

Control state (un-adapted), was defined as 0 phase shift. Here, inhibition co-occurred with excitation and canceled out the excitation in response to ND stimulation but not in response

to PD stimulation. Inhibitory conductances were shifted from 0 phase to 2π phase, to cover all possible time shifts between excitatory and inhibitory conductances.
For each given phase shift, we determined the membrane potential of a DSGC in response to drifting gratings in each time point based on the excitatory and inhibitory conductances as follows:

(5) $V_m(0) = -60$
(6) $I(t+1) = g_{exc}(V_m(t) - 0) + g_{inh}(V_m(t) + 80)$
(7) $V_m(t) = V_m(t-1) - I(t) * R$

where V_m (t) is the membrane potential at time t; I(t) represents the total synaptic current to the cell at time t based on the excitatory and inhibitory conductances, g_{exc} and g_{inh}, and their reversal potentials, 0mV and -80mV, respectively; R is the input resistance of the DSGC, (estimated at 100 MOhm).

Spiking activity in the DSGC in response to PD and ND stimulation were randomly generated based on membrane potential values at each time point. Action potentials had a probability of 0 for membrane potentials lower than or equal to -40mV, and a probability of (Vm(t)+60)/100 for higher membrane potential values (e.g., $P_{spike}(t \mid V_m(t)=-20)=0.4$). For every phase shift, we generated 100 spike trains in response to PD and ND stimulation and calculated the direction selective index (DSI) for each pair based on:

(8) $DSI = < \frac{PD_i - ND_i}{PD_i + ND_i} >$

where PD_i and ND_i represent total number of spikes in the *i*th random spike trains in response to PD and ND stimulations, and <.> denotes averaging.

Results

Reversible Inactivation of SACs Abolishes Direction Selectivity

Previous work demonstrating that SACs are necessary for the computation of direction selectivity used an immunotoxin to kill SACs over the course of days (Amthor et al., 2002; Yoshida et al., 2001), an irreversible perturbation of the circuit. To test unambiguously whether SAC activity is required for generating direction selective responses, we reversibly inhibited SACs using pharmaco-genetics by expressing a chimeric ligand-gated chloride channel, PSAML141F,Y115F-GlyR (PSAM, (Magnus et al., 2011)) in SACs (Fig. 2.1A). This was achieved by intravitrial injection into Chat-cre mice of a 7m8-AAV2 virus (Dalkara et al., 2012; 2013) carrying a flex-PSAM-IRES-GFP gene. Application of the synthetic ligand PSEM89S to the retina reversibly opened the PSAM chloride channels, which significantly reduced the mean input resistance of On-SACs (297±84.6 MΩ before addition of PSEM89S to 164±66.4 MΩ in PSEM89S, n=6 cells, $p<0.05$).

To assess the effect of activating PSAM on direction selectivity, retinas expressing PSAM were loaded with the calcium dye Oregon Green-BAPTA via electroporation and responses to drifting bars were characterized using two-photon calcium imaging (Briggman and Euler, 2011; Briggman et al., 2011; Yonehara et al., 2013). Both On-Off DSGCs and On-DSGCs were detected (Fig. 2.1B, C). After application of PSEM89S, the vast majority of DSGCs lost

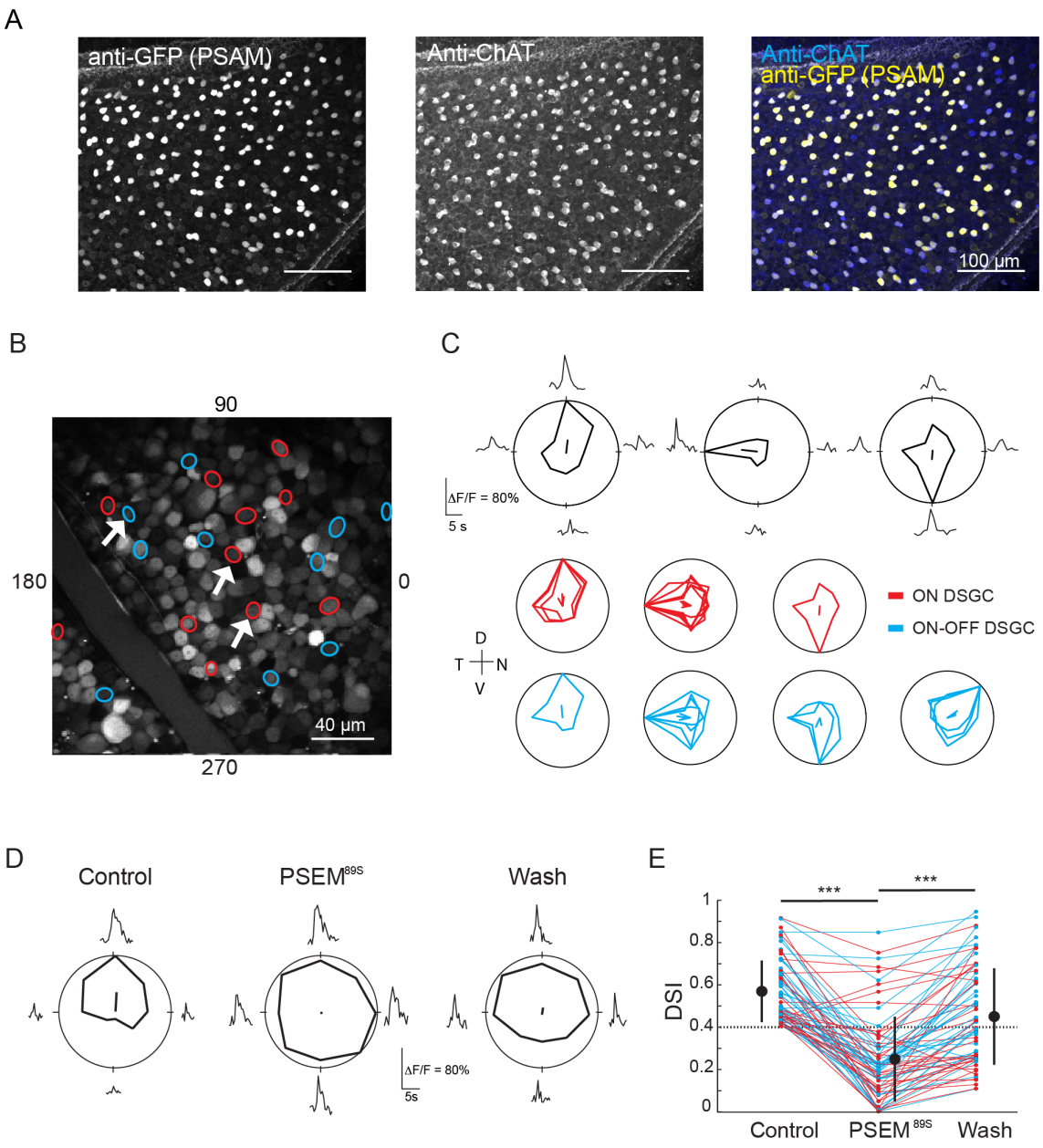

Figure 2.1 **Reversible inactivation of SACs abolishes direction selectivity.** (A) Fluorescence projections of confocal images of the ganglion cell layer of a ChAT-Cre mouse retina injected with AAV2-PSAM^{L141F,Y115F}-GlyR-IRES-GFP. Immunostain is for GFP (co-expresses with PSAM, left) and choline acetyltransferase (ChAT), a marker for SACs (middle). GFP-positive cells are also ChAT immunoreactive (right). (B) Two-photon fluorescence image of the ganglion cell layer of a retina expressing PSAM that has been electroporated with cell impermeant Oregon Green 488 BAPTA-1. Circles are cells identified as DSGCs, color-coded by response type (red: On DSGCs, blue: On-Off DSGCs). White arrows correspond to the individual tuning curves in (C). (C) Top: examples of average calcium responses ($\Delta F/F_0$) and tuning curves of three DSGCs (white arrows in (B)) in response to a white bar moving in eight different directions. The solid lines inside the polar plots indicate the vector-summed response corresponding to the preferred direction. Bottom: tuning curves for all of the DSGCs imaged in (B). Each tuning curve is normalized to the maximum response for each cell. Color codes as in (B). Axes of the retina are indicated to the left of the plots; D = dorsal, N = nasal, T = temporal, V = ventral. (D) Example tuning curve of a DSGC before (Control), during (PSEM^{89S}) and after (Wash) the addition of PSEM^{89S}. (E) Effect of PSEM^{89S} on the direction selective index (DSI) of DSGCs (n = 68 cells) in 5 retinas. Large circles are group means, error bars are SD, dotted line indicates the threshold DSI for defining a cell as a DSGC (DSI > 0.4). Color codes as in (B).

their directional tuning, responding equally to motion in all directions (DSI for Control: 0.57 ± 0.15; for PSEM: 0.25 ± 0.20; for Wash: 0.45 ± 0.22; n = 68 cells from 5 retinas; one-way ANOVA, $p<0.001$; Tukey post-hoc for Control vs. PSEM, $p<0.001$; for PSEM vs. Wash, $p<0.001$; Fig. 2.1D, E), consistent with a loss of direction-selective inhibition from SACs. Addition of PSEM89S to wild-type retinas, which did not express PSAM, resulted in no change in the DSI of DSGCs (Fig. 2.2, DSI for Control: 0.57 ± 0.14; for PSEM: 0.56 ± 0.15, n=46 cells from 4 retinas; paired t-test $p=0.7$), indicating that there were no off-target effects of PSEM89S. These data demonstrate the requisite role of SACs in the direction-selective computation and demonstrate that the reduction in SAC excitability using PSAM is sufficient to prevent their participation in the direction-selective circuit.

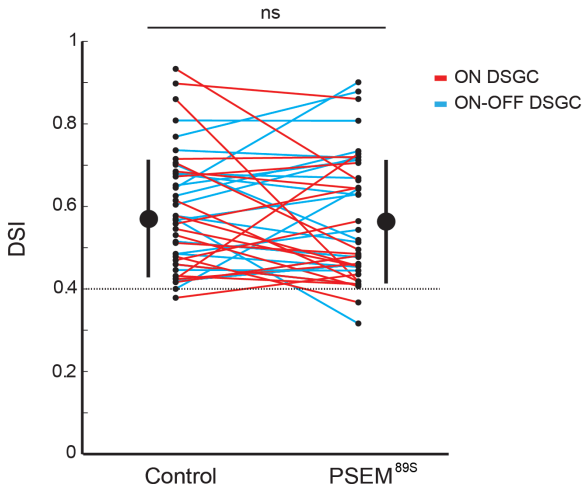

Figure 2.2 **PSEM^{89S} has no effect on direction selective tuning of DSGCs in wild type mice.** Effect of PSEM^{89S} on the direction selectivity index (DSI) of On (red) and On-Off (blue) DSGCs (n = 46 cells, small black circles) in 4 retinas from wild type mice, which were not infected with PSAM virus. DSI was determined using 2-photon calcium imaging as described in Figure 2.1. Large circles are group means, error bars are SD, dotted line indicates the threshold DSI for defining a cell as a DSGC (DSI > 0.4).

Starburst Amacrine Cells Switch Their Polarity as A Result of Visual Stimulation

Previously, we found that visual adaptation using repetitive stimulation induced a reversal of the directional tuning of DSGCs. In addition, repetitive stimulation induced changes in the synaptic inputs to DSGCs, most notably the inhibitory inputs (Rivlin-Etzion et al., 2012), suggesting that the repetitive stimulation might alter the light responses of SACs. We performed two-photon targeted whole-cell voltage clamp recordings from transgenically-labeled SACs ((Rivlin-Etzion et al., 2012; Wei et al., 2010); Fig. 2.3A) to characterize the effect of repetitive stimulation on the response to increases and decreases in illumination using a 2-s stationary white spot projected onto the retina. Initially, our recordings from On-SACs were restricted to the dorsal half of the retina where our visual stimulus would robustly activate the cones sensitive to green light (Breuninger et al., 2011; Wang et al., 2011). Currents were measured at four different holding potentials (Fig. 2.3B, blue), allowing us to perform conductance analysis to isolate the excitatory inputs from the inhibitory inputs (Fig. 2.3C, blue; (Taylor and Vaney, 2002); see Extended Experimental Procedures). We then exposed the retina to the repetitive stimulation previously

shown to reverse the direction preference of DSGCs (Rivlin-Etzion et al., 2012) and repeated the light spot stimulation and conductance analysis (Fig. 2.3B, C; black).

Before repetitive stimulation, On-SACs exhibited a large excitatory conductance at light onset, but not at light offset (Fig. 2.3B, C; blue). Following repetitive stimulation, many On-SACs lost their excitatory input at light onset and, surprisingly, gained an excitatory input at light offset, thereby switching their polarity (Fig. 2.3B, C; black). In contrast, the inhibitory conductance onto On-SACs was observed at light onset as well as at light offset both before and after repetitive stimulation, indicating that the basic organization of inhibition did not change. We refer to the state following repetitive stimulation as "adapted".

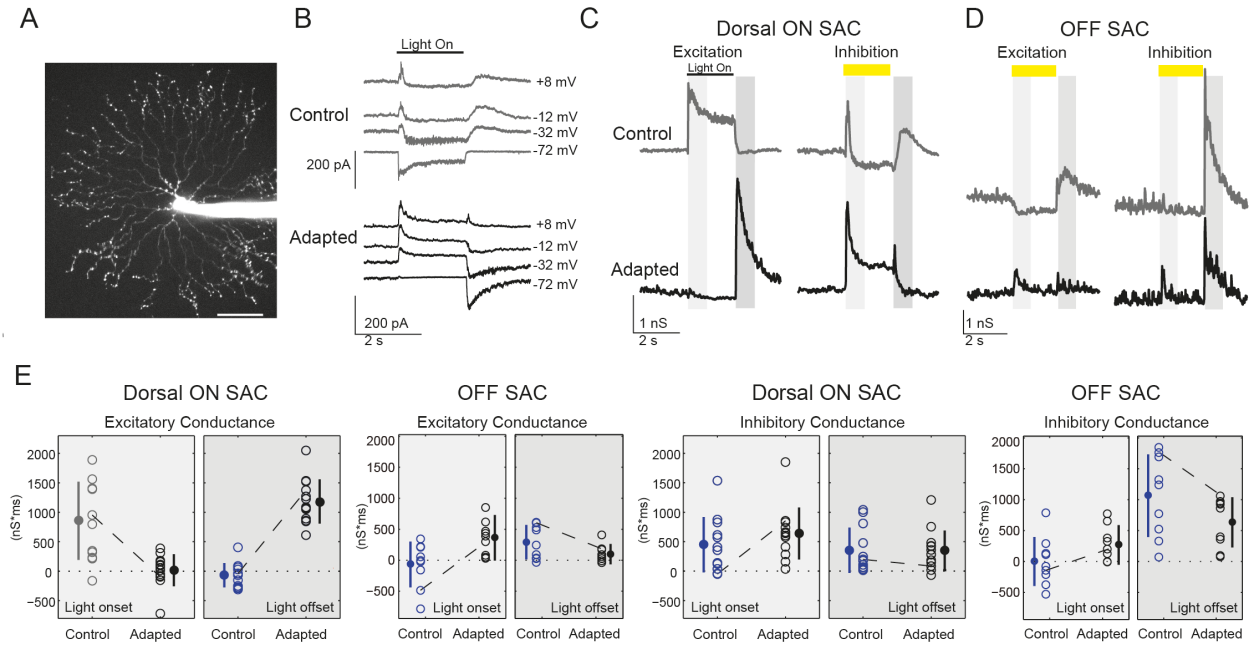

Figure 2.3 **SACs switch their polarity as a result of visual stimulation**. (A) Projection of fluorescence image of an Off-SAC filled with Alexa Fluor 594, scale: 50 µm. (B) Synaptic currents onto a dorsal On-SAC at different holding potentials in response to a 2-s light spot (225 µm diameter) before (top) and after (bottom) adaptation. Traces are averages of five sweeps. (C, D) Excitatory and inhibitory conductances from a dorsal On-SAC (C) and an Off-SAC (D) were evaluated at 10 ms intervals based on the I-V relations in response to a 2-s white spot stimulus. The On-SAC conductances correspond to the current measurements shown in (B). The time periods for calculating the integrated conductances (see (E) below) are indicated by the yellow rectangle for light onset (50-850 ms after light onset) and by the grey rectangle for light offset (100-900 ms after light offset). (E) The integrated excitatory and inhibitory conductances during light onset and light offset for dorsal On-SACs and all Off-SACs before and after adaptation. Empty circles are conductances in individual cells. Dashed lines represent the example cells shown in (C) and (D). Mean values are represented by the filled circles, error bars = standard deviation. Blue data = controls (before adaptation), black data = adapted cells. Light stimulation is indicated by the yellow bar.

To compare control and adapted populations, we quantified the overall conductances of each SAC at light onset and light offset (Fig. 2.3E). The population analysis demonstrates that adapted On-SACs in the dorsal half of the retina had a reduced excitatory conductance at light onset (863±664 nS*ms in controls, n=12; 16±272 nS*ms in adapted cells, n=13; $p<0.01$; Fig. 2.3E) and gained an excitatory conductance at light offset (-70±206 nS*ms in controls; 1184±377 nS*ms in adapted cells; $p<0.01$). Inhibitory conductance onto adapted On-SACs did

not significantly change (p=0.17 and p=0.68 for light onset and light offset, respectively). To verify that changes in conductance of adapted On-SACs did not emerge as a result of prolonged whole-cell recordings, we presented the adapted stimulus to a subset of cells before recording from them (n=4/13 On-SACs; see Table 2.1 for details on sample sizes for this and subsequent experiments).

We executed the same protocol on Off-SACs, which also exhibited a polarity switch, increasing their excitatory conductance in response to light onset (-70±361 nS*ms in controls; 358±276 nS*ms in adapted cells; $p<0.05$; Fig. 2.3D, E; Note: Off-SACs were recorded from both dorsal and ventral regions of the retina). The excitatory conductance of adapted Off-SACs in response to light offset was not changed significantly (p=0.14). Following repetitive stimulation, inhibition onto Off-SACs was also not changed significantly (p=0.09 and p=0.22 for light onset and light offset, respectively).

Polarity Switch Occurs Independent of SAC Activity and Inhibitory Circuits

The above experiments demonstrate that the excitatory inputs to SACs are dramatically altered following repetitive stimulation, indicating that the site of modulation is the BC terminal presynaptic to SACs. GABA-A and GABA-C receptors are localized to the terminals of On-cone BCs and therefore can provide a powerful inhibition of glutamate release (Sagdullaev et al., 2006). It has been postulated that the asymmetric release of glutamate associated with direction selectivity in DSGCs is due to feedback inhibition from SACs onto the terminals of On-cone BCs (Vaney et al., 2012; Wei and Feller, 2011) (but see recent findings indicating glutamate release is not modulated by motion stimulation (Park et al., 2014; Yonehara et al., 2013)).

To test whether the polarity switch is due to a change in SACs' feedback inhibition onto BCs, we reversibly inhibited SACs during repetitive stimulation in mice expressing PSAM in SACs by adding PSEM89S only during the repetitive stimulation (Fig. 2.4A). We found that dorsal On-SACs still switched their polarity when the SAC activity is reduced by PSEM89S during the repetitive stimulus (Fig. 2.4B, C); On-SACs lose their excitatory current at light onset (control, 32.6±19.5 pA*sec; stimulated, -9.0±10.8 pA*sec) and gain an excitatory current at light offset following repetitive stimulation (control, -5.7±4.9 pA*sec; stimulated, 50.8±7.1 pA*sec).

While it is known that GABA-A receptors mediate inhibition between On-SACs, blocking GABA-A signaling before repetitive stimulation did not abolish inhibitory input to On-SACs, suggesting that the combination of inhibitory inputs to these cells is complex (Fig. 2.5). We tested whether acute blockade of inhibition from SACs and other sources could affect the excitatory Off response gained after repetitive stimulation. Addition of either GABA-A or GABA-C receptor blockers (5 μM gabazine and 50 μM TPMPA, respectively) to the solution following repetitive stimulation did not abolish the adapted Off response (Fig. 2.4D; Fig. 2.5), confirming that inhibitory feedback from SACs or any other GABAergic amacrine cell did not mediate the adapted Off response. Another source of modulation of release from BCs terminals is crossover inhibition, which is mediated by both glycinergic and GABAergic amacrine cells (Werblin, 2010). We found that the addition of the glycine receptor antagonist, strychnine (1 μM), after repetitive stimulation did not eliminate the Off response charge transfer or conductance in On-SACs (Fig. 2.4D; Fig. 2.5).

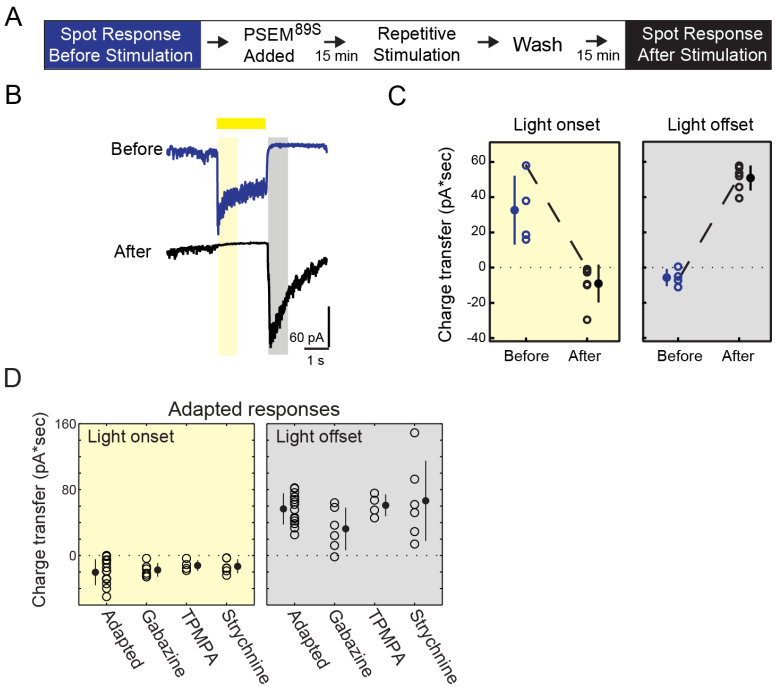

Figure 2.4 **Polarity switch occurs independent of SAC activity and inhibitory circuits.** (A) Protocol for assessing SAC adaptation in the presence of PSEM^{89S}. PSEM^{89S} was present during the repetitive stimulation but not while measuring the response to light spot stimuli before and after stimulation. (B) Example of voltage clamp recording (average of 5 sweeps) from PSAM-expressing On-SAC held at -72 mV during light spot stimuli presented before and after the protocol outlined in (A). The time periods for calculating the charge transfer are indicated by the yellow rectangle for light onset (50-850 ms after light onset) and by the grey rectangle for light offset (100-900 ms after light offset). (C) Charge transfer (averaged over five sweeps) of the excitatory current during light onset and light offset as specified by the yellow and grey boxes in (B) for On-SACs before and after stimulation in the presence of PSEM^{89S}. The dotted line is the cell in (B). (D) The excitatory charge transfer during light onset (yellow) and light offset (grey) in individual adapted On-SACs in control solution (Adapted) and after application of 5 µM gabazine, 50 µM TPMPA, or 1 µM strychnine. For (C, D) Empty circles = individual cells, solid circles = mean, error bars = SD.

Together, these data rule out a role for inner retina inhibitory circuits in the polarity switch in On-SACs, suggesting that the polarity switch is not due to feedback or crossover inhibition.

Gain of Off Response Requires Cone Activation

How is repetitive stimulation altering the release of glutamate from BCs? Light responses in the mouse retina are mediated by interactions of cone and rod pathways (Grimes et al., 2014; Ke et al., 2014; Münch et al., 2009; Wang et al., 2011) (Fig. 2.6A). Hence, the loss of the On response and the appearance of the Off response in On-SACs may result from a change in the interaction between these pathways. To isolate the contributions of rod and cone pathways, we took advantage of the ventral-to-dorsal gradient of cone opsin expression, as cones in the ventral retina are dominated by UV opsins, while those in the dorsal retina are dominated by green opsins (Applebury et al., 2000; Calderone and Jacobs, 1995) (Fig. 2.6B). These experiments were conducted using visual stimuli that did not strongly activate UV opsins. Thus, to minimize

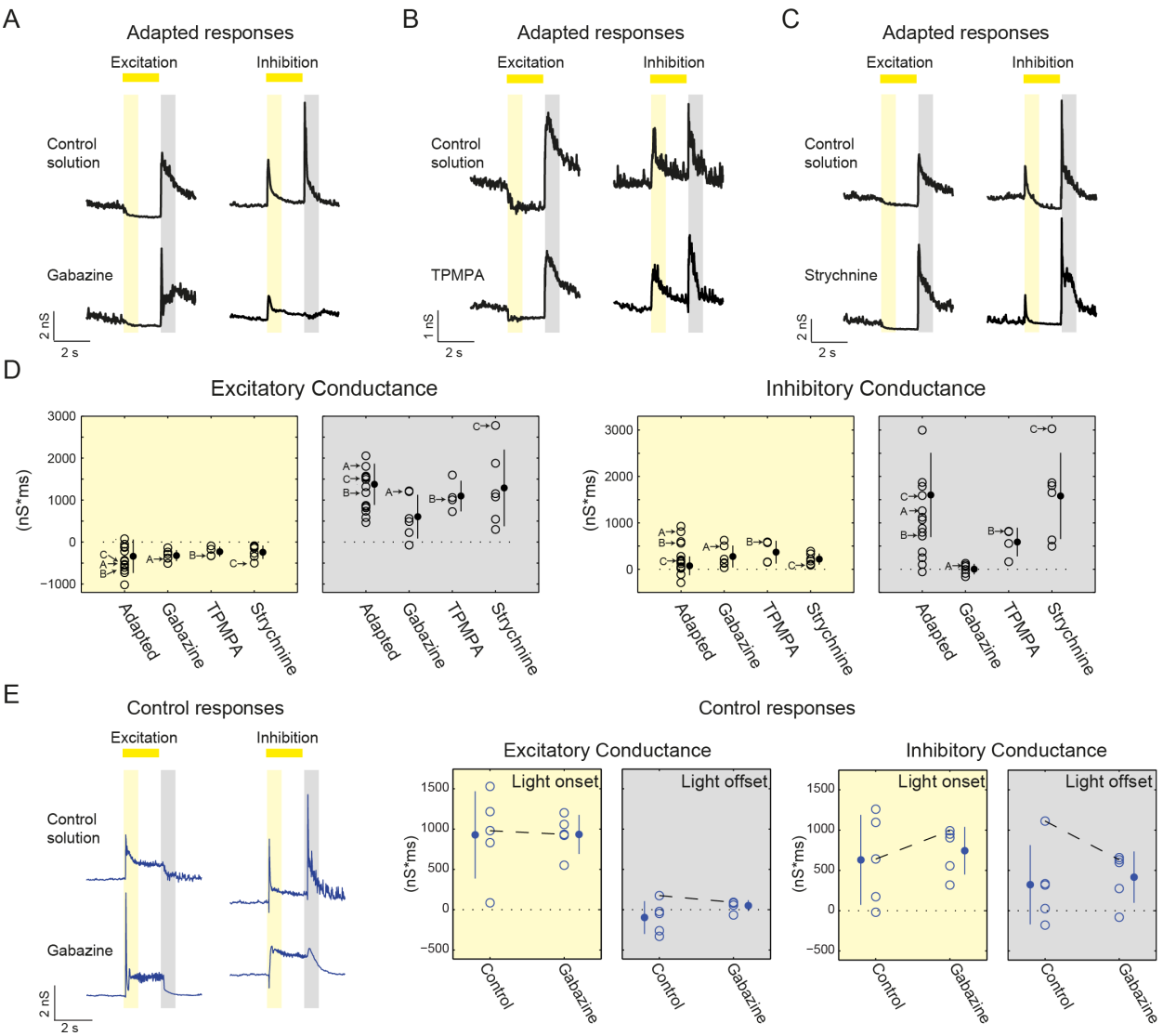

Figure 2.5 **Conductance analysis of control and adapted responses in the presence of inhibitory blockers**. (A-C) The excitatory and inhibitory conductance at light onset and light offset for adapted On-SACs in control solution and in 5 µM Gabazine (A), 50 µM TPMPA (B) or 1 µM Strychnine (C). Conventions are as in Fig. 2.3C. (D) The excitatory (left) and inhibitory (right) integrated conductance at light onset and light offset for adapted On-SACs in control solution and after application of 5 µM gabazine, 1 µM strychnine, or 50 µM TPMPA. Conventions are as in Fig. 2.3E. Arrows indicate conductances of example cells in A-C. (E) Left: the excitatory and inhibitory conductance at light onset and light offset for unadapted On-SACs in control solution and in 5 µM Gabazine. Conventions are as in Fig. 2.3C. Right: The excitatory (left) and inhibitory (right) integrated conductance at light onset and light offset for unadapted On-SACs in control solution and after application of 5 µM Gabazine. Conventions are as in Fig. 2.3E.

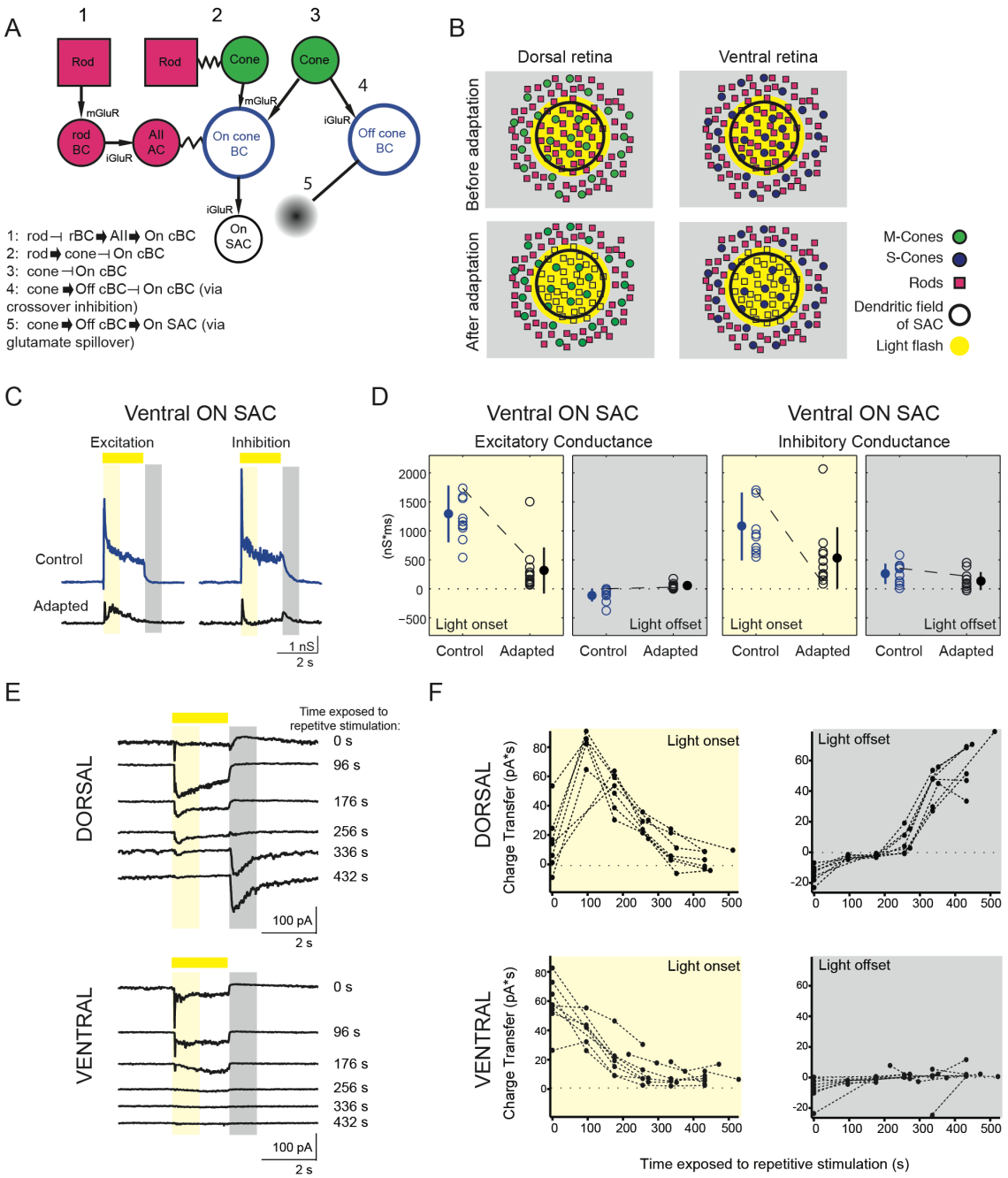

Figure 2.6 **Gain of off response requires cone activation**. (A) Schematic of potential pathways that could influence signaling in On-SACs. (B) Schematic of experimental results. Light stimulation with an OLED activated both rods and cones in the dorsal retina and only rods in ventral retina. Following repetitive stimulation, rods are no longer responsive to light spots. (C) Excitatory and inhibitory conductances from a ventral On-SAC. Conventions are as in Figure 2.3C. (D) The integrated excitatory and inhibitory conductances during light onset and light offset for ventral On-SACs before and after adaptation. Conventions are as in Figure 2.3E. (E) Voltage clamp recordings of excitatory currents from dorsal (top) and ventral (bottom) On-SACs (holding potential = -72 mV) in response to a 2-s light spot (225 µm diameter). Spots were presented in between exposing the cells to repetitive stimulation, with the time exposed to repetitive stimulation indicated on the right. Traces are averages of five sweeps. The time periods for calculating the charge transfer are indicated by the yellow rectangle for light onset (50-850 ms after light onset) and by the grey rectangle for light offset (100-900 ms after light offset). (F) Charge transfer (averaged over five sweeps) of the excitatory current during light onset and light offset for dorsal (top) and ventral (bottom) On-SACs as a function of the amount of time cells were exposed to gratings.

the cone contribution, we monitored the effects of repetitive stimulation on ventral On-SACs. We found that after repetitive stimulation, On-SACs in the ventral half of the retina lost their excitatory input at light onset in a manner similar to On-SACs in dorsal retina (from 1294±487 nS*ms in controls to 317±395 nS*ms in stimulated cells; $p<0.01$; quantification of the sustained component of the light response is provided in Fig. 2.7). Conversely, ventral On-SACs did not gain a large Off response following repetitive stimulation, though there was a slight increase in the integrated-conductance (-107±107 in controls; 55±48 nS*ms in adapted cells; $p<0.01$; Fig. 2.6C, D). These data indicate that the On response lost following repetitive stimulation is due primarily to a loss of rod mediated signaling while the Off response gained after repetitive stimulation occurred uniquely in the dorsal half of the retina, suggesting that strong activation of cones is required for the polarity switch.

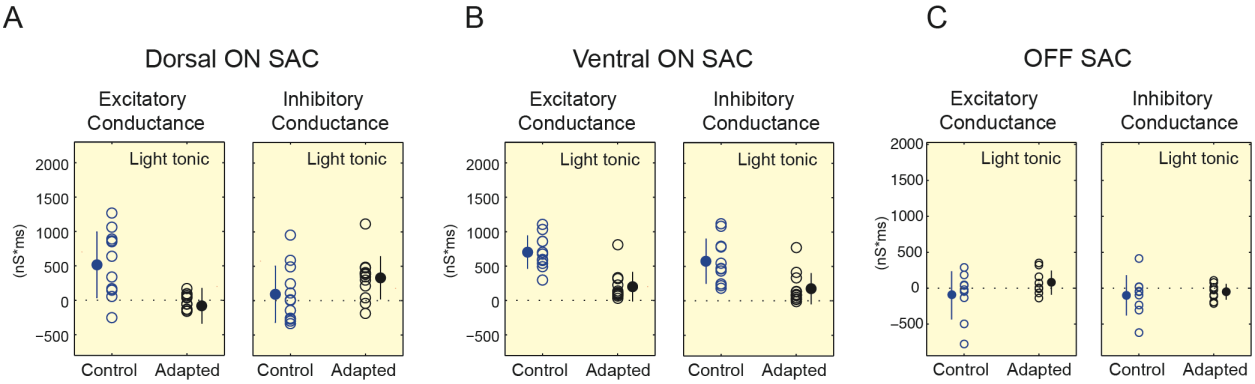

Figure 2.7 **Tonic excitatory conductances are reduced in On and Off-SACs after adaptation**.
The light response had two components – a fast transient component followed by a slower tonic component. We independently quantified the changes in the tonic response following repetitive stimulation by integrating over the period between 1050–1850 ms after light onset for both On- and Off-SACs. The results mirrored the results at light onset, with both dorsal and ventral On-SACs losing the tonic On response after repetitive stimulation.
Excitatory and inhibitory conductances from dorsal On-SACs (A), ventral On-SACs (B) and Off-SACs (C). The time periods for calculating the tonic integrated conductance was 1050 – 1850 ms after light onset. Blue data = controls (before adaptation), black data = adapted cells. Empty circles are conductances in individual cells. Mean values are represented by the filled circles, error bars = standard deviation.

One simple explanation for the switch in polarity of the excitatory inputs to On-SACs is that the strong repetitive stimulation has saturated the rod photoreceptors such that they no longer respond to light spots. Indeed, the light levels used during repetitive stimulation can lead to saturation of rods (Wang et al., 2011), which cannot recover since our preparation does not have a pigment epithelium. In this scenario, the Off response gained after repetitive stimulation is mediated by cones; the difference between the effect of repetitive stimulation on dorsal and ventral On-SACs supports this idea.

To further explore the dependence of the Off response on the loss of the On response, we characterized the time course of adaptation by recording the excitatory currents in On-SACs in response to stationary white spots in between bouts of repetitive stimulation. In dorsal On-SACs, exposure to the repetitive stimulus initially led to an increase in excitatory charge transfer followed by a slow loss of the On response after exposure to ~400 s of the repetitive stimulus. In these cells, the excitatory Off response emerged after 250-350 s exposure to the repetitive stimulus and persisted for as long as the recording (Fig. 2.6E, F, top). In contrast, in ventral On-

SACs we observed a slow loss of the excitatory On response over the course of the recording, but we did not observe an excitatory Off response emerge in these cells (Fig. 2.6E, F, bottom). These data indicate that 1) the Off response is mediated by cones and 2) this cone-mediated Off response emerges only in the absence of a robust On response.

On-cone BCs Mediate Polarity Switch in SACs

To further explore the mechanism that underlies the polarity switch in SACs, we set out to study the source of the Off response gained after repetitive stimulation of dorsal On-SACs. Connectomic reconstructions of the inner retina confirm that On-SACs only receive inputs from On-cone BCs and not from Off-BCs (Helmstaedter et al., 2013) (Fig. 2.6A), and functional glutamate imaging showed limited spillover between On and Off pathways (Borghuis et al., 2013). Before repetitive stimulation, excitatory input onto On-SACs was mediated exclusively via the On pathway, since hyperpolarization of On-cone BCs using the mGluR6 agonist L-AP4 (5 µM; (Slaughter and Miller, 1981)) blocked excitation completely (Fig. 2.8B). Addition of L-AP4 to adapted On-SACs abolished both excitatory and inhibitory inputs in response to light offset (Fig. 2.9A, Fig. 2.8A). These data indicate that the Off response gained after repetitive stimulation originates from the On pathway and not via spillover from the Off pathway (Fig. 2.6A, pathways 4&5).

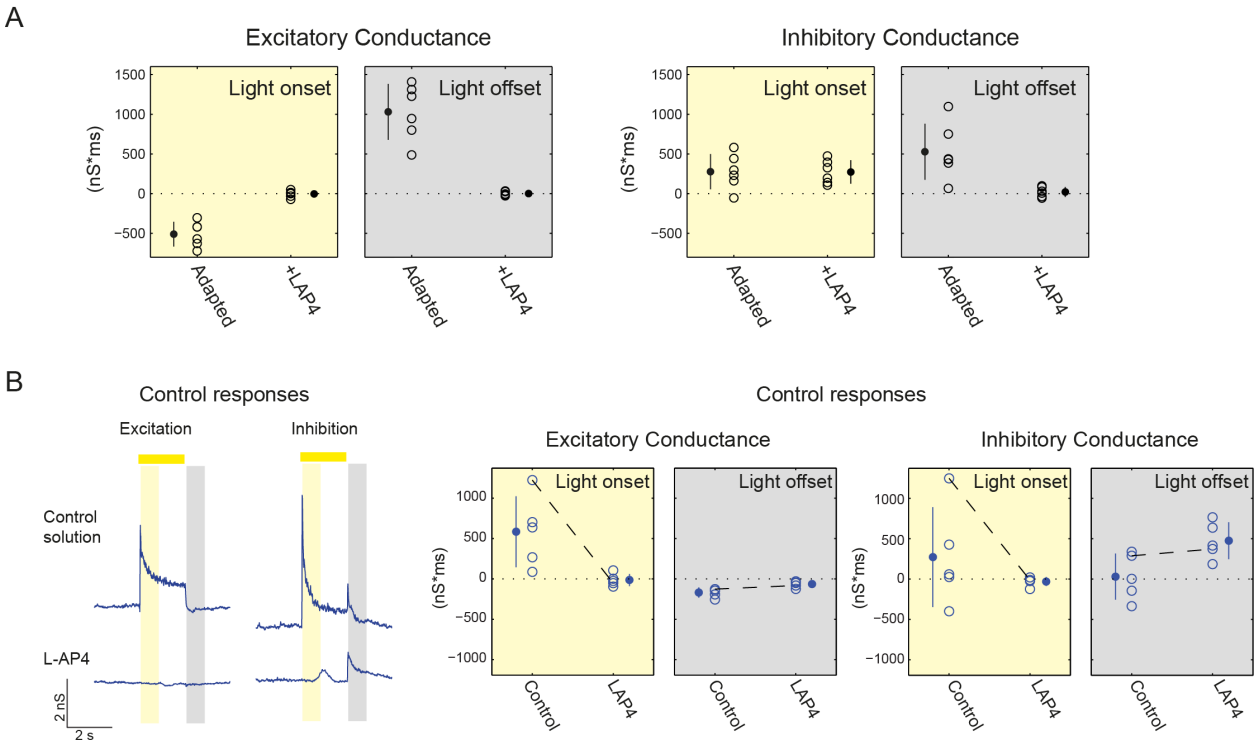

Figure 2.8 **Conductance analysis of control and adapted responses in the presence of L-AP4.** (A) The excitatory (left) and inhibitory (right) integrated conductance at light onset and light offset for adapted On-SACs in control solution and in 5 µM L-AP4. Conventions are as in Figure 2.3E. (B) Left: the excitatory and inhibitory conductance at light onset and light offset for unadapted On-SACs in control solution and in 5 µM L-AP4. Conventions are as in Fig. 2.3C. Right: The excitatory (left) and inhibitory (right) integrated conductance at light onset and light offset for unadapted On-SACs in control solution and after application of 5 µM L-AP4. Conventions are as in Fig. 2.3E.

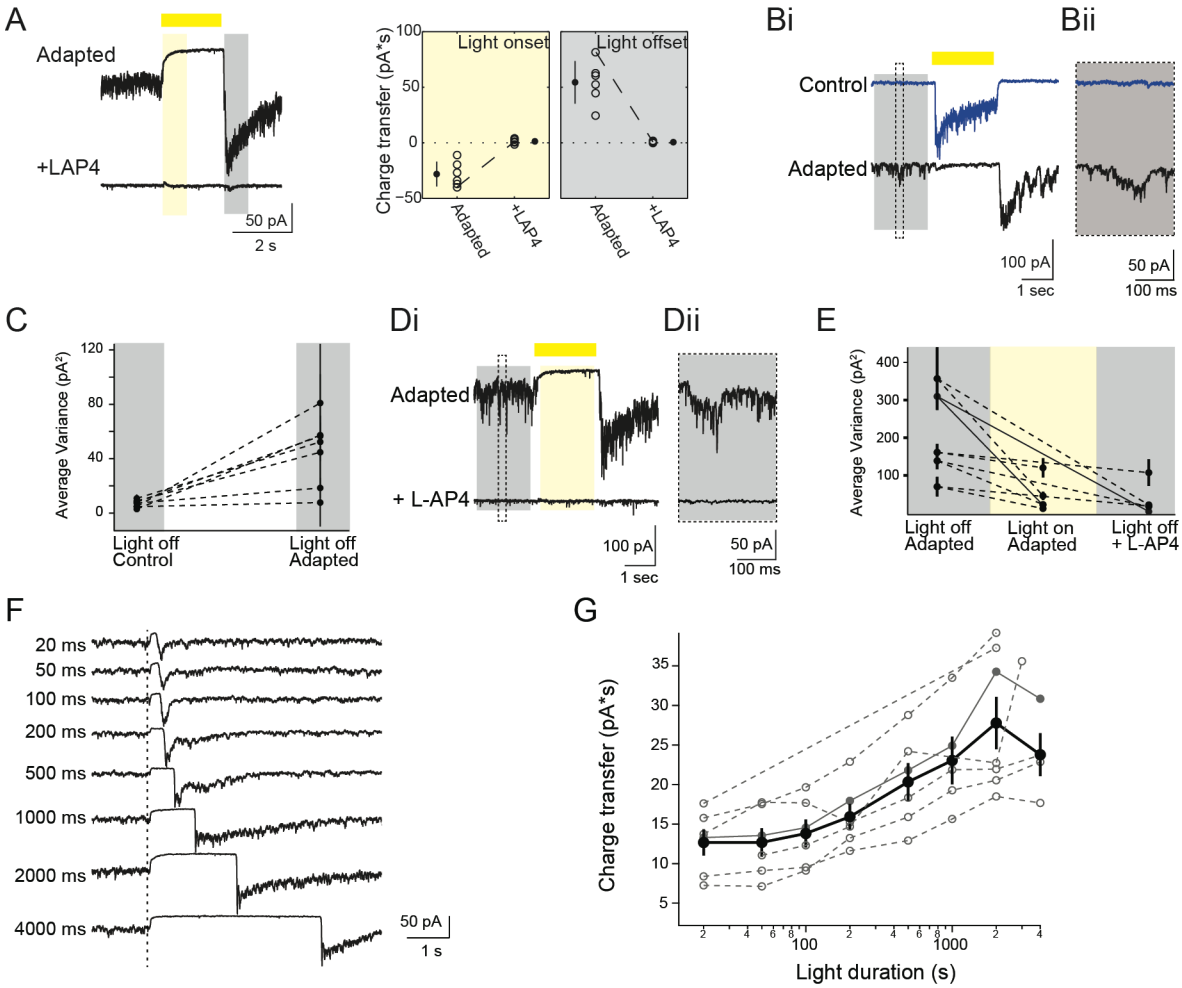

Figure 2.9 **On-cone BCs mediate polarity switch in SACs**
(A) Left: Excitatory current in adapted On-SACs in control solution (top) and after application of 5 µM L-AP4 (bottom) (holding potential = -72 mV). Conventions are as in Figure 2.4B. Right: The excitatory charge transfer at light onset and light offset for adapted On-SACs in control solution and in L-AP4. Conventions are as in Figure 2.4C. (Bi) Individual voltage clamp sweeps at -72 mV holding potential showing the excitatory current during presentation of a 2 s light flash (yellow bar) in an On-SAC before and after repetitive stimulation. The time period used to measure the variance in the holding current quantified in (C) is represented by the grey box. Dotted line indicates the inset in (Bii) showing the spontaneous activity. (C) The variance of the excitatory current of On-SACs (n = 6 cells) during the 1800 ms "light off" period (grey box in (Bi)). For each cell, the average of the variance from 5 sweeps is plotted (black dots) with the standard deviation. (Di) Individual voltage clamp sweeps at -72 mV holding potential showing the excitatory current in an adapted On-SAC during presentation of a 2 s light flash (yellow bar) in control solution (above) and after adding 5 µM L-AP4 (below). Dotted box is the timing of the inset in (Dii) showing the spontaneous activity, the grey rectangle is the time period used for "Light off" analysis in (E) and yellow rectangle is the time period used for "Light on" analysis in (E). (E) The variance of the excitatory current in adapted On-SACs (n = 5 cells) during 1800 ms "light off" and "light on" periods (grey and yellow rectangles in (D), respectably). For each cell, the average of the variance from 5 sweeps is plotted (black dots) with the standard deviation. Solid lines represent the variance for the example cell in (D). (F) Voltage clamp recordings (holding potential = -72 mV) from an On-SAC. Dotted line is the time of light onset. Duration of the light flash is indicated by the time to the left of traces. Traces are averages of five sweeps. (G) Excitatory charge transfer during the 400 ms following the time of the maximum current as a function of light flash duration plotted on a semi-log scale. Open grey circles = individual cells. Closed grey circles = example cell shown in (F). Black circles = average across cells. Error bars = SEM.

Further evidence that the repetitive stimulation alters the On-pathway is the observation that spontaneous glutamate transmission from On-cone BCs changed following adaptation. Exposure to repetitive stimulation significantly increased excitatory spontaneous activity at light offset, as measured by the variance in the holding current (from 6.77±2.74 pA2 to 45.43±24.90 pA2; paired t-test: $p<0.01$; Fig. 2.9B, C), indicating that the adapted On-SACs cells were tonically depolarized in the dark because of tonic glutamate release from On-cone BCs. This elevated level of tonic glutamate release from On-cone BCs onto adapted On-SACs following repetitive stimulation was suppressed by light (Fig. 2.9D, E). By hyperpolarizing On-cone BCs with L-AP4, we abolished tonic glutamate transmission in the dark (Fig. 2.9D, E). These observations confirm that the Off response observed in On-SACs is mediated by glutamate release from On-cone BCs and suggest that, in the adapted state, On-cone BC terminals are depolarized in the dark and hyperpolarized in the light.

A previous study at cone photoreceptor synapses provides an interesting hypothesis as to how suppression of glutamate release during light stimulation can lead to the generation of an Off response. Cone photoreceptors exhibit build-up of glutamatergic vesicles at the ribbon synapse when the light is on; when the light is turned off, this suppression is relieved, and the excess vesicles that have crowded at the bottom of the ribbon are released (Jackman et al., 2009). This model was based in part on the observation that the magnitude of the Off-response was correlated with the length of light-mediated suppression of glutamate release (Jackman et al., 2009). Similarly, we found that the Off excitatory charge transfer following repetitive stimulation increased with increasing stimulus duration, with the effect saturating at longer durations (Fig. 2.9F, G). This supports the idea that the excitatory Off response in adapted On-SACs arises because of suppression of release and accumulation of glutamatergic vesicles during light stimulation at a ribbon synapses, however it does not distinguish whether suppression occurs at BC or at photoreceptor terminals.

Polarity Switch Depends on Changing Contribution of Rod Circuit

The above experiments indicate that the Off response gained following repetitive stimulation is mediated by glutamate release from On-cone bipolar terminals. As noted previously, the Off response gained after repetitive stimulation was observed in dorsal but not ventral retina, indicating that the response originates from cones (Fig. 2.3, 2.6). Cones can influence the membrane potential of On-cone BCs terminals either via their direct, sign-inverting glutamatergic synapse with On-cone BCs (Fig. 2.6A, pathway 3) or through signaling to rods via Cx36-mediated gap junction coupling between rods and cones (Deans et al., 2002) (Fig. 2.6A, pathway 2). This second pathway through rods feeds forward to On-cone BCs via rod BCs that form excitatory synapse onto AII amacrine cells, which in turn are gap junction coupled to On-cone BCs, also via Cx36 gap junctions (Deans et al., 2002; Grimes et al., 2014) (Fig. 2.6A, pathway 1).

To test whether cone signaling through the rod pathway (Fig. 2.6A, pathways 1 and 2) might mediate the change in On-cone BC glutamate release, we repeated the experiment in connexin-36 knock-out (Cx36 KO) mice. Before repetitive stimulation, Cx36 KO mice exhibited a smaller, though not significant, excitatory input at light onset compared to WT (50.7±35.9 in WT mice; 27.7±10.3 pA*s in KO mice; $p=0.13$); after repetitive stimulation, they have a significantly smaller excitatory input at light offset compared to WT (65.5±17.4 in WT mice; 14.3±5.1 pA*s in KO mice; $p<0.01$) (Fig. 2.10A; Fig. 2.11). These findings suggest that through

gap junction coupling, the rod pathway contributes to release from On-cone BCs before and after repetitive stimulation and that the rod pathway not only drives excitatory input onto On-SACs, but also modulates the amplitude of the Off response obtained following adaptation. This is surprising given that repetitive stimulation reduced the rod-mediated On response in ventral retina (Fig. 2.6) and indicates that the rod pathway may contribute via inhibitory feedback from cones (this hypothesis is explored further in the Discussion and Fig. 2.12).

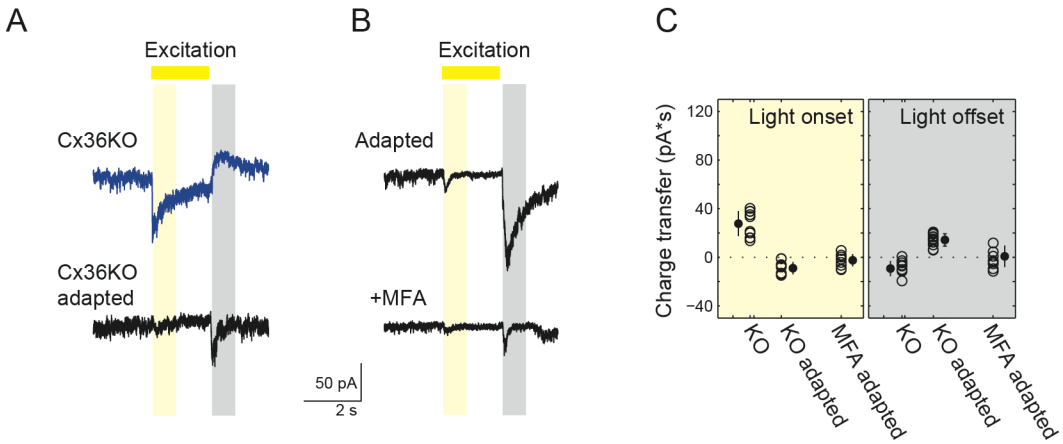

Figure 2.10 **Polarity switch depends on changing contribution of rod circuit** (A) Voltage clamp recordings (holding potential = -72 mV) from an On-SAC from a *Cx36* KO mouse in control conditions (top) and following adaptation (bottom). (B) Voltage clamp recordings (holding potential = -72 mV) from an On-SAC following adaption in control conditions (top) and in the presence of the gap junction antagonist MFA (bottom). (C) The excitatory charge transfer during light onset (yellow) and light offset (grey) in individual On-SACs (circles) from *Cx36* KO retinas before (KO) and after (KO adapted) adaptation; and from WT retinas after adaptation in the presence of 100 µM meclofenamic acid (MFA adapted).

Importantly, while excitation was reduced after repetitive stimulation, On-SACs in Cx36 KO mice still exhibited loss of the On response and gain of the Off response following repetitive stimulation (Fig. 2.10A, C; Fig. 2.11; from 27.7±10.3 in control to -8.9±5.1 pA*s in adapted cells for light onset; $p<0.01$; and from -9.3±6.3 in control to 14.3±5.1 pA*ms in stimulated cell for light offset; $p<0.01$). This suggests that while the rod pathway modulates the amplitude of the Off response following repetitive stimulation, the polarity switch still takes place in the Cx36 KO. Because the AII amacrine cell to On-cone BC electrical synapse is composed of heterologous connexins containing both Cx36 and Cx45 (Dedek et al. 2006), we utilized meclofenamic acid (MFA; 100 µM), a general gap junction blocker, to more completely block gap junction in the rod circuit. In the presence of MFA, the excitatory charge transfer and conductance after repetitive stimulation at light offset was abolished (Fig. 2.10B, C, Fig. 2.11). Note, before repetitive stimulation, addition of 100 µM MFA led to a sharp decrease in excitatory conductance onto On-SACs, consistent with our recordings from the Cx36 KO (Fig. 2.11).

Together, these data indicate that 1) rod-mediated signals comprise a significant component of the On response observed in On-SACs; 2) rod-mediated On signals are lost following adaptation and 3) the generation of the Off-response following repetitive stimulation occurs independently of rod transduction. We propose that the Off response is generated in the bipolar-cell surround by a cone-mediated depolarization of rods (Fig. 2.12), a pathway that

becomes active only following loss of the rod-mediated responses. A full description of this model is presented in the Discussion.

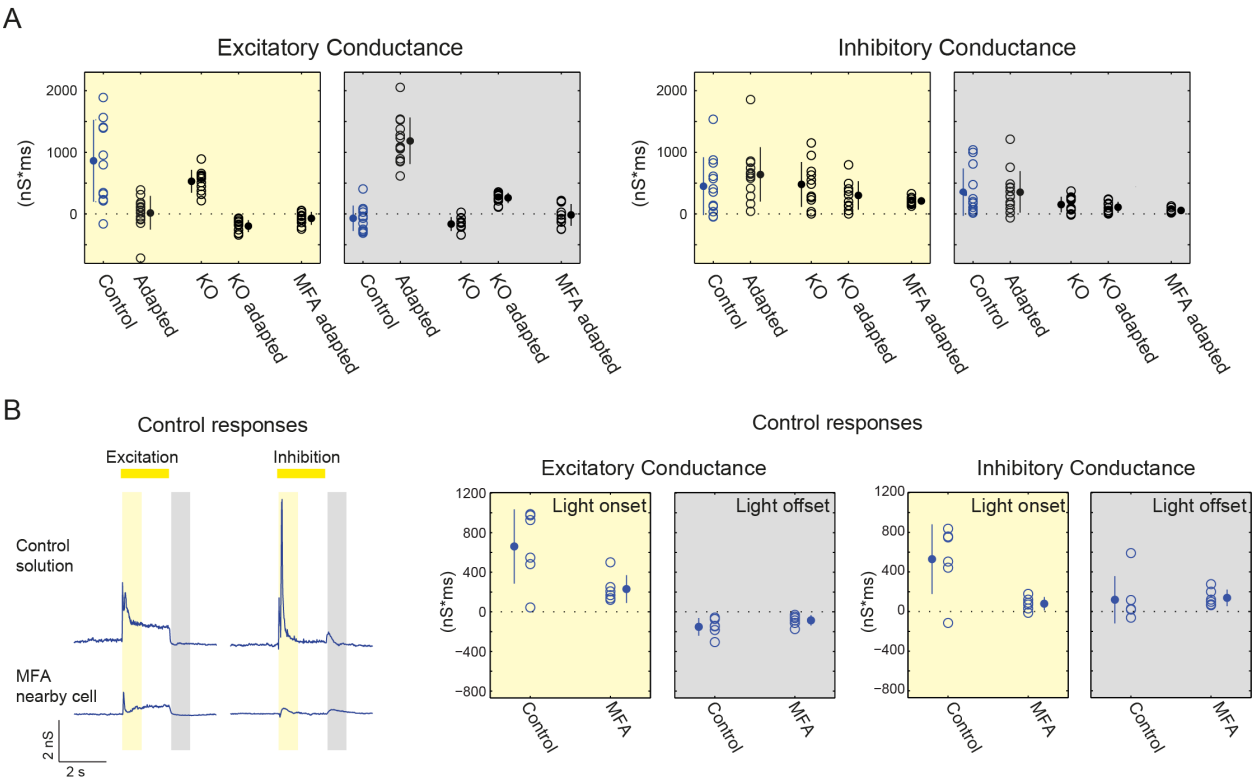

Figure 2.11 **Conductance analysis of control and adapted responses in Cx36 KOs and in MFA.** (A) The excitatory (left) and inhibitory (right) integrated conductance at light onset and light offset for On-SACs in control solution and after adaptation in WT and Cx36 KO retinas, as well as in WT retinas in the presence of 100 µM MFA. Conventions are as in Fig. 2.3E. (B) Left: the excitatory and inhibitory conductance at light onset and light offset for unadapted On-SACs in control solution and in 100 µM MFA. Conventions are as in Fig. 2.3C. Example shown is from two nearby cells. Right: The excitatory (left) and inhibitory (right) integrated conductance at light onset and light offset for unadapted On-SACs in control solution and after application of 100 µM MFA. Conventions are as in Fig. 2.3E.

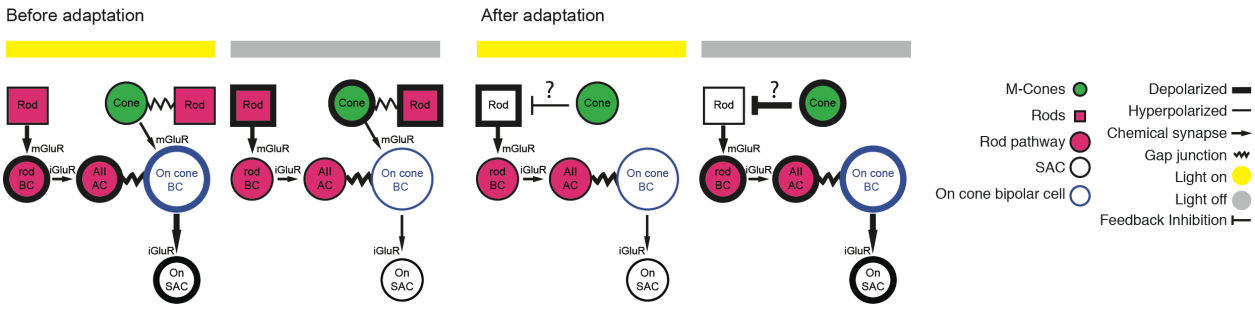

Figure 2.12 **Proposed model of polarity switch in the retinal circuit.** Schematic of circuit that mediates light responses prior to and following adaptation. Details are provided in the Discussion.

SAC Polarity Switch Could Mediate Reversed Tuning of DSGCs

What are the circuit implications for a polarity switch in SACs? Because inhibition from SACs is necessary for the tuning of DSGCs (Fig. 2.1), we hypothesized that the polarity switch in SACs after repetitive stimulation would shift the phase of GABA release relative to a drifting gratings stimulation, and that this phase shift contributes to the reversal of the preferred direction of DSGCs. To test this hypothesis, we created a simulation. We assumed that since there are subtypes of BCs that innervate exclusively SACs but not DSGCs (Helmstaedter et al., 2013), the timing of excitatory input onto DSGCs is not shifted in a similar manner. We simulated the changes in the membrane potential of a DSGC and the spiking activity generated by these changes in response to drifting gratings in the preferred direction (PD) and null direction (ND) (Fig. 2.13). For simplification, the simulation included responses mediated only by the On pathway. Excitatory and inhibitory conductances onto DSGCs were simulated as rectified sinusoids. The excitatory conductance onto DSGCs was similar during both PD and ND drifting grating stimulation, while the inhibitory conductance mediated by On-SACs was continuously shifted in phase relative to excitatory conductance (Park et al., 2014). Prior to repetitive stimulation, the inhibitory conductance in response to ND stimulation was coincident with the excitatory conductance, thereby preventing depolarization in the DSGC. In response to PD stimulation, the inhibitory conductance was delayed relative to excitation, allowing the DSGC to depolarize. We calculated the weighted difference between the spiking in response to PD vs. ND to determine the direction selective index (DSI, see Methods). Before repetitive stimulation, we calculated DSI = 1. We defined this condition as phase shift = 0 (Fig. 2.13A, left).

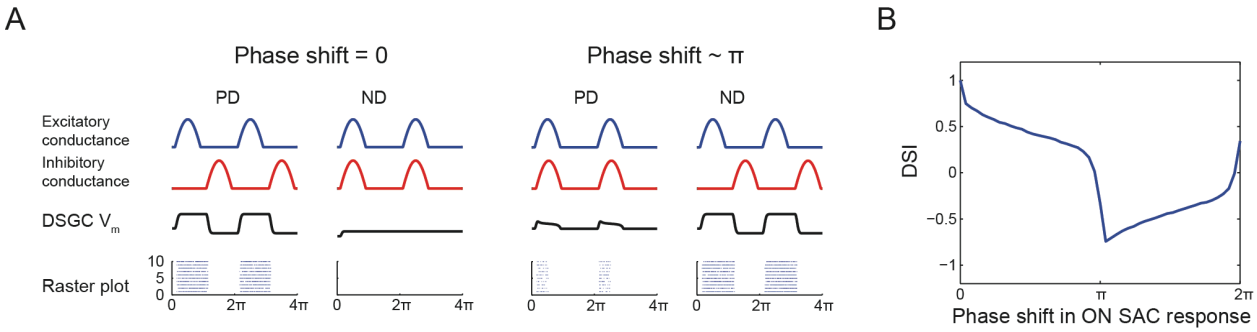

Figure 2.13 **SAC polarity switch could mediate reversed tuning of DSGCs.** (A) Excitatory conductance from On-cone BCs (blue), inhibitory conductance from On-SACs (red) and resulting changes in membrane potential in DSGC (V_m, black) in response to drifting grating in PD and ND (response to 2 phases of grating are shown). Bottom: raster plots depict spiking activity in DSGC randomly generated based on membrane potential values in 10 repetitions of the stimulus. The examples on left and right represent the phase shifts that lead to the maximum and minimum *DSI* values, respectively. Left: phase shift=0, which represents the control non-adapted state. Right: phase shift ~π, which represents the adapted state where inhibitory input is shifted by half a cycle due to polarity switch in On-SAC. (B) DSI as a function of the phase shift between excitatory and inhibitory conductances onto DSGC. DSI values were calculated based on 100 spike trains randomly generated in response to PD and ND stimulation with spiking probability based on DSGC membrane potential. DSI value decreased and became negative for a range of phases around half a cycle shift (i.e. π).

By examining DSI as a function of the phase shift, we found that DSI values were negative for a range of phases around half a cycle shift (π), indicating that the DSGC has

reversed its directional preference for a wide range of phase shifts (Fig. 2.13B). The excitatory and inhibitory conductances onto the DSGC that lead to the minimal DSI value are shown in Fig. 2.13A, right. Here, the inhibitory conductance was half-a-cycle shifted in time relative to excitation resulting in more depolarization in response to ND stimulation. The same temporal shift caused the inhibitory conductance to be synchronous with excitation in response to PD stimulation. This led to a reduced depolarization in response to PD stimulation. Such a phase shift is expected if the SACs have a polarity switch in their phase, i.e., if On-SACs respond to a decrease in light intensity rather than an increase. Furthermore, asymmetric wiring of SACs creates a smaller PD inhibitory conductance, but if phase shifted as in the model, this smaller conductance would be effective enough to shunt the excitatory current on the DSGC (see Fig. 2.4C, D of Rivlin-Etzion 2012). Thus, a polarity switch in SACs postulates a potential contribution for reversed tuning of DSGCs.

Discussion

We demonstrated for the first time that silencing SACs in a reversible manner transiently eliminates direction-selective responses in DSGCs, indicating a requisite role for SAC signaling in the computation of direction selectivity. Furthermore, presenting the retina with a repetitive visual stimulus consisting of drifting gratings, a protocol known to reverse the direction selectivity of DSGCs, caused the excitatory synaptic input to SACs to switch its polarity. The switch occurs independently of GABA-A, C and glycine signaling. Rather, our data suggest that repetitive stimulation leads to a reduction in the On response followed by an increase in cone-mediated signaling that occurs at light offset and leads to an Off response in On-cone BCs. As an example of how these changes in signaling in the outer retina can profoundly alter the response properties in the inner retina, we use modeling to demonstrate how this flip in polarity of SACs may contribute to the reversal in the directional tuning of DSGCs (Rivlin-Etzion et al., 2012).

Mechanism Involves Changes in Circuits in the Outer Retina

The polarity switch in On-SACs is comprised of two components – the loss of the On response and the gain of an Off response. The former occurred in all regions of the retina while the latter occurred exclusively in the dorsal half of the retina. Two key facts allowed us to understand this difference between dorsal and ventral regions. First, there is a gradient of cone opsin expression in the mouse retina, with M-cones dominating in the dorsal retina and S-cones dominating in the ventral retina (Breuninger et al., 2011; Ekesten and Gouras, 2005; Wang et al., 2011). Second, our visual stimuli preferentially activate M-cones and rods, but not S-cones (Wang et al., 2011). This suggests that the gain of the Off response, which only occurred in the dorsal half of the retina, requires cone stimulation, while the loss of the On response, which occurred in both regions of the retina, requires rod saturation.

Several lines of evidence support the idea that a change in rod-cone interactions underlies the polarity switch. First, neither loss of the On response nor gain of the Off response was dependent on depolarization of SACs or inhibitory signaling, ruling out role of crossover, lateral, and feedback inhibition in the inner retina. Second, prior to adaptation, the On response is mediated in large part by rods, as evidenced by its presence in ventral retina and sensitivity to Cx36. Hence, the loss of the On response is consistent with a loss of rod transduction (Wang et al., 2011).

A more interesting scenario underlies the emergence of the Off response gained after repetitive stimulation. First, it was blocked by L-AP4, indicating that it is mediated by the On pathway. Second, the Off response is dependent on the existence of a high level of tonic glutamate release from On-cone BCs, which appears only after the original On-response has decayed. Furthermore, the magnitude of the Off response is correlated with the duration of the light-induced suppression of glutamate release from On-cone BCs, indicating that it is mediated by the relief of this suppression (Jackman et al., 2009).

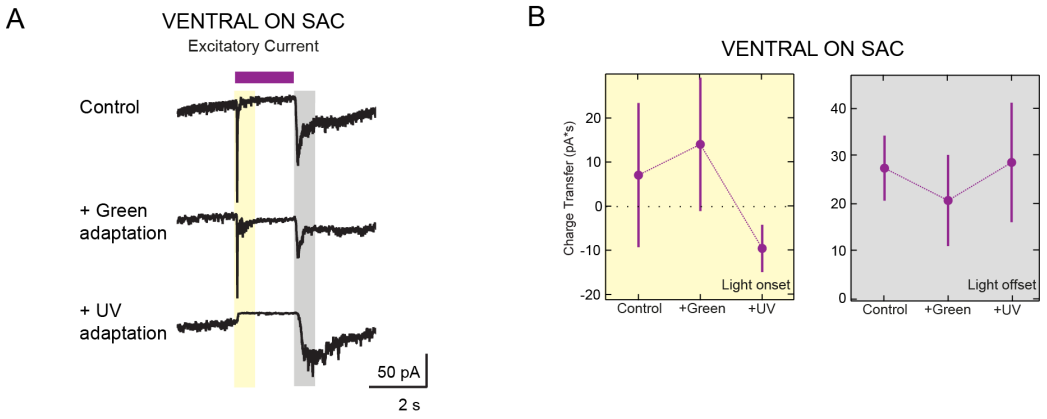

Figure 2.14 **SACs in ventral retina switch polarity after adaptation with UV light.** (A) Voltage clamp recording from an On-SAC in ventral retina showing excitatory current (Holding Potential = -72 mV) in response to a 2 s stationary spot stimulus with UV-wavelength light (purple bar) in control conditions and following exposure to 10 s of Green light ("Green adaptation") followed by exposure to 7 min of UV light ("UV adaptation"). Yellow and grey bars indicate the time periods used for analysis in (B). Traces are averages of 5 sweeps. (B) Charge transfer (averaged over five sweeps) of the excitatory current during light onset (yellow) and light offset (grey) for ventral On-SACs in control conditions and following exposure to 10 s of Green light ("Green") followed by exposure to 7 min of UV light ("UV"). Error bars = SD. N = 5 cells from 2 mice.

To evaluate whether SACs in the ventral retina can switch their polarity, we measured the response to 2 s stationary spots of "UV" light before and after adaptation. Note these experiments were not carried out on a two-photon microscope and therefore the retina piece was exposed to several seconds of bright green light prior to starting the protocol. First, we recorded the spot responses to UV light (Control). Then, to completely saturate the rods, we exposed the cells to steady green light for 10 s. We then recorded the spot response to UV light. Finally, we adapted the cells to steady UV light for 7 min before evaluating the response to UV spots again. We found that On-SACs in the ventral retina exhibited both an On and Off response to UV light spots before adaptation (Fig. 2.14). This initial response was not affected by adaptation with Green light. Subsequent adaptation with UV light led to a loss of the On response, resulting in a spot response similar in kinetics to the adapted responses we recorded in adapted On-SACs in the dorsal retina (see Fig. 2.3). These data are consistent with the model proposed in Figure 2.12 – that the Off response is 1) loss of a rod and cone-mediated On light response and 2) mediated by cone photoreceptors via surround inhibition of rods.

Visual stimuli were transmitted through a 60x objective (Olympus LUMPlanFl/IR 60/0.90W) on a fixed stage microscope (Olympus, BX61WI) using a Xenon Arc Lamp. "UV" and "Green" stimulations were produced using neutral density filters along with a Fura2 filter cube (measured excitation spectrum: 375-400 nm) and YFP filter cube (measured excitation spectrum: 490-510 nm), respectively. Light intensity was 2.9 x 10^6 R*/rod/s (1.54 x 10^7 photons/μm^2/s) for "UV" and 2.28 x 10^8 R*/rod/s (2.28 x 10^8 photons/μm^2/s) for "Green" stimulation. Importantly, the "UV" stimulation provided a 5.38 x 10^6 sOpsin*/sCone/s intensity and therefore primarily activated sOpsin. An aperture in the light path was used to limit light spots to ~220 µm in diameter. To target cells for electrophysiology, GFP immunofluorescence was imaged with a <1 s exposure using a GFP filter cube. The duration of light stimuli used to adapt ventral On-SACs was determined by comparing the light intensity to the light intensity of the OLED used for light adaptation elsewhere and adjusting the duration so that cells were exposed to roughly the same number of total photons.

How does light stimulation suppress release from On-cone BCs in the adapted circuit? Our hypothesis is that prior to adaptation both rods and cones mediated the On response in dorsal retina (Fig. 2.12), while rods primarily mediate the On response in the ventral retina, though the visual stimulation may also activate the low level of M-opsin in cones in the ventral retina (Wang et al., 2011). After adaptation, rods are unable to hyperpolarize in response to light but, in the dorsal retina, they exhibit the opposite polarity response to light as a result of surround inhibition from cones, leading to a hyperpolarization of the On-cone BCs (Fig. 2.12). One consequence of our model is that stimulating cones in the ventral retina with UV light would reveal a polarity switch in ventral On-SACs. Our preliminary findings support this (Fig. 2.14).

We propose that rods flip their polarity due to negative feedback provided by horizontal cells (Babai and Thoreson, 2009) (Fig. 2.12). In this scenario, cones are hyperpolarized by light, which hyperpolarizes horizontal cells. This leads to a depolarization of saturated rods, which cannot hyperpolarize in response to light. In tiger salamander, Off responses in On-cone BCs have also been observed under conditions of high ambient light (Pang et al., 2012). This Off response was mediated by depolarization of rods and was dependent on AMPA receptor signaling. Indeed, a subsequent study demonstrated that rods may depolarize in response to high light levels via a sign-inverting synapse from cones to horizontal cells to rods (Gao et al., 2013), with a similar phenomenon observed in mice (Babai and Thoreson, 2009). Rod depolarization in response to light stimulation would then propagate through the rod–rod BC circuit, suppressing the release of glutamate from the On-cone BC terminal.

Comparison to Adaptation in Rod-Mediated Light Responses

There are a growing number of examples of adaptation that occur at or presynaptic to On-cone BCs. For example, adaptation to stimulus contrast involves changes in the amount of glutamate released from BCs either because of activation of a conductance in the On-cone BC such as Ih (Manookin and Demb, 2006) or because of differing levels of GABAergic feedback (Nikolaev et al., 2013). In addition, the rod pathway adapts to increasing ambient light levels through changes in the contrast sensitivity via AII cells (Ke et al., 2014) as well as changes in the linearity of retinal ganglion cell integration (Grimes et al., 2014).

Importantly, we showed that signaling through gap junctions amplifies the magnitude of the adapted Off response, implicating changes in signaling in the outer retina as the mechanism for the polarity switch. Though some gap junction blockers have known nonspecific effects (for example, see (Vessey et al., 2004)), MFA has been demonstrated to functionally block gap junctions without blocking other conductances (Veruki and Hartveit, 2002). Interestingly, gap junctions were found to play a role in reversal of directional preference of On-DSGCs following GABA blockade (Ackert et al. 2009).

Examples of "switches" in retinal circuits

Classically, adaptation has been described as a continuous adjustment to changing statistics of the visual scene. However, more recently, various forms of adaptation in the retina are referred to as "switches", abrupt transitions in circuits as a continuous variable in the environment is changed. First, altering the ambient lights levels can lead to an abrupt change in center-surround properties (Barlow et al., 1957; Farrow et al., 2013). Second, increasing ambient light levels leads to a switch in inner retinal circuits (Grimes et al. 2014), which changes the spatial

integration properties of the ganglion cell, referred by the authors as "repurposing". Finally, PV-5 Off ganglion cells become approach-sensitive in bright light levels and On-Off DSGCs reverse their directional preference following adaptation (Münch et al., 2009; Rivlin-Etzion et al., 2012).

While the segregation between On and Off pathways is one of the most well known examples of parallel processing in the retina (Wassle, 2004), there is accumulating evidence of interactions between them. Several studies have reported that On-ganglion cells reveal an Off response during blockade of inhibition (Ackert et al., 2009; Nirenberg and Meister, 1997) and Off-ganglion cells display an On response (Farajian et al., 2011; Rentería et al., 2006). On the contrary, the polarity switch we observe is generated by visual stimulation and persists in the absence of normal inhibitory signals. In tiger salamander, an Off-RGC switches its polarity in response to stimulation in the periphery (Geffen et al., 2007). This switch lasts roughly 100 ms and is mediated by a wide-field amacrine cell that releases GABA in response to shifts in the visual scene that occur during a normal saccade. Importantly, the rapid switch does not contradict the anatomy of the cells, as Geffen and colleges classify these switching cells as having On-Off ganglion cells morphology (Geffen et al., 2007).

The physiological implications of the functional switches we observe following adaptation have yet to be determined. An intriguing possible consequence would be that direction selective cortical neurons inherit their adaptive properties from retinal DSGCs (Kohn and Movshon, 2004; Priebe et al., 2010). This hypothesis is supported by recent findings that there is a di-synaptic circuit linking DSGCs to the superficial layers of primary visual cortex (Cruz-Martín et al., 2014). Yet, since our preparation is separated from the pigment epithelium, saturated rods cannot recover and hence our experiment might model a physiological state in which rods are not active. Notably, our results demonstrate that computations performed by anatomically-defined neuronal circuits are subject to change following circuit perturbations, emphasizing the necessity of studying both anatomy and physiology while varying the sensory input.

SAC Polarity Switch May Contribute to Reversed Directional Preference of DSGCs

The drifting grating stimulus that induced the polarity switch in this study was chosen because of its ability to reverse the directional preference described in DSGCs (Rivlin-Etzion et al., 2012). However, the cellular and synaptic interactions that link signaling from SACs to DSGCs are complex, with the critical computations occurring at the subcellular level (Taylor and Smith, 2012). Notably, release of GABA is the result of dendritic integration that occurs locally within each SAC process and therefore cannot be assessed with whole cell recording (Euler et al., 2002).

To explore how a polarity switch could contribute to the reversal of DSGC tuning, we provide a simple model demonstrating how a polarity switch in SACs alters the timing of GABA release relative to the release of glutamate. Based on our results, one interesting prediction is that in ventral retina, where we observed a loss of the On response but no gain of the Off response, we would expect DSGCs to not reverse their directional preference. A re-analysis of the data from Rivlin-Etzion et al. matched this prediction: DSGCs located in the dorsal retina that were exposed to 200-300 s of the repetitive stimulus (note that not all SACs have switched polarity by this time point; Fig. 2.4) were more likely to reverse their direction preference than DSGCs in ventral retina, which were more likely to remain stably-tuned (52% of 41 DSGCs in dorsal retina reversed while 21% of 29 DSGCs in ventral retina reversed; 23% of DSGCs in dorsal retina

remained stable while 66% of DSGCs in ventral retina remained stable). Note this model does not take into account the observation that repetitive stimulation altered the tuning of inhibition, also described in (Rivlin-Etzion et al., 2012).

In conclusion, our data represent a dramatic and surprising example of how computations performed by well-defined anatomical circuits depend not only on the wiring diagram between the neurons, but also on the functional connectivity (Bargmann and Marder, 2013) and the visual environment.

Chapter III

A Role for Synaptic Input Distribution in a Dendritic Computation of Motion Direction in the Retina

This Chapter is a full reprint of Vlasits et al., *Neuron* (2016), in which I was the primary author. The work is included with permission from all authors.

Relevant publication:

Vlasits, A.L., Morrie, R.D., Tran-Van-Minh, A., Bleckert, A., Gainer, C.F., DiGregorio, D.A., and Feller, M.B. (2016). A Role for Synaptic Input Distribution in a Dendritic Computation of Motion Direction in the Retina. *Neuron* 89, 1317–1330.

Abstract

The starburst amacrine cell in the mouse retina presents an opportunity to examine the precise role of sensory input location on neuronal computations. Using visual receptive field mapping, glutamate uncaging, two-photon Ca2+ imaging, and genetic labeling of putative synapses, we identify a unique arrangement of excitatory inputs and neurotransmitter release sites on starburst amacrine cell dendrites: the excitatory input distribution is skewed away from the release sites. By comparing computational simulations with Ca2+ transients recorded near release sites, we show that this anatomical arrangement of inputs and outputs supports a dendritic mechanism for computing motion direction. Direction selective Ca2+ transients persist in the presence of a GABA-A receptor antagonist, though the directional tuning is reduced. These results indicate a synergistic interaction between dendritic and circuit mechanisms for generating direction selectivity in the starburst amacrine cell.

Introduction

Starburst amacrine cells (SACs) are axonless GABAergic interneurons, whose release sites are located in the distal tips of their dendrites. SACs play a critical in the computations of direction selectivity by providing asymmetric inhibition onto direction selective ganglion cells (DSGCs), which fire selectively to motion in one direction and very little to motion in the other direction (Amthor et al., 2002; Fried et al., 2002, 2005; Vlasits et al., 2014; Yoshida et al., 2001). The mechanism of direction selective inhibition from SACs has been widely studied. DSGCs receive greater inhibitory input from SACs located on their "null side" (Fried et al., 2002; Wei et al., 2011; Yonehara et al., 2011) due to selective wiring of inhibitory synapses from SAC dendrites pointed in the DSGC's null direction (Beier et al., 2013; Briggman et al., 2011; Morrie and Feller, 2015). But wiring cannot by itself explain direction selective inhibition, because DSGCs exhibit DS even when moving stimuli are restricted to a small region of the receptive field (Fried et al., 2002). Therefore, GABA release from SAC dendrites must also be DS. Indeed, individual SAC dendrites prefer motion in different directions. Specifically, Ca2+ transients in SAC dendrites are larger in response to motion outward from the soma to the end of the dendrite compared to motion inward from the end of the dendrite to the soma (Euler et al., 2002; Hausselt et al., 2007; Lee and Zhou, 2006; Yonehara et al., 2013). SACs receive excitatory input from bipolar cells, glutamatergic interneurons that are the major feed-forward circuit component in the retina. But bipolar cell axon terminals exhibit neither DS Ca2+ transients (Chen et al., 2014; Yonehara et al., 2013) nor DS glutamate release onto DSGCs (Park et al., 2014). This suggests that the first computation of motion direction takes place in SAC dendrites.

Currently, there are three hypotheses of how direction selective calcium signals arise in SAC dendrites. The first hypothesis is that integration of spatially-offset bipolar cell inputs with different release kinetics produces DS (Kim et al., 2014). The second is that circuit-level reciprocal lateral inhibition between SACs creates a preference for outward motion in the absence of dendrite-intrinsic asymmetries (Lee and Zhou, 2006; Münch and Werblin, 2006). The third is a dendrite-intrinsic mechanism, which proposes that passive properties of SAC dendrites, combined with non-linear conductances, are capable of computing motion direction (see Vaney et al., 2012 for review). However, the precise dendritic computations would depend on the arrangement of input and output sites. Outputs (GABA release sites) are located in the distal 1/3 of the SAC dendrite, where widenings called varicosities contact DSGCs (Briggman et al., 2011;

Famiglietti, 1991). On the other hand, different distributions of excitatory inputs have been proposed in the SAC dendritic arbor: either inputs cover the entire arbor (Famiglietti, 1991; Koizumi et al., 2011) or there are fewer inputs in the distal dendrites (Greene et al., 2016; Kim et al., 2014).

Here, we determined the dendritic locations of excitatory synaptic inputs to elucidate the dendrite-intrinsic mechanisms that play a role in SAC computations. We utilized several methods to examine the excitatory input distribution: visual receptive field mapping, localized glutamate uncaging, and labeling of the PSD95 distribution. In addition, we modeled the SAC to explore the effect of changing the input distribution on the voltage responses in different regions of the dendrite. Finally, we used two-photon Ca2+ imaging of varicosities to determine the relative contributions of excitation and lateral inhibition to the direction selective computation in SAC dendrites.

Methods

Visual stimulation and calcium imaging

Ethics Statement:
All animal procedures were approved by the UC Berkeley Institutional Animal Care and Use Committee and conformed to the NIH Guide for the Care and Use of Laboratory Animals, the Public Health Service Policy, and the SFN Policy on the Use of Animals in Neuroscience Research.

Tissue Preparation:
Adult mice (P21-P40) of either sex were anesthetized with isoflurane and decapitated. Retinas were dissected from enucleated eyes under infrared illumination and isolated retinas were mounted over a 1-2 mm2 hole in filter paper (Millipore) with the photoreceptor layer side down. Mounted retinas were stored in oxygenated Ames' media (US Biological or Sigma) in the dark at room temperature prior to imaging and recording. To target SACs for whole cell recordings, we used two mouse lines that express fluorescent proteins in SACs: mGluR2-GFP mice that contain a transgene insertion of the interleukin-2 receptor fused to GFP under control of the mGluR2 promoter (Watanabe et al., 1998); and ChAT-Cre/nGFP mice generated by crossing a mouse in which IRES-Cre recombinase was knocked in downstream of the endogenous choline acetyltransferase gene (Ivanova et al., 2010) (B6.129S6-ChATtm2(cre)Lowl/J; Jackson Labs) (Chat-cre) with a mouse line containing a loxP-flanked STOP cassette upstream of the GFP gene containing a nuclear-localization sequence (Stoller et al., 2008) (B6.129-Gt(ROSA)26Sortm1Joe/J; Jackson Labs). For some experiments, ChAT-Cre mice without the nGFP transgene or wild-type (C57BL/6J; Jackson Labs) mice were used. In these experiments SAC identity was confirmed by fluorescence imaging of dye-filled cells at the end of the experiment.

Whole Cell Recordings:
All recordings in this study were performed from displaced (On-layer) SACs. Retinas mounted on filter paper were placed under the microscope and perfused with oxygenated (95% O2 – 5% CO2), bicarbonate-buffered Ames' media at 32-34°C. For calcium imaging experiments, L-ascorbic acid (Sigma) was added to Ames' media to achieve a final concentration of 0.5 mM. For

experiments in Fig. 3.14, SR 95531 hydrobromide (GABAzine, Tocris Bioscience), was added to Ames' media to achieve a final concentration of 5 μM. Retinas were bathed in GABAzine-containing Ames' media for ≥ 10 minutes before recording from SACs.

To avoid bleaching the photoreceptors, fluorescently labeled retinal cells were targeted for whole cell recordings using two-photon microscopy (see 2-photon imaging below) (Wei et al., 2010). For placing the patch pipette on the cell soma, the tissue was visualized using transmitted infrared illumination with an IR-LED (Thor Labs) and an IR1000 camera (DAGE-MTI). The inner limiting membrane and Müller cell endfeet above the targeted fluorescent cell were removed using a glass pipette before targeting a new pipette for recording. In all instances a gigaohm seal was obtained before breaking in.

For whole cell voltage clamp recordings, borosilicate glass electrodes pulled to a 5-7MΩ tip were filled with an internal solution containing (in mM): 110 CsMeSO3, 2.8 NaCl, 4 EGTA, 5 TEA-Cl, 4 adenosine 5'-triphosphate (magnesium salt), 0.3 guanosine 5'-triphosphate (trisodium salt), 20 HEPES, 10 phosphocreatine (disodium salt), and CsOH to pH 7.2. Alexa Fluor 594 hydrazide (0.03 mM, Life Technologies, #A-10438) was included in internal solution for collecting 2-photon images of dendritic morphology after the visual stimulation protocol was complete. Voltage clamp recordings were acquired at 10 kHz and filtered at 2 kHz with a Multiclamp 700A amplifier (Molecular Devices) using pCLAMP 10 recording software and a Digidata 1440 digitizer. Currents were recorded at only one holding potential (-72 mV). The holding potentials reported throughout are after correction for the junction potential (-12 mV).
For calcium imaging experiments, electrodes were filled with an internal solution containing (in mM): 116 D-gluconic acid (K+ salt), 6 KCl, 2 NaCl, 20 HEPES, 4 adenosine 5'-triphosphate (magnesium salt), 0.3 guanosine 5'-triphosphate (trisodium salt), 10 phosphocreatine (disodium salt), 0.15 Oregon Green 488 BAPTA-1 hexapostassium salt (OGB-1; Life Technologies) and KOH to pH 7.25. Membrane potentials reported here are after correction for the liquid junction potential (-8.6mV) Cells were held in current clamp for calcium imaging experiments and recordings were acquired at 10kHz. Cells resting above -48 mV were injected with negative current (maximum -150 pA) to achieve a resting potential < -48mV. Cells that did not hyperpolarize below -48mV upon current injection were discarded from analysis.

2-photon Imaging:
Targeted patching of GFP-expressing cells and imaging of Alexa-594 and OGB-1 dye-filled SACs were performed using a custom-built two-photon microscope. We used a Chameleon Ultra II laser (Coherent) tuned to 810 nm (for Alexa-594 dye imaging) or 930 nm (for GFP and OGB-1 imaging) focused through a 60x LUMPlanFL N water-immersion objective (1.00 NA, Olympus). A 20x UMPlanFL N water-immersion objective (0.50 NA, Olympus) was used for imaging the entire SAC dendritic tree. Laser intensity was controlled using a Pockels cell (Conoptics), scanning was performed using a 3 mm XY Galvanometer scanner (Edmund Optics), and the fluorescence was collected with photomultiplier tubes (H10770PA-40, Hamamatsu). The average sample plane laser power measured after the objective was 6.5-13 mW. The imaging system was controlled by ScanImage software (www.scanimage.org).

For Ca2+ imaging experiments, OGB-1 visualization was performed at 930 nm to reduce the light response of the retina during scanning (Denk and Detwiler, 1999). After break-in, the distal end of a dendrite, as well as a single varicosity on that dendrite, were identified as quickly as possible with minimal exposure to the 2-photon laser (6±2 minutes after break in). A small region of interest (2-6 μm2) that included the varicosity was imaged at either 5.92 or 11.84 Hz

(64 x 64 pixels) (see Visual Stimulation below). Unlike Hausselt et al. (2007), we saw that a majority (61%) of our patched SACs had Ca2+ responses to light stimuli, although long whole cell recording times (>~20 minutes), as well as prolonged laser and/or visual stimulation exposure, often led to unreliable Ca2+ responses. These included changes in SAC response polarity (Vlasits et al., 2014), as assessed by the electrical current clamp recording, as well as reduction in fluorescent signal and light responsiveness. Cells were discarded from analysis if the response polarity changed during the imaging session or if the responses to stimuli were lower than 2 S.D. above the noise. Overall, 39% of cells for which a recording was achieved were discarded for the reasons stated above.

Visual Stimulation:

For visual receptive field mapping using voltage clamp, visual stimuli were generated using a computer running an Intel core duo processor with Windows XP running a monochromatic organic light-emitting display (OLED-XL, eMagin, 800 x 600 pixel resolution, 85 Hz refresh rate). For simultaneous calcium imaging and visual stimulation, visual stimuli were generated using a computer running an Intel core duo processor with Ubuntu (v. 14.04.2, "Trusty Tahr") running a DMD projector (Cel5500-Fiber, Digital Light Innovations, 1024 x 768 pixel resolution, 60 Hz refresh rate) and an LED light source (M470L2, Thorlabs, Inc.). Visual stimuli were filtered to project only wavelengths between 480-490 nm. The OLED or DMD was projected through a condenser lens onto the photoreceptor-side of the sample. For the OLED, the maximum size of the projected image on the retina was 800 x 600 μm. For the DMD, the maximum size of the projected image on the retina was 670 μm x 500 μm. Custom stimuli were developed using Matlab or GNU Octave and the Psychophysics Toolbox. Proper alignment of stimuli in all planes was checked each day prior to performing the experiment. First, a pipette filled with fluorescent dye was inserted into the bath at the focal plane of the retinal photoreceptors in our chamber (empirically measured using IR imaging (see Whole Cell Recordings)). The tip of the pipette was used to find the center of the 2-photon image and align it to a point in the image from the IR1000 camera used for patching. A 5 μm radius spot was then projected through the condenser and detected directly with the IR1000 camera. To align the stimulus to the tip of the pipette (center point of the 2-photon image) any misalignments in the z-plane were corrected by focusing the condenser, while those in the x-y plane were corrected by shifting the condenser along the horizontal axes.

For visual receptive field mapping with voltage clamp, we presented 4 repetitions of each stationary spot (12.5 μm radius) position at maximum intensity (2.9 x 105 R*/rod/s) on a grey background (1.4 x 104 R*/rod/s) for 1 s with 2 s between each spot. For rings, we presented 4 repetitions of each ring radius at maximum intensity (2.9 x 105 R*/rod/s) on a grey background (8.3 x 104 R*/rod/s) for 1 s with 2 s between each ring. For rings and spots, we allowed the retina to adapt to the background illumination for 30 s before beginning data collection. After the experiment was performed a 1 μm/slice z-stack of the dye-filled dendritic arbor was acquired to determine stimuli locations.

For simultaneous calcium imaging and visual stimulation, we first calculated the dendritic radius of a SAC using measurement tools in ImageJ on images of the dye-filled arbor and soma taken within 15 minutes of break-in (See Data Analysis for radius calculations). For Fig. 3.3, we presented 3 repetitions of the same sized stationary spot (12.5μm radius) (1.9 x 105 R*/rod/s) on a black background for 1 s with 6 s between each spot. Spots were centered on the 25-100% dendritic radius locations previously calculated from ImageJ. For measuring direction

selectivity (Fig. 3.11), we presented a 25 μm x 25μm square moving at 500 μm/s. For outward moving squares, the stimulus originated centered on the soma and moved a distance of 75 or 100% of the dendritic radius. Inward stimuli began centered at either 75% or 100% of the dendritic radius and moved inward to the soma. For both these experiments, the relative visual stimulus location along the SAC arbor was verified, and post-hoc corrected if necessary, using a maximum intensity projection image of a 0.5 um/slice z-stack of the quadrant of the filled SAC containing the region of interest imaged. The stack was acquired with the laser tuned to 800 nm (16 mW sample plane power) to take advantage of the larger 2-photon cross-section of OGB at this wavelength. For all visual stimulation experiments, stimuli were presented in pseudorandom order.

Data Analysis:

Data analysis of physiological recordings was performed in IgorPro (WaveMetrics) running Neuromatic functions. Reported responses are the averages over the 4 repetitions of each stimulus position/radius. The excitatory charge transfer of visually-evoked events was calculated by integrating the average current over the entire 1 s period of the stimulus and subtracting the background charge measured during the 1 s prior to stimulus presentation. For spots, the charge transfer was normalized to the charge transfer measured at the soma as this was usually the maximum response (Fig. 3.1B-E). For rings, the charge transfer was normalized to the maximum charge transfer (Fig. 3.1F-I). For spots, the receptive field was defined as the % of the dendritic field at which the normalized charge transfer reached <5% of the charge transfer at the soma. For rings, the receptive field was defined as the % of the dendritic field at which the normalized charge transfer reached <0% of the maximum charge transfer.

Measurements of the extent of the SAC dendritic field were performed in ImageJ. Measurements were taken from the maximum intensity projection of images of the SAC. The dendritic field with stationary spot stimuli (Fig. 3.1B-E) was the radius from the center of the soma to the edge of the longest dendrite within the region of the cell covered by the stimuli. The dendritic field with ring stimuli (Fig. 3.1F-I), was the radius from the center of the soma to the end of the longest dendrite in the entire dendritic tree. The dendritic field for Ca2+ imaging experiments was the radius from the center of the soma through the imaged varicosity to the edge of the longest dendrite within the region of the cell covered by the stimuli. Path lengths were calculated using the segmented line function in ImageJ to trace the dendritic path from the soma through the imaged varicosity to the tip of that dendrite.

Analysis of the calcium imaging experiments was performed in MATLAB and IgorPro using custom procedures. Images of varicosities were segmented by Multi Otsu's method. In brief, time-lapse images from a single stimulation experiment were combined by maximum intensity projection. The bottom class of each thresholded projection was then assigned as background, while the top class was used as a mask for further analysis. The pixel intensities for pixels within a mask were averaged at each time step. The average background intensity was subtracted and the change in fluorescence responses shown here were calculated as

$$\frac{\Delta F}{F} = \frac{F - F_0}{F_0}$$

where F is the fluorescence during visual stimulation and F0 is the average fluorescence during the 3 s preceding visual stimulation. The maximum ΔF/F for each average response was used to

calculate the direction selectivity index as follows (with direction of visual stimulation relative to SAC soma indicated by the subscript):

$$DSI = \frac{\frac{\Delta F}{F}_{out} - \frac{\Delta F}{F}_{in}}{\frac{\Delta F}{F}_{out} + \frac{\Delta F}{F}_{in}}$$

Glutamate Uncaging

Ethics Statement:
Animal experiments were performed in accordance with the guidelines of Institut Pasteur.

Tissue Preparation:
Tissue was prepared as described for visual stimulation (above) with the exception that dissections of the retina were done in ambient light and tissue was stored in oxygenated ACSF containing (in mM): 125 NaCl, 2.5 KCl, 1 CaCl2, 1 MgCl2, 1.25 NaH2PO4, 25 NaHCO3, and 25 glucose. We recorded from wild type (C57Bl/6) mice. To target On-SACs in wild type mice, we filled cells with small, round somas (Petit-Jacques et al., 2005) with Alexa Fluor 594 in the internal solution and imaged the dendritic morphology using a 2-photon microscope to determine cell identity before proceeding.

Voltage Clamp Recordings:
Whole-cell recordings were made from SACs at -72 mV at near physiological temperatures (32°C) using a Multiclamp 700B amplifier (Axon Instruments, Foster City, Ca, USA) with thick-walled glass patch-electrodes (tip resistances of 5-8 MΩ) that were backfilled with either a K+-based internal solution containing (in mM): 117 K-MeSO3, 40 HEPES, 6 NaOH, 5 EGTA, 1.78 CaCl2, 4 MgCl2, 0.3 NaGTP, 4 NaATP, and 0.03 Alexa 594 or a Cs+- based internal solution containing (in mM): 90 Cs-MeSO3, 40 HEPES, 6 NaOH, 10 BAPTA, 3.4 CaCl2, 5 MgCl2, 10 TEA-Cl, 0.3 NaGTP, 4 NaATP, and 0.03 Alexa 594, adjusted to ~305 mOsm and pH 7.3. The series resistance was typically below 35 MΩ and was not compensated. Unless otherwise noted, for recording, the ACSF was supplemented with 2 µM L-AP4 and 1.2 µM LY341495 to block the light response from photoreceptors (Ala-Laurila et al., 2011) in addition to 2 mM MNI-glutamate. Uncaging-evoked events were filtered at 10 kHz and digitized at 100-500 kHz using an analogue-to-digital converter (model NI USB 6259, National Instruments, Austin, TX, USA) and acquired with Nclamp (www.neuromatic.thinkrandom.com).

2-photon Imaging:
SAC somata were identified and whole-cell patched using infrared Dodt contrast (Luigs and Neumann, Ratingen, Germany) and a frame transfer CCD camera (Scion Corporation, Cairn Research Ltd, Faversham, UK). These components were mounted on an Ultima two-photon laser scanning head (Prairie Technologies, Middleton, WI, USA) based on an Olympus BX61W1 microscope, equipped with a water- immersion objective (60x, 1.1 numerical aperture, Olympus Optical, Tokyo, Japan). Two-photon excitation was performed with a pulsed Ti:Sapphire laser (DeepSee, Spectra-Physics, Evry, France) tuned to 810 nm. The SAC morphology was visualized from maximal intensity projections of 2PLSM images (0.261 µm/pixel, and 1 µm in Z-dimension) to find isolated dendrites for uncaging. 100 nm diameter fluorescent beads

(Invitrogen, Carlsbad, CA, USA) were used to estimate the point spread function (PSF) of the microscope system as previously described (Abrahamsson et al., 2012; DiGregorio et al., 2007). The measured PSF had lateral and axial dimensions of 390 ± 5 nm (FWHM, n = 15) and 1430 ± 40 nm (n = 14), respectively.

Glutamate Uncaging:

The caged compound 4-methoxy-7-nitroindolinyl-caged L-glutamate (MNI-glutamate, Tocris Bioscience) was bath applied at a concentration of 2 mM (in ACSF). The custom photolysis system was coupled into the photolysis pathway of the Ultima two-photon scanhead. A 405 nm diode laser (Omicron Lasers, Rodgau, Germany) beam was coupled to the microscope using a single mode optical fiber (Oz Optics, Ottawa, Ontario, Canada) similar to a previously described setup (DiGregorio et al., 2007), except additional optics were used to adjust the convergence angle to both backfill the objective and match the focal plane of the two photon excitation for imaging (810 nm). Parfocality of the two wavelengths was verified previously (Abrahamsson et al., 2012). Photolysis laser powers were 2.55 mW.

To map putative postsynaptic sites along a dendrite (Fig. 3.4), we uncaged at dendritic locations 2.5-4 μm apart at 100 or 200 ms intervals and measured current responses to uncaging in voltage clamp. In one cell, we uncaged inward from the distal dendrite to the soma and did not observe any differences in measured parameters (data not shown). Uncaging-based mapping was performed using 100 μs duration laser pulses, a duration shown to optimize event detection and resolution (see Fig. 3.5). The effective uncaging resolution was measured by uncaging systematically in locations 0.5 – 1 μm along a line perpendicular to a synaptic location determined via mapping (Fig. 3.6). For all experiments, uncaging pulses in neighboring locations were timed 100 or 200 ms apart, which was enough time to ensure that nearby glutamate receptors were no longer desensitized (Fig. 3.5). Depending on flatness of the sample, the objective was refocused between bouts of uncaging to only uncage on in-focus sections of the dendrite. Because SAC dendrites lie in a relatively flat plane, tissue depth was fairly constant across uncaging locations, though because of slight changes in depth of the dendrites in the inner plexiform layer, we cannot make major conclusions about receptor number or dendritic filtering using amplitudes of events measured here.

Data Analysis:

Data analysis of uncaging-evoked events was performed in IgorPro (WaveMetrics) running Neuromatic functions. Using event detection combined with selection of events with locally-maximal amplitudes, we determined the events we thought were putative postsynaptic sites (Fig. 3.5).

For event detection, uncaging-evoked events were defined as having an amplitude greater than 6 times the S.D. measured during the 3 ms prior to uncaging. This criterion was found to be sufficient to exclude noise due to spontaneous activity from being included. The amplitude was defined as the maximum current during the 10 ms after uncaging. The rise time was the time period from 10% to 90% of the amplitude.

For analyzing the resolution of uncaging, we evaluated the event found to have the maximum amplitude to determine the time point for evaluating the amplitude of other events in the series. These amplitudes were then fit to a Gaussian distribution and the FWHM of the distribution was measured to determine the resolution of uncaging.

The paired-pulse ratio was defined as the amplitude of the second uncaging event divided by the first event.

To determine the location of putative postsynaptic sites from uncaging-evoked events, we selected the events of local maximal amplitude within 5 μm from the set of events detected using the event detection procedure described above (Fig. 3.5). For events proximal to the soma, events with locally maximal amplitude almost always had locally minimal rise times, while for events distal to the soma this was not the case (Fig. 3.5).

The path length from the soma to the location of the uncaging sites was determined in ImageJ. Measurements were taken from the maximum intensity projection of images of the SAC (stacks taken in 1 μm z-steps). We traced the path from the center of the soma to most distal uncaging site recorded in an image during the experiment identified based on the local anatomical features. Then, we extrapolated backward from this site to the soma to determine the location of all other sites using our records of the distance between sites measured during the experiment. For analyses using the radius from the soma to distal uncaging sites, we measured the radius using a straight line from the soma center to the anatomical location of the most distal uncaging site. The dendritic field was measured from a straight line from soma center to the end of the dendrite uncaged upon. The receptive field was defined as the % of the dendritic field at which the last synaptic site was detected.

PSD95 Labeling and Imaging

Ethics Statement:
This study was conducted with the approval of the University of Washington Institutional Animal Care and Use Committee (Protocol 4122-01). Mice were euthanized by isoflurane overdose followed by decapitation.

Tissue Preparation:
Mice of postnatal day 22 were euthanized and enucleated and the eyes immersed in oxygenated mouse artificial cerebral spinal fluid (mACSF) containing the following in (mM): 119 NaCl, 2.5 KCl, 2.5 CaCl2, 1.3 MgCl2, 1 NaH2PO4, 11 glucose, and 20 HEPES, and brought to pH 7.42 with NaOH. To obtain retinal whole mounts, retinas were isolated in mACSF and mounted flat, ganglion cell side up, onto filter paper (Millipore).

Biolistic Transfection:
Plasmids for which a cytomegalovirus (CMV) promoter drives expression of tandem dimer Tomato (tdTomato) or postsynaptic density protein 95 fused to yellow fluorescent protein (PSD95-YFP) were coprecipitated onto gold particles (Bio-Rad) (Morgan and Kerschensteiner, 2012). Gold particles were propelled into whole mount retinas using a Helios Gene Gun (Bio-Rad), and the tissue then incubated at ~34°C in oxygenated mACSF in a humidified chamber for 24 hr to allow for expression of PSD95-YFP and tdTomato. We have found that 18-24 hour incubation is sufficient for detection of fluorescent protein expression in peripheral processes (Morgan et al., 2008), and minimizes overexpression of exogeneous PSD95-YFP, which is accompanied by accumulation of fluorescent protein in the nucleus, indicative of overexpression, and is known to alter synaptic dynamics (El-Husseini et al., 2000; Prange et al., 2004). Afterwards, retinas were fixed in 4% paraformaldehyde in mACSF for 20-30 min, rinsed in PBS, and flat mounted in vectashield (Vector Laboratories) for confocal imaging.

Image Acquisition:
Image stacks were acquired on an Olympus FV-1000 laser scanning confocal microscope with an oil-immersion 60x objective (Olympus, 1.35 NA). Voxel dimensions were (x-y-z in μm) 0.103-0.103-0.3 for images of isolated single starburst amacrine cells (SACs) in whole mount retinas. Images were median filtered to remove noise and compressed to 8-bits for analysis after normalization of the entire stack histogram using Fiji(Schindelin et al., 2012).

Quantification of SAC Dendrites:
The branching patterns of SAC dendrites were skeletonized using the filament function of Imaris (Bitplane). Total dendritic length was calculated from the skeletonized filament. A skeleton of an entire SAC traced in Imaris was used to create the schematic in Fig. 3.12.

Identification and Quantification of Postsynaptic PSD95 Puncta:
Potential PSD95YFP puncta were identified using custom MATLAB scripts previously described(Morgan et al., 2008). Briefly, fluorescence signals within the PSD95 channel were iteratively thresholded, filtered by size and contrast, and their ratio of fluorescence to cytosolic fluorescence intensity. We then calculated the log ratio of YFP to tdTomato fluorescence intensity within each punctum in order to evaluate potential bleedthrough between the two channel (Torborg and Feller, 2004). To compare across cells, for each cell, the minimum value for the log ratio for each cell was set to zero (but log ratio distributions were not normalized). A log ratio threshold of 1 was used for simulations and comparison to uncaging and output distributions because it minimized bleedthrough while allowing for a clear designation of PSD95 puncta (see Fig. 3.8 for details). For Figures in which a log ratio threshold is used, only puncta with a log ratio greater than the threshold value were included in analysis.

Path Length and Radial Density Analysis:
We first determined the path length distance from the soma for every node of the skeletonized dendritic filament. The path length distance for each PSD95 puncta was assigned from its nearest node of the skeletonized dendritic filament. We determined the path length puncta linear density by dividing the total number of identified PSD95 puncta by the total dendritic length of the skeletonized dendrite within a sliding window of 10 μms, incrementally by 1 μm, from the soma to the longest path length distance. For radial distributions in Fig. 3.7E and Fig. 3.8C, the number of inputs across cells was summed in 1 μm bins. To exclude the cell body and vertical dendritic segments the initial 15 μm were omitted.

Simulation of SAC

Passive cable simulations of EPSC propagation or EPSP integration within an idealized SAC model were performed using Neuron v7.3 (Carnevale and Hines, 2006). The SAC morphology was approximated as a ball-and-stick model (Fig. 3.9, Fig 3.6, and Fig. 3.10).

To test the effect of dendritic filtering on voltage-clamp recordings, we modeled one 150 μm-long main dendritic branch, each with 3 branch points at 15, 35 and 65 μm (Fig. 3.6). This length was chosen to correspond to the longest SAC dendrites measured (3% of 95 dendrites of SACs patch-loaded with Alexa Fluor 594 and imaged on a two-photon microscope), for which distal events would be the most filtered.

For the integration experiments, we wanted to establish an average dendritic branching representative of SAC morphology (Fig. 3.9, Fig. 3.10). Out of the 95 dendrites of SACs imaged and measured, 66% had 4 or 5 orders of branching, so we implemented those two morphologies in the model. We modeled one 105 µm-long main dendritic branch, with 4 branch points at 10.9, 35.2 and 67.2 and 73.7 µm, and another 115 µm-long main dendritic branch, with 3 branch points at 21.9, 53.6 and 69.1 µm. Synapses were distributed along one of the main branches with regular spacing or as a density gradient that matched experimental findings. The initial 10 µm of the dendrite was set to 400 nm in diameter, which represents the dendritic segment linking the soma in the ganglion cell layer to the dendrites in the inner plexiform layer. The diameter of subsequent dendrites were set at a constant value of 200 nm (Kim et al., 2014). Varicosities were inserted in the most distal third of the dendrites, equally spaced, and modeled as a cylinder of 500 nm length and 500 nm diameter.

Passive properties were assumed uniform across the cell. Specific membrane capacitance (Cm) was set to 1 pF/cm². Rm was set to 21700 Ω-cm² based on an electrophysiological estimate of the membrane time constant (tm = 21.7±2.4ms, n=5 cells, data not shown). tm was measured from the slowest decay time constant of the voltage response to a brief 0.5 ms negative current pulse injection, which produced hyperpolarizations of 30 mV. Ri was set to either 100 Ω-cm or 200 Ω-cm to match a range of values used in modeling studies of SACs and other amacrine cells (Grimes et al., 2010; Singer et al., 2004; Tukker et al., 2004). In all simulations, the resting potential of the cell was set at -70 mV.

All synaptic responses were modeled using the Exp2syn function. The AMPA conductance was set to match the amplitude (313 pS) and time course (trise = 0.14ms, tdecay = 0.54ms) of fast rising miniatures EPSCs (< 0.175 ms rise-time, data not shown), as they are likely to represent synapses converging on proximal dendritic compartments, which are space-clamped. For direction selectivity simulations, however, the value of the synaptic conductance was increased to model the release of three vesicles (939 pS) to account for multivesicular release from bipolar cell terminals (Grimes et al., 2010). We plotted the simulated dendritic voltage at 25, 55, 75, 95 and 105 or 115 µm from the soma, in response to the inward or outward activation of synapses at a speed of 500 µm/s. This speed is within the range of velocity tuning of direction-selective ganglion cells (Sivyer et al., 2010) and matches the speed of visual stimulation from experiments in Figs. 3.11 and 3.14.

Results

The starburst amacrine cell excitatory receptive field is excluded from distal dendrites

A neuron's input distribution relative to its outputs can make a difference in the nature of the dendrite-intrinsic computation the cell can perform. If inputs and outputs are comingled, local dendritic computations would dominate. On the other hand, if inputs are skewed or segregated away from output sites, global computations within each dendrite would dominate (Fig. 3.1A). Modeling studies thus far have assumed inputs are near to output sites (Taylor and Smith, 2012; Tukker et al., 2004), and achieving DS in this case requires strong nonlinear mechanisms.

To determine the functional map of excitatory inputs onto SAC dendrites in the retina, we first measured the excitatory receptive field using visual stimulation of the retina with small spots (25 µm diameter) whose size was chosen to roughly match the receptive field size of cone bipolar cells (Berntson and Taylor, 2000) (Fig 3.1B). We performed voltage clamp recordings

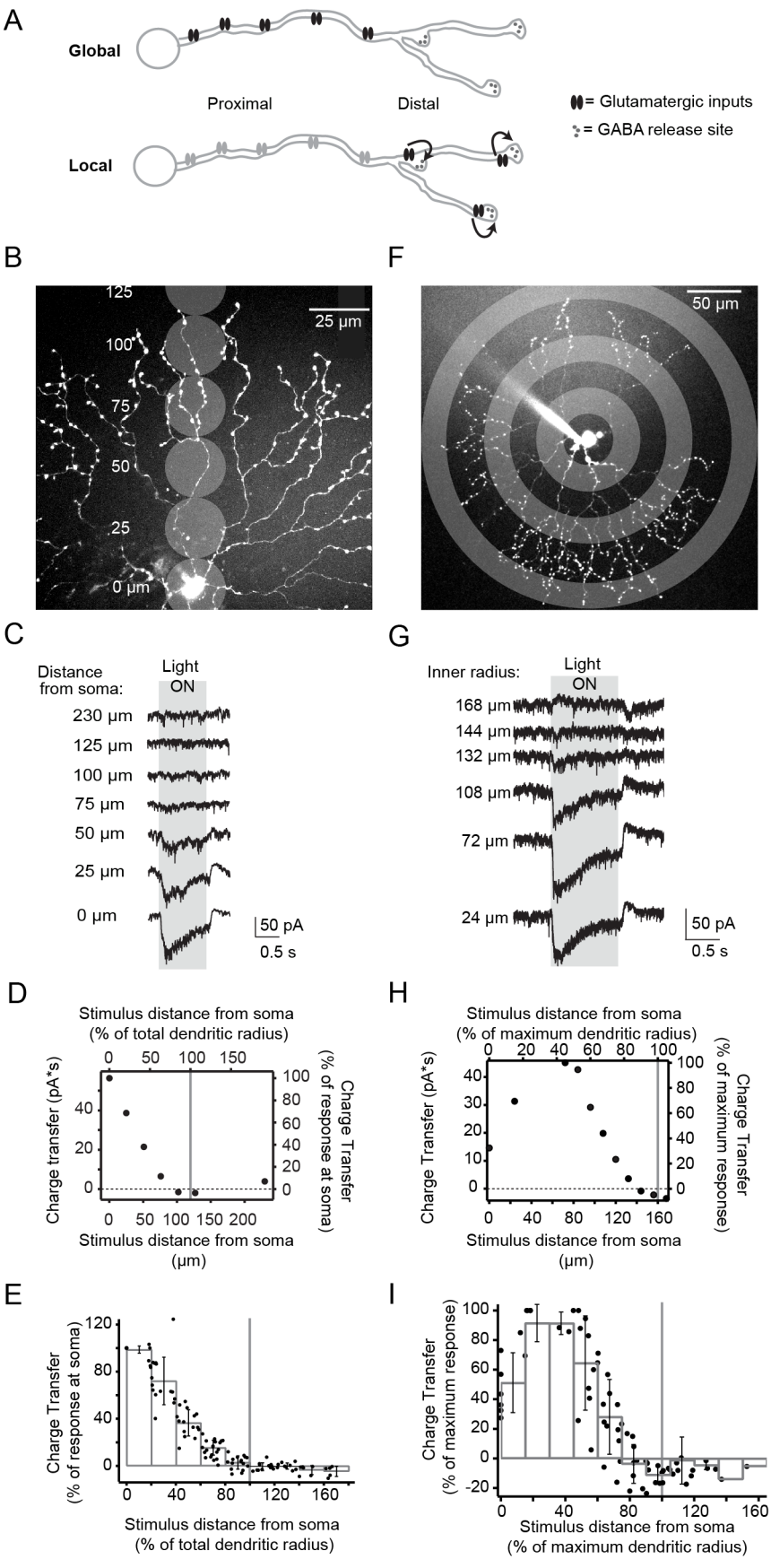
A
Global
Proximal
Distal
Local
= Glutamatergic inputs
= GABA release site
B
125
100
75
50
25
0 µm
25 µm
F
50 µm
C
Distance from soma:
Light ON
230 µm
125 µm
100 µm
75 µm
50 µm
25 µm
0 µm
50 pA
0.5 s
G
Inner radius:
Light ON
168 µm
144 µm
132 µm
108 µm
72 µm
24 µm
50 pA
0.5 s
D
Stimulus distance from soma (% of total dendritic radius)
Charge transfer (pA*s)
Charge Transfer (% of response at soma)
Stimulus distance from soma (µm)
H
Stimulus distance from soma (% of maximum dendritic radius)
Charge Transfer (pA*s)
Charge Transfer (% of maximum response)
Stimulus distance from soma (µm)
E
Charge Transfer (% of response at soma)
Stimulus distance from soma (% of total dendritic radius)
I
Charge Transfer (% of maximum response)
Stimulus distance from soma (% of maximum dendritic radius)

Figure 3.1 **Starburst amacrine cell excitatory receptive field is smaller than dendritic field.** A) Schematic of two distributions of glutamatergic inputs (ovals) and GABAergic release sites (outputs, small circles) on a SAC dendrite. The skewed distribution (top) produces a global computation where all inputs contribute, while the regular distribution produces primarily local computations, with receptors near outputs having a dominant effect on neurotransmitter release (arrows). B) Schematic showing locations of visual stimulation spots overlaid on a 2-photon fluorescence image of a SAC (z-projection). Distances are relative to the soma. C) Light-evoked current responses for illumination locations shown in B (holding potential = -72 mV). Grey box indicates the timing of the stimulus onset and offset. Traces are averages of 4 sweeps. D) Excitatory charge transfer as a function of distance from the soma. Right and top axes are normalized to the maximum charge transfer and maximum dendritic radius, respectively. Grey vertical line: the radius of the dendritic tree. E) Normalized excitatory charge transfer following visual stimulation as a function of distance from the soma (15 cells). Black dots: individual cells; grey bars: binned averages. Grey vertical line: 100% of the radius of the dendritic tree. Error bars = S.D. F) Schematic showing anatomical location of visual stimulation rings overlaid with 2-photon fluorescence projection of a SAC at low magnification. Rings shown have an inner radius of 24, 72, and 132 μm. The thickness of the rings was 24 μm. G) Voltage clamp recordings (holding potential = -72 mV) from the SAC in F during stimulation with stationary rings (width = 24 μm) with different inner radii. Averages of 4 sweeps. Grey box: the timing of the stimulus onset and offset. H) Excitatory charge transfer calculated from the recordings in G plotted as a function of the inner radius from the soma. Right and top axes are normalized to the maximum charge transfer and maximum dendritic radius, respectively. Gray vertical line, the maximum radius of the dendritic tree. I) Excitatory charge transfer calculated for 6 cells plotted as a function of the length of the inner radius from the soma. Axes are normalized to the maximum charge transfer response and maximum dendritic radius, respectively. Black dots: measurements from each cell; grey bars: binned averages of these measurements; error bars: S.D.

from SACs to measure light-evoked excitatory currents (Fig. 3.1C) and quantified the charge transfer as a function of the position of the stimulation spot relative to the dendritic radius. We observed a decrease in charge transfer as spots were presented further from the soma, with spots centered at ≥74±13% of the dendritic radius producing <5% of the maximum charge transfer recorded in the cell (Fig. 3.1D-E, n = 15 cells). On the other hand, we did not observe differences in the spot response kinetics at different locations on the dendritic tree, suggesting that phasic vs. sustained bipolar cell release kinetics may not play a role in generating DS in On-SACs (Fig. 3.2; see Discussion and Kim et al., 2014).

We repeated our receptive field measurements using 24 μm wide ring stimuli to stimulate all of the SAC dendrites at a certain radius on the arbor at once (Fig. 3.1F). Similar to the stimulation with small spots of light, the charge transfer in response to rings decreased to <5% of the maximum response with rings centered at ≥77±10% (average±S.D. for 6 cells) of the maximum dendritic radius (Fig. 3.1I). In addition, during stimulation outside of the dendritic field we observed a decrease in the tonic excitatory current that coincided with an inhibitory current; the inhibitory receptive field extended beyond the excitatory receptive field (Fig. 3.2). Thus, based on ring and spot stimulation, the excitatory receptive field appears to exclude the most distal dendrites.

So far, we have determined the excitatory receptive field using voltage clamp recordings from the soma, but SACs are thought to release neurotransmitter from varicosities in their distal dendrites. To determine the impact of proximal vs. distal visual stimulation at SAC release sites, we performed two-photon imaging of Ca2+ transients from varicosities in SACs filled with OGB-1 (Fig. 3.3A). Consistent with our voltage clamp recordings (Fig. 3.1), we observed larger Ca2+ transients in varicosities in response to spots centered at proximal compared to distal locations, despite the distal spots' closer proximity to the varicosities being imaged (Fig. 3.3B-E). Together, these findings suggest that the excitatory receptive field does not include distal regions of the dendrites, but nevertheless has a strong influence on the Ca2+ concentration there.

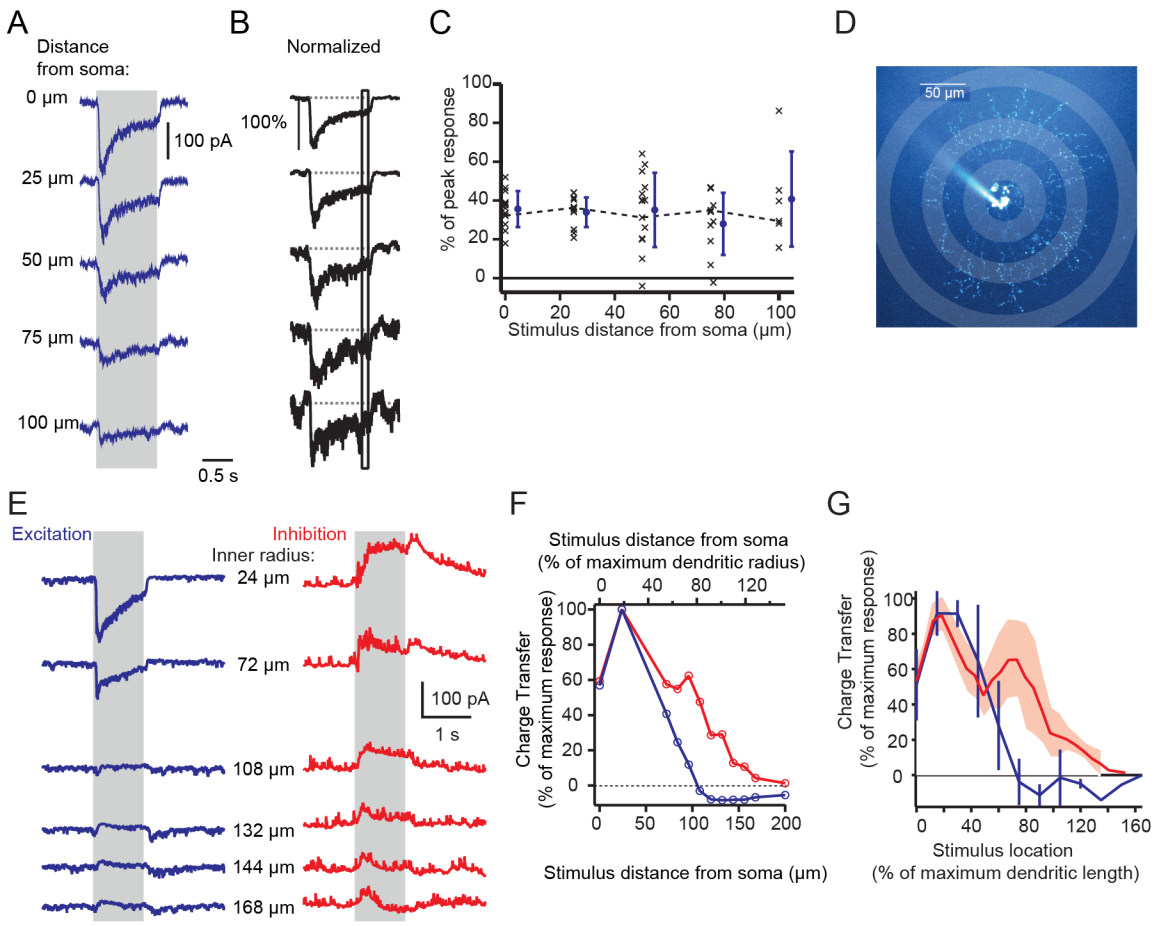

Figure 3.2 **Kinetics of bipolar cell release onto SAC dendrites do not vary based on input location and inhibitory receptive field is larger than dendritic field.** A) Voltage clamp recordings (holding potential = -72 mV) in response to stimulation with 25 µm diameter spots centered at different distances from the soma. Grey box indicates the timing of the light stimulus. Traces are averages of 3 responses. B) The same responses as in A normalized to the maximum amplitude (averaged over 50 ms window) during the first 300 ms of the response. The box indicates the period of time used to assess the sustained component of the response in C. Grey dotted lines mark the baseline. C) Plot showing the amplitude of the sustained component of the response to spots at different distances from the soma as a percentage of the maximum amplitude. Black x's are individual cells, blue dots are averages, error bar = S.D. Dotted line connects responses for the cell in A and B. N = 14 cells. D) Schematic showing anatomical location of visual stimulation rings overlaid with 2-photon fluorescence projection of a SAC at low magnification (20x). Rings shown have an inner radius of 24, 72, and 132 µm. Ring thickness was 24 µm. E) Voltage clamp recordings (holding potentials = -72 mV (blue) and 0 mV (red)) from the SAC in D during stimulation with stationary rings with different inner radii. Traces are averages of 4 sweeps. Grey box indicates the timing of stimulus presentation. F) Excitatory and inhibitory charge transfers calculated from the recordings in E and normalized to the maximum charge transfers plotted as a function of the distance from the inner radius of the ring stimulation to the soma. Blue trace is the excitatory receptive field and red trace is the inhibitory receptive field. Top axis shows ring inner radius distance normalized to the maximum dendritic radius. For this cell, the maximum dendritic radius was 130 µm. G) Excitatory charge transfer calculated for 4 cells plotted as a function of the length of the inner radius of the stimulus from the soma. Axes are normalized to the maximum charge transfer response and maximum dendritic radius, respectively. Blue and red lines are binned averages of the responses from each cell for excitation and inhibition, respectively; error bars/shading are S.D.

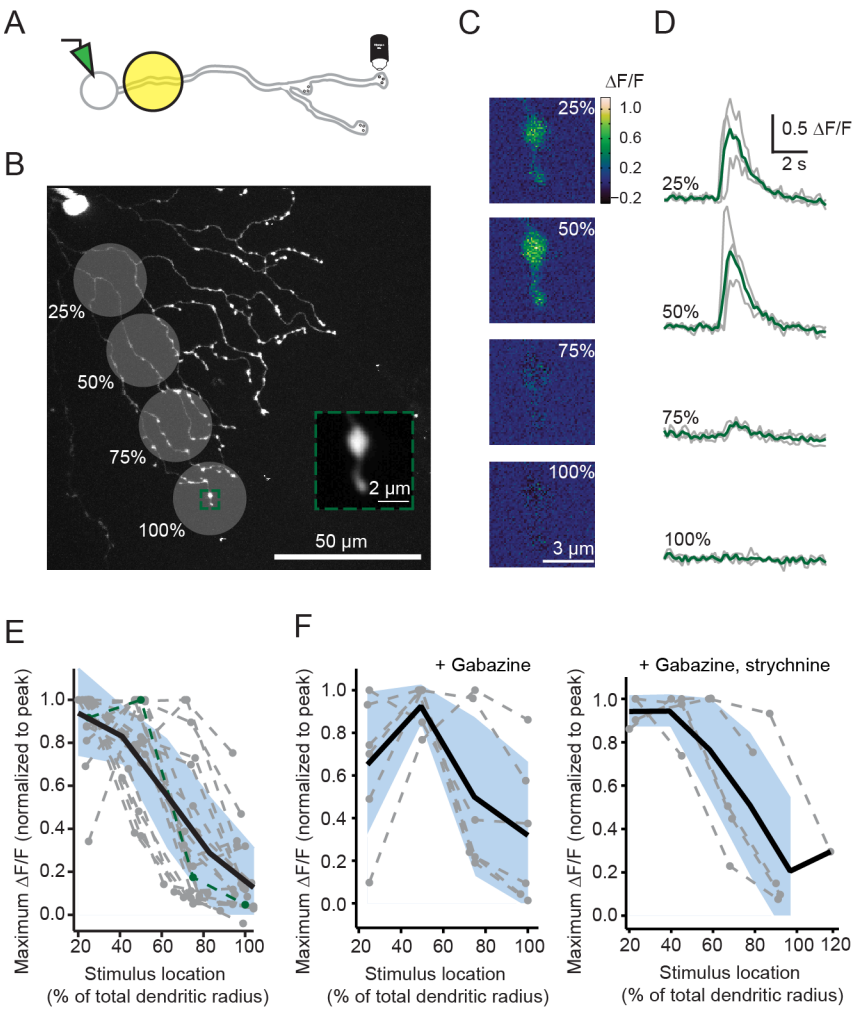

Figure 3.3 **Ca^{2+} transients in varicosities are largest during proximal visual stimulation.** A) Schematic displaying experiment to image a distal varicosity from a SAC filled with 150 µM OGB-1 during visual stimulation with 25 µm diameter spots. B) Location of visual stimulation spots overlaid with a 2-photon fluorescence image of a SAC filled with OGB-1 (z-projection). Visual stimuli were centered at indicated positions (25, 50, 75, 100%) after measuring the SAC dendritic radius along the axis of the varicosity being imaged. Green box: ROI used to image a distal varicosity. The soma and patch electrode are visible in the top left corner. Inset: average intensity projection of the fluorescent images acquired during visual stimulation. C) Maximal change in fluorescence (ΔF/F) responses of the ROI shown in B to one presentation of each spot located at the indicated % of the total dendritic radius along the axis of the varicosity being imaged. D) ΔF/F (grey lines) following visual stimulation centered at the % of the total dendritic radius for the varicosity in B. Green traces: the mean of three trials. E) Maximum ΔF/F normalized to the peak response for 15 varicosities measured from 15 cells in response to stimuli at four locations along their dendrites (grey dotted lines; green line = the cell in B-D). Black line: the average response of linear interpolations of each receptive field. Blue shading = S.D. F) Same as E but for varicosities in the presence of 5 µM gabazine (left; 5 cells) or 5 µM gabazine + 1 µM strychnine (right; 5 cells) to isolate the excitatory inputs.

Glutamate uncaging reveals absence of excitatory synapses in distal dendrites

To directly characterize the distribution of excitatory inputs on SAC dendrites, we used 2-photon fluorescence imaging, glutamate uncaging by single-photon photolysis of MNI-glutamate (2 mM, bath-applied) (DiGregorio et al., 2007), and somatic voltage clamp recordings (Fig. 3.4A-B). Locations along the dendrite where uncaging-evoked EPSCs were detected were assumed to result from the presence of AMPAR clusters (Abrahamsson et al., 2012). We selected uncaging-

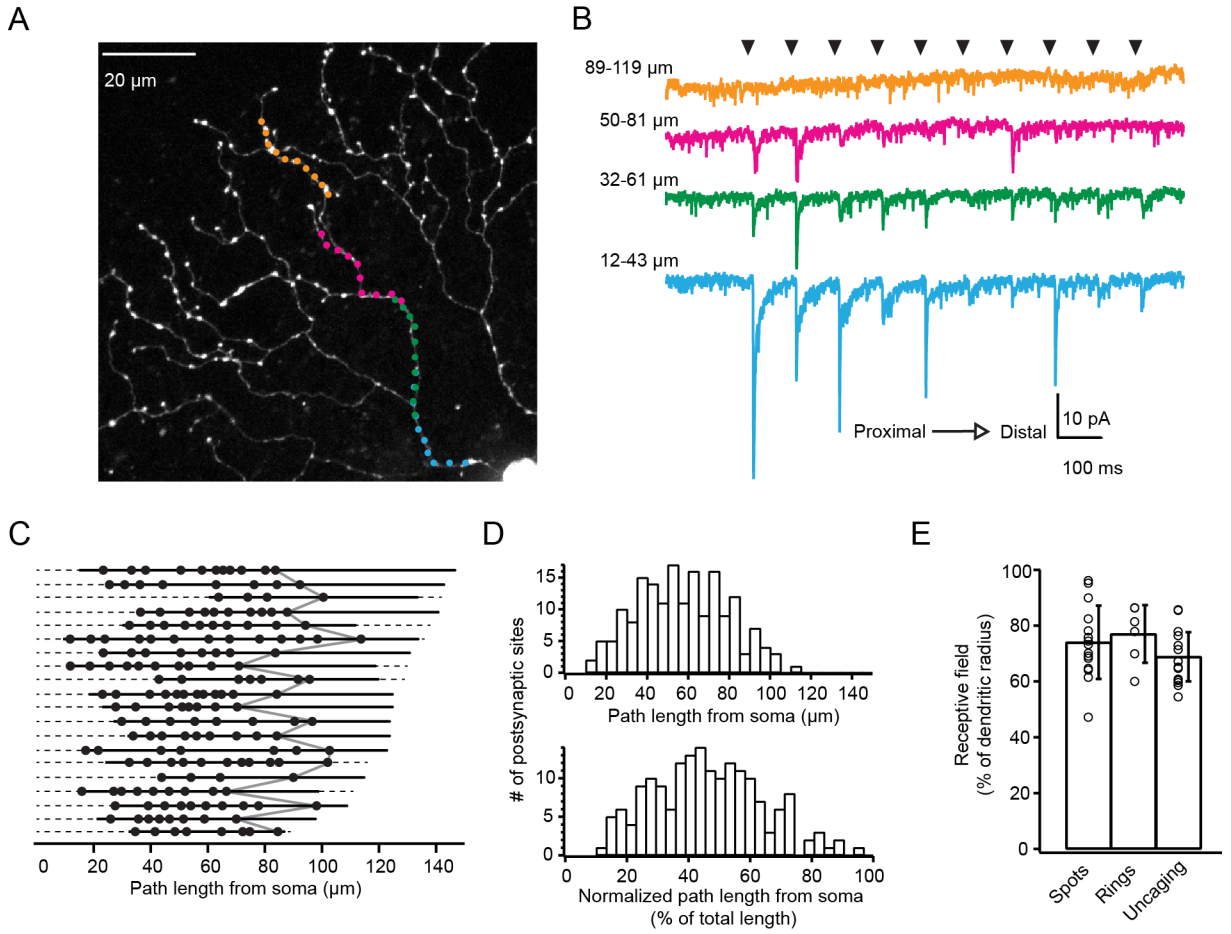

Figure 3.4 **Glutamate receptors are absent from distal dendrites.** A) 2-photon fluorescence image of a SAC (z-projection) with targeted locations of glutamate uncaging sites along one dendritic path. Colors correspond to current responses in B. B) Voltage clamp recordings (holding potential = -72 mV) from the cell in A in response to glutamate uncaging at 40 dendritic sites. Black arrowheads indicate the timing of the 100 µs laser uncaging pulses at different dendritic sites (moving outward from the soma to the distal dendrites from left to right and bottom to top). Traces are averages of 10 sweeps. C) Locations where uncaging-evoked EPSCs indicated the presence of putative postsynaptic sites (black dots). Each row represents a different dendrite (n = 20 dendrites from 15 cells). Dashed lines: the entire path lengths from the soma to the end of the dendrite; solid lines: the path lengths sampled by uncaging. Locations of the last synapses in each dendrite are connected by the grey line. D) Histograms of the putative postsynaptic sites as a function of path length (top) or path length normalized to the dendritic length of each dendrite. E) Starburst amacrine cell excitatory receptive field size determined using spot stimulation ('Spots'), ring stimulation ('Rings'), or glutamate uncaging ('Uncaging'). Error bars are S.D.

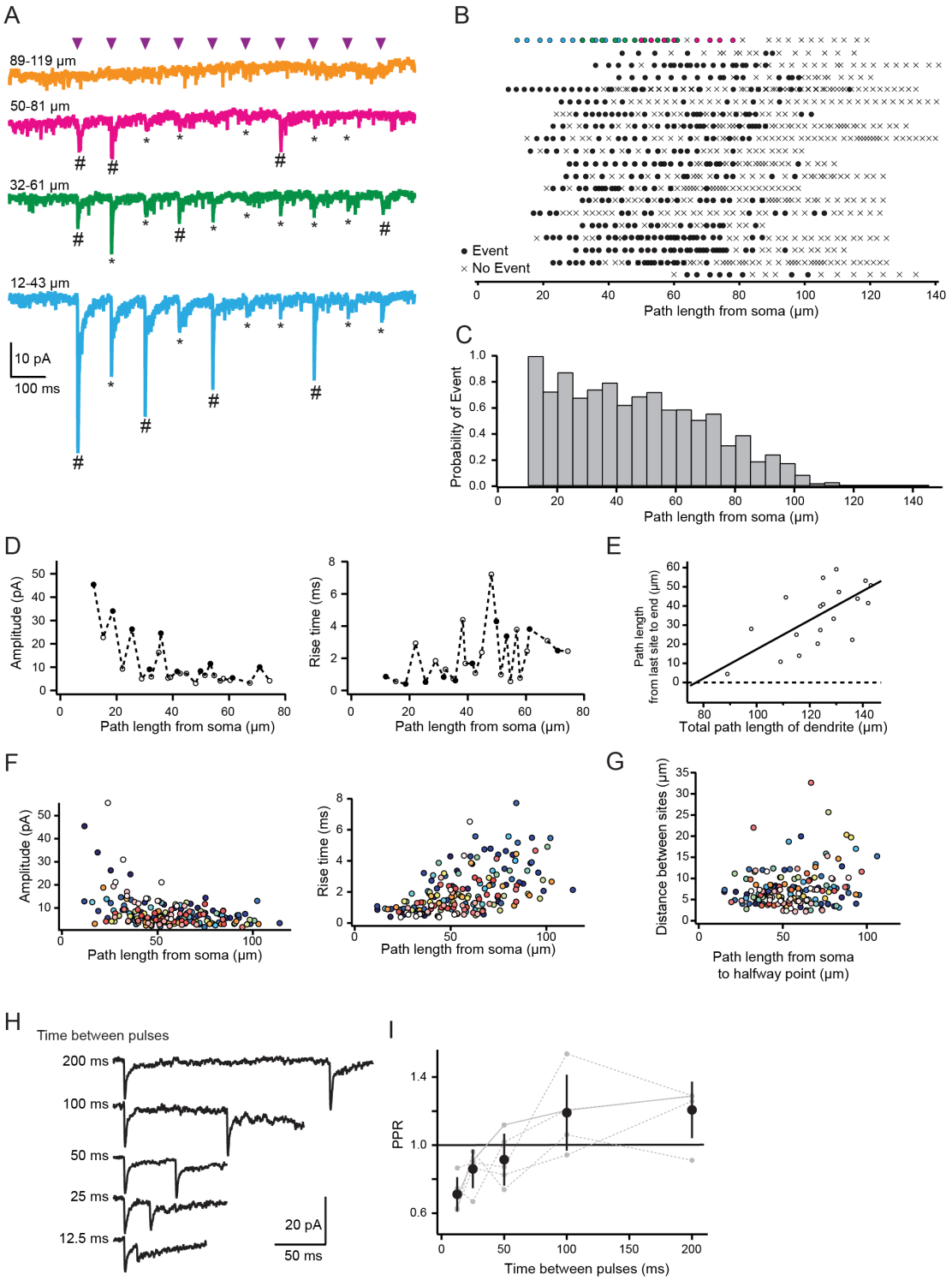

Figure 3.5 **Procedure for determining locations of putative postsynaptic sites using kinetics of uncaging evoked events.** We used event detection combined with selection of uncaging-evoked EPSCs with locally-maximal amplitudes to determine the location of putative postsynaptic sites. A) Same recordings as in Figure 3.4B showing dendritic locations of detected uncaging-evoked events (*) and events further determined to be the sites of putative postsynaptic sites (#). For event detection, uncaging-evoked events were included if the amplitude was greater than 6 times the S.D of the baseline noise, measured during the 3 ms prior to uncaging. This conservative threshold was necessary because of the large amount of spontaneous activity in SACs. To determine putative postsynaptic sites, we

identified locations along the dendrite in which the amplitude of uncaging-evoked currents were maximal relative to its neighbors within 5 µm (local maximum). This strategy minimized double counting, but could also lead to undercounting of putative postsynaptic sites for dendritic segments with high synapse density. B) Dendritic locations of uncaging-evoked events. Each row is a different dendrite (n = 20 dendrites from 15 cells). The top row shows the event locations color-coded to match the traces in A. C) Probability histogram of detecting events from B in 5 µm bins as a function of the path length from the soma. D) Amplitude and rise time of uncaging-evoked events from the cell in A as a function of path length from the soma to the uncaging site. Putative postsynaptic sites were selected from uncaging-evoked events based on the amplitude of the events. Putative postsynaptic sites were defined as locally maximal in amplitude (filled circles) and the other events (open circles) were discarded. For well space-clamped locations proximal to the soma, the location of locally maximal amplitude almost always had locally minimal rise times, confirming the presence of a postsynaptic site. For distal locations, we did not observe the amplitude-rise time correlation, presumably due to dendritic filtering. E) The path length for dendrites in Figure 3.4C from the most distal detected putative postsynaptic site ("last site") to the end of the dendrite plotted as a function of the total path length of the dendrite. The black line is a linear fit with $r^2 = 0.48$. F) Rise time and amplitude of the uncaging-evoked events from putative postsynaptic sites from Figure 3.4C-D plotted as a function of path length from the soma. G) The distance between pairs of adjacent putative postsynaptic sites from Figure 3.4C-D plotted as a function of the path length from the soma to the halfway point between each pair of putative postsynaptic sites, indicating that the density of postsynaptic sites on a given process is constant regardless of distance from the soma. The gradual drop-off in density observed in Figure 3.7D (orange line) is a product of the average across different processes.

To determine the minimum time between uncaging pulses to avoid uncaging when receptors were desensitized, we performed a paired-pulse experiment. We uncaged at the exact same location over a putative postsynaptic site and varied the interval between pulses to measure the desensitization period of the receptors. H) Voltage clamp recordings (holding potential = -72 mV) from a SAC in response to glutamate uncaging at a single dendritic site. The time between pairs of uncaging pulses was varied and is listed to the left of each trace. Traces are averages of 10 sweeps. I) Paired pulse ratio (PPR) as a function of the time between pulses for 5 dendritic sites from 3 cells. Grey lines = individual sites; solid grey line = the cell in H; black spots = the mean PPR across sites; error bars = S.D. For 5 cells, we found a PPR equal to or greater than 1 when the time between uncaging pulses was 100 ms or more. Thus, we used intervals of 100 or 200 ms to map the uncaging responses.

evoked EPSCs with locally-maximal amplitudes as the location of putative postsynaptic sites (Fig. 3.5). In 20 dendrites from 15 cells, the majority of putative synapses were in the more proximal region of the dendritic tree (Fig. 3.4C-D), resulting in an excitatory receptive field that extended to 69±9% of the dendritic field, similar to that determined using visual stimulation (Fig. 3.4E). We confirmed that the lack of responses in distal dendritic regions was not due to alterations in the uncaging resolution or cable filtering (Fig. 3.6), and therefore not due to insensitivity of our measurements. Taken together, these results are consistent with the conclusion that synaptic inputs are absent from the outer third of the SAC dendritic tree.

PSD95 puncta are skewed away from output sites

We next used an anatomical approach to confirm our functional estimates of the distribution of glutamate receptors in SAC dendrites. Retinas were biolistically transfected with plasmids encoding post-synaptic density 95 fused to YFP (PSD95-YFP) to label putative sites of glutamatergic input and tdTomato for identification of transfected SACs (Fig. 3.7A, C). We then took confocal images of SAC dendrites that did not overlap with other labeled cells and identified the locations of PSD95-YFP puncta (Fig. 3.7B; see Methods and Fig. 3.8). We found that PSD95-YFP puncta were at the highest density near the soma, while the density decreased more distally with a profile similar to the putative postsynaptic sites detected with uncaging (Fig. 3.7D, n = 8 cells from 5 retinas).

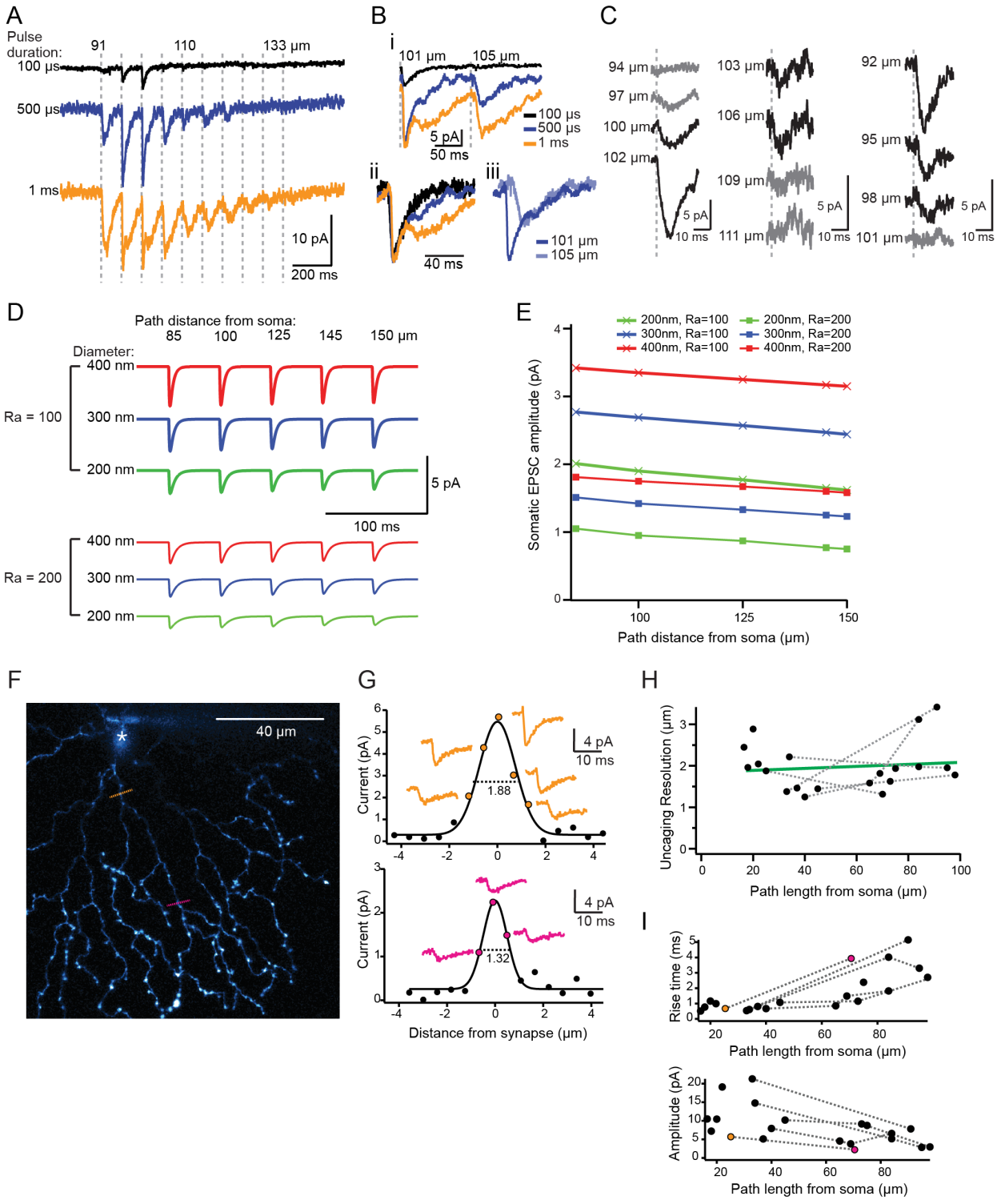
A
Pulse duration:
91
110
133 µm
100 µs
500 µs
1 ms
10 pA
200 ms
B
i
101 µm
105 µm
100 µs
500 µs
1 ms
5 pA
50 ms
ii
iii
40 ms
101 µm
105 µm
C
94 µm
97 µm
100 µm
102 µm
5 pA
10 ms
103 µm
106 µm
109 µm
111 µm
5 pA
10 ms
92 µm
95 µm
98 µm
101 µm
5 pA
10 ms
D
Path distance from soma:
85
100
125
145
150 µm
Diameter:
Ra = 100
400 nm
300 nm
200 nm
5 pA
100 ms
Ra = 200
400 nm
300 nm
200 nm
E
200nm, Ra=100
300nm, Ra=100
400nm, Ra=100
200nm, Ra=200
300nm, Ra=200
400nm, Ra=200
Somatic EPSC amplitude (pA)
Path distance from soma (µm)
F
40 µm
G
Current (pA)
4 pA
10 ms
1.88
1.32
Distance from synapse (µm)
H
Uncaging Resolution (µm)
Path length from soma (µm)
I
Rise time (ms)
Path length from soma (µm)
Amplitude (pA)
Path length from soma (µm)

Figure 3.6 **Glutamate uncaging duration and resolution are sufficient to detect postsynaptic sites in distal dendrites if postsynaptic sites are present.** We wanted to determine whether an absence of uncaging-evoked events in distal sites was due to an absence of receptors or the inability to record these currents from the soma. To test this, we performed two experiments. First, we increased the uncaging laser pulse duration while uncaging over distal dendrites to reveal the presence of AMPARs with a larger dose of glutamate. A) SAC current responses (holding potential = -72 mV) to glutamate uncaging at 10 different dendritic sites (path length from soma indicated above traces) with three different laser pulse durations. The start of laser pulse illumination is indicated by the grey dashed lines. For part A-C, all traces are averages of 10 sweeps. B) i: Expanded timescale of currents evoked at two adjacent dendritic sites from A. ii: Normalized uncaging-evoked currents at 101 µm show that a fast-rising response is detected at all laser pulse durations. iii: Responses to 500 µs uncaging pulse at the two adjacent sites from i overlaid to demonstrate that sites not showing a response at short laser pulse durations never evoke fast-rising events, as would be expected if a prominent number of AMPARs were present at the site of uncaging. Note that because of the close location of the two sites, dendritic filtering also cannot account for the difference (see below for more detail). C) Voltage clamp recordings (holding potential = -72 mV) from three cells in response to glutamate uncaging at very distal dendritic sites (path length from soma indicated to the left of the trace) using a 100 µs uncaging laser pulse demonstrating detection of glutamate receptors. Black traces were events detected using event detection criteria (see Methods), while adjacent grey traces were concluded to have no event.

We found that, while new events emerged when the pulse duration increased (A), these events display the typical kinetics of glutamate spillover (DiGregorio et al., 2007) (B, events recorded at >105 µm from soma), while synaptic sites showed a fast and slow phase typical of on-synapse activation followed by glutamate spillover onto the same synapse (events at <105 µm from the soma). Based on this experiment, we determined that the 100 µs uncaging laser pulse duration was sufficient for detection of distal synapses (C) while optimizing resolution and avoiding spillover.

Second, we examined theoretically whether there could be a decreased chance of detecting distal AMPAR clusters due to dendritic filtering. D) and E) Numerical simulations of somatic EPSCs in a passive neuron under voltage-clamp (with C_m =1 pF/cm^2, R_m = 21700 Ω-cm^2, R_a = 100 Ω-cm or 200 Ω-cm. The amplitude of g_{syn} was set to reproduce experimental miniature EPSCs recorded from SACs (data not shown). Passive properties were assumed uniform across the cell. Pipette resistance was set at 20 MΩ. The idealized SAC dendritic morphology has a uniform diameter of 0.2 -0.4 µm (green, blue, and red traces), 3 dendritic branch points, and a maximum length of 150 µm. D) Traces of simulated EPSCs in response to an evoked conductance (g_{syn}) at input locations at different path distances from the soma. E) The peak amplitude of somatic EPSCs in response to a simulated evoked conductance at different path distances from the soma. This simulation revealed that dendritic filtering, while present at distal sites, does not increase dramatically across the region of dendrite where the most distal synapses were observed, even for diameters as narrow as 0.2 µm. Thus we predict that currents arising from distal synapses should be detectable.

To determine whether the uncaging resolution is affected by the dendritic location of the uncaging site, we uncaged along lines perpendicular to sites previously determined to contain putative postsynaptic sites at different distances from the SAC soma. We determined the effective uncaging resolution by fitting the maximal responses to a Gaussian distribution and measuring the full-width half maximum (FWHM). F) 2-photon fluorescence z-projection of a SAC showing locations of uncaging sites used to determine uncaging resolution (orange and pink lines). White asterisk = location of cell soma. G) Amplitude of uncaging-evoked current as a function of the distance from the putative postsynaptic site to the uncaging site for the cell in F. Colored traces are voltage clamp recordings (holding potential = -72 mV) showing events detected by uncaging (averages of 10 sweeps). Solid black line is the Gaussian fit; the dotted line is the full-width half-max (FWHM) of the fit in microns. H) The uncaging resolution (FWHM of the Gaussian fits determined as in G) as a function of the path length from the soma. The mean uncaging resolution was 2±0.6 µm (n=20 measurements from 11 dendrites in 8 cells). Grey dotted lines connect measurements from different sites on the same dendrite. Green line is a linear fit (slope = 0.002, r^2=0.013). I) Rise time and amplitude of uncaging evoked events from dendritic locations in H plotted as a function of path length from the soma (n=20 measurements from 11 dendrites in 8 cells). Events shown were found to be closest to the peak amplitude of the Gaussian fits used to determine the uncaging resolution; colors correspond to the traces in that figure. Dotted lines connect samples measured from the same dendrite.

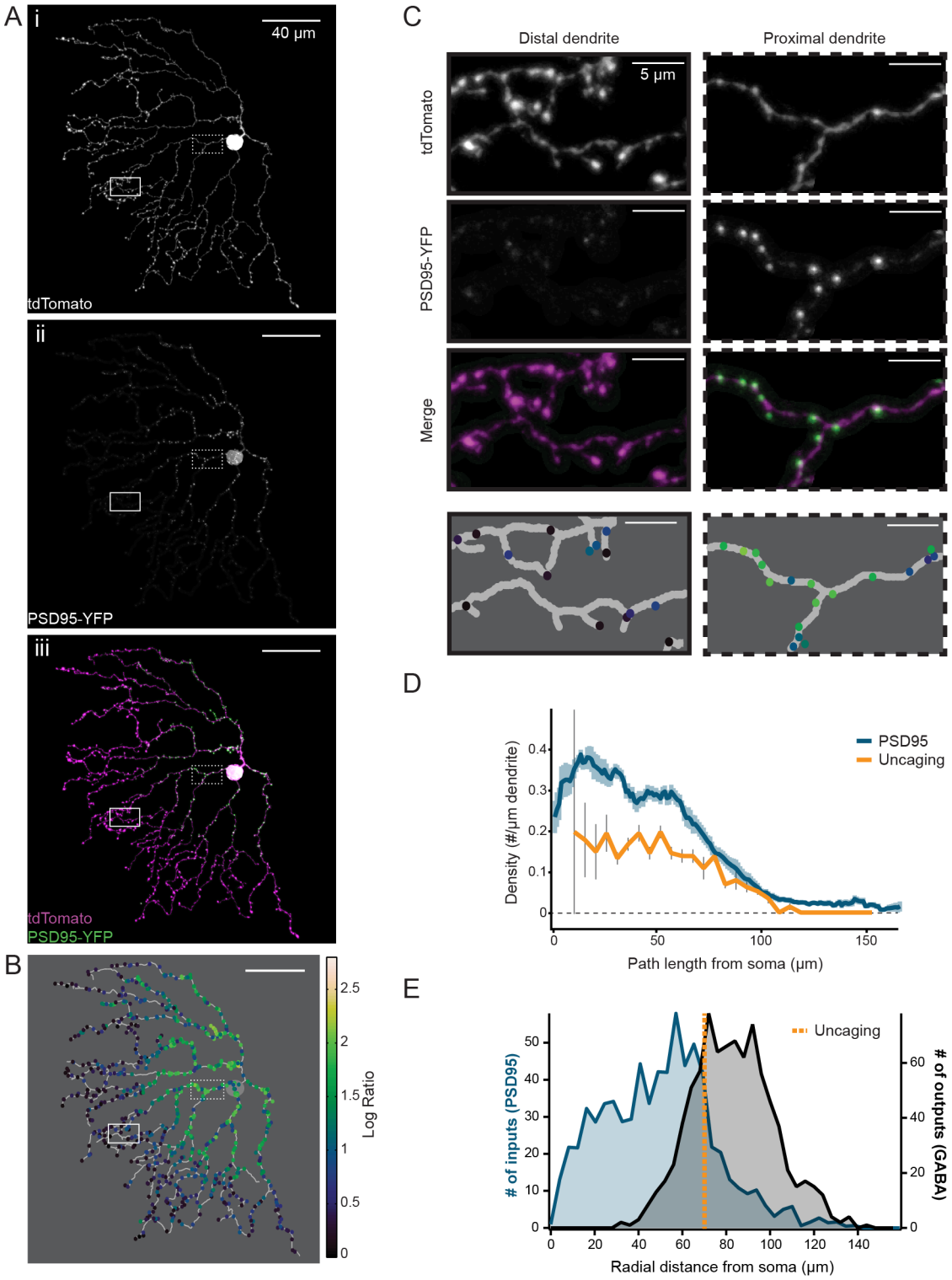
A
i
40 µm
tdTomato
ii
PSD95-YFP
iii
tdTomato
PSD95-YFP
B
2.5
2
1.5
1
0.5
0
Log Ratio
C
Distal dendrite
Proximal dendrite
5 µm
tdTomato
PSD95-YFP
Merge
D
PSD95
Uncaging
Density (#/µm dendrite)
0.4
0.3
0.2
0.1
0
0
50
100
150
Path length from soma (µm)
E
Uncaging
# of inputs (PSD95)
# of outputs (GABA)
50
40
30
20
10
0
60
40
20
0
0
20
40
60
80
100
120
140
Radial distance from soma (µm)

Figure 3.7 **Distribution of putative postsynaptic sites is skewed away from output sites.** A) Projection image of the analyzed dendritic processes of a SAC expressing tdTomato (i) and PSD95-YFP (ii). iii is a merged image showing tdTomato in magenta and PSD95-YFP in green; in this image, contrast was adjusted to improve visibility for display. The image was masked to exclude dendritic branches that overlapped with other labeled cells to ensure that only PSD95 puncta from SACs were included in analysis. Magnified regions (dotted and solid boxes) correspond to example proximal and distal regions in C. B) Skeleton of cell from A with identified PSD95 puncta (colored dots). Colors represent the log ratio of the PSD95 to tdTomato fluorescence intensity within each puncta, which was used for thresholding puncta to include in subsequent analysis (see Methods). C) Examples of distal (left) and proximal (right) regions indicated by the dotted and solid boxes in A. Colors of identified puncta in the bottom row correspond to the heat map in B. D) Density of PSD95-YFP puncta or putative postsynaptic sites determined by uncaging (see Fig. 3E) as a function of dendritic path length from the soma. For PSD95, the average linear density of PSD95 puncta using a 10 μm sliding window is plotted using a threshold log ratio of 1.0 to select puncta to include (blue line; light blue shading = S.E.M, 8 cells). For uncaging, histogram of the average density of putative postsynaptic sites in 5 μm bins is plotted (orange line; grey bars = S.E.M, 23 dendrites). E) Histogram of PSD95 puncta from 8 SACs using a threshold log ratio of 1.0 (left axis, blue) as well as the synaptic contacts with DSGCs (outputs, right axis, black) as a function of radial distance from the soma. Orange dotted line: the mean radial distance of the last putative postsynaptic sites detected with uncaging (see Fig. 3E). Outputs were determined from electron microscopy reconstructions of 24 SACs (Briggman et al., 2011) and analyzed as a function of radial distance to compare with PSD95 locations.

To establish the locations of inputs relative to outputs, we plotted putative postsynaptic locations determined from uncaging or PSD95 labeling and release sites. We took advantage of data from a previous study that used serial block-face electron microscopy (SBEM) to characterize the dendritic locations of On and Off SAC contacts with DSGCs (Briggman et al., 2011). We found that synaptic input and output distributions were significantly skewed away from one another (Fig. 3.7E; $p<0.05$, Wilcoxon Rank test). Similarly, only 25% of the output sites overlapped with the excitatory receptive field predicted from uncaging (Fig. 3.7E, orange dotted line is the mean radial distance of the last postsynaptic site predicted from uncaging). This arrangement of inputs and outputs suggests that computations in the SAC most likely rely on a global mechanism of dendritic integration (Fig. 3.1A), and may underlie a dendrite-intrinsic DS computation.

Skewed synaptic input distributions enhance DS of simulated dendritic voltage

How does the skewed distribution of inputs contribute to direction selectivity of SAC outputs? To address this question, we turned to a computer simulation based on a passive "ball and stick" representation of the SAC dendrite (Fig. 3.9A, D and Fig. 3.10). The dendritic morphology was based on the average lengths of dendritic branches measured from SACs imaged by 2-photon microscopy (data not shown). We compared the dendritic voltage responses produced by several different input distributions: the skewed distribution determined by uncaging (Fig. 3.9A), the higher density skewed distribution determined by PSD95 labeling (Fig. 3.10A), a regular distribution covering the entire dendritic length (Fig. 3.9D, Fig. 3.10D), and a regular distribution covering the proximal 71% of the dendritic length, which is the extent of the excitatory receptive field predicted from uncaging (calculated from Fig. 3.4C). These different distributions allowed us to assess separately the impact of skewed synapse distributions and the effect of the absence of any inputs to the distal region of the SAC.

We simulated voltage along the dendrite during outward and inward stimulation of inputs at an apparent velocity of 500 μm/s and report the results both at specific sites (Fig. 3.9B, E) as well as continuously along the entire dendrite (Fig. 3.9C, F). To quantify the strength of DS, we computed the difference in peak depolarization between outward and inward stimulation (Fig.

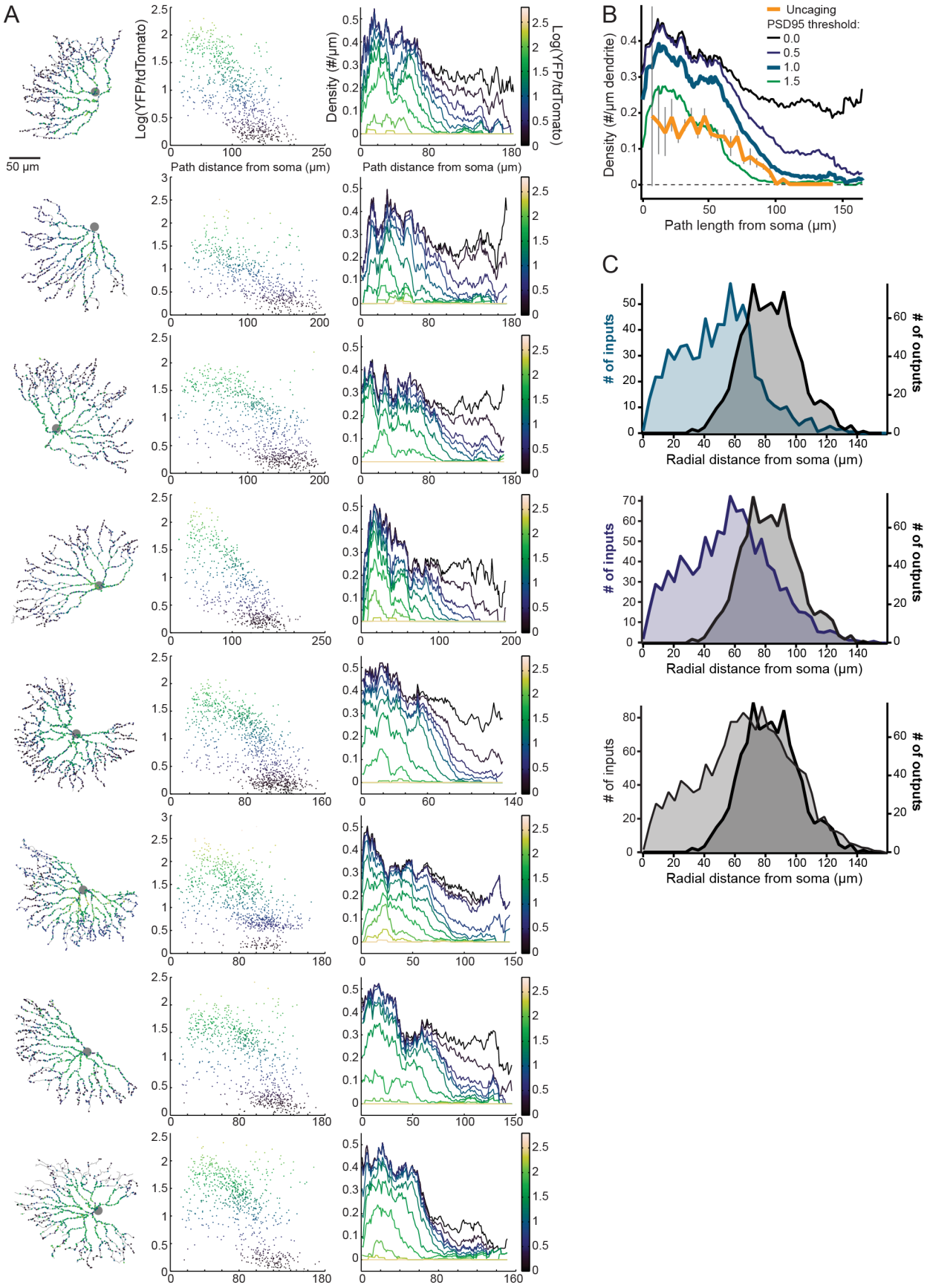
A
50 µm
Log(YFP/tdTomato)
Path distance from soma (µm)
Density (#/µm)
Path distance from soma (µm)
Log(YFP/tdTomato)
B
Uncaging
PSD95 threshold:
0.0
0.5
1.0
1.5
Density (#/µm dendrite)
Path length from soma (µm)
C
# of inputs
# of outputs
Radial distance from soma (µm)
# of inputs
# of outputs
Radial distance from soma (µm)
# of inputs
# of outputs
Radial distance from soma (µm)

Figure 3.8 **Effect of threshold on puncta detected from eight SACs labeled with PSD95-YFP.** To identify PSD95 puncta, we computed the log ratio of the intensity of YFP fluorescence to tdTomato fluorescence for each pixel, $R=\log(F_{YFP}/F_{tdTomato})$. Variations in R are independent of imaging conditions that linearly scale the ratio of F_{YFP} to $F_{tdTomato}$ and help to normalize for bleed-through from the tdTomato channel into the YFP channel, which is more substantial in distal dendrites (see example images in Fig. 3.7C). PSD95 puncta were subsequently identified using a segmentation algorithm that detected spatial variations of R. We systematically varied the threshold value of R to determine the effect of this value on the distribution of puncta as a function of distance along the dendrite. Across all cells, a threshold of R=1 represented a transition—a range of higher thresholds did not vary the distributions substantially while lower thresholds greatly increased the number of distal puncta. In addition, values of R<1 corresponded to F_{YFP} that was indistinguishable from $F_{tdTomato}$ bleedthrough (see example in Fig. 3.7A,C).
A) First column: Skeleton analyzed dendritic arbors of all 8 cells with identified PSD95 puncta used for analysis (colored dots). Colors represent $R = \log(F_{YFP}/F_{tdTomato})$ within each punctum, which was used for thresholding puncta to include in subsequent analysis. Second column: For each cell, the R value within each punctum (dots) is plotted as a function of path distance from the soma. Third column: For each cell, the average linear density of PSD95 puncta as a function of path length from the soma is plotted using increasing thresholds of R to determine puncta to include in analysis. All colors correspond to the colormap on the right. B) This plot is the same as the plot in Figure 3.7D with the addition of three density lines showing additional threshold log ratios (green = 1.5; indigo = 0.5; black = 0.0), which demonstrate the average linear density of PSD95 puncta as a function of path length from the soma in 8 cells. C) Histogram of PSD95 puncta (left axis) from 8 cells using a threshold log ratio of 1.0 (top; same as Fig. 3.7E displayed for comparison), 0.5 (middle), or 0.0 (bottom), as well as the synaptic contacts with DSGCs (right axis, black), as a function of radial distance from the soma. Radial distances of synaptic contacts with DSGCs were measured from electron microscopy reconstructions of 24 SACs (Briggman et al., 2011).

3.9H, J). There were three primary predictions from the model. First, we found that input distributions restricted to the proximal 71% of the dendrite (whether skewed distributions or regular distributions) produced the strongest DS for outward motion. Second, input distributions restricted to the proximal 71% of the dendrites also led to lower DS values for varicosities located within the receptive field of the SAC dendrite compared to varicosities located outside the receptive field. Third, the degree of DS was constant over a long section at the end of the dendrite (>30 μm for the uncaging distribution; >45 μm for the PSD95 distribution) only for input distributions restricted to the proximal 71% of the dendrites. The uniform depolarization along the distal dendrite is the result of inputs localized to the proximal portion of the dendritic tree acting in combination with the sealed cable effect of the dendrite (see Discussion). In contrast, stimulating a regular synapse distribution covering the whole dendrite produced DS values that became steadily stronger with increasing distance from the soma, although DS remained much weaker than for input distributions restricted to the proximal 71%, even at the most distal sites (Fig. 3.9G-J). These results were consistent at a faster velocity of stimulation (1000 μm/s, data not shown). Our passive model simulations suggest that a proximal-weighted input distribution promotes a prominent direction selective depolarization in the distal dendritic tips, where the majority of release sites are located.

Direction selectivity of varicosities depends on varicosity location

Our simulations predict that varicosities in the distal region of the dendrite will have similar strength DS, in contrast to weaker DS at more proximal release sites (Fig. 3.9). To test this prediction directly, we performed 2-photon Ca2+ imaging of varicosities in SACs while stimulating the retina with moving squares of light (25 μm2). Note, there are two important differences from previous measurements that used Ca2+ imaging to assess DS in SAC dendrites (Euler et al., 2002; Hausselt et al., 2007; Lee and Zhou, 2006; Yonehara et al., 2013). First, we

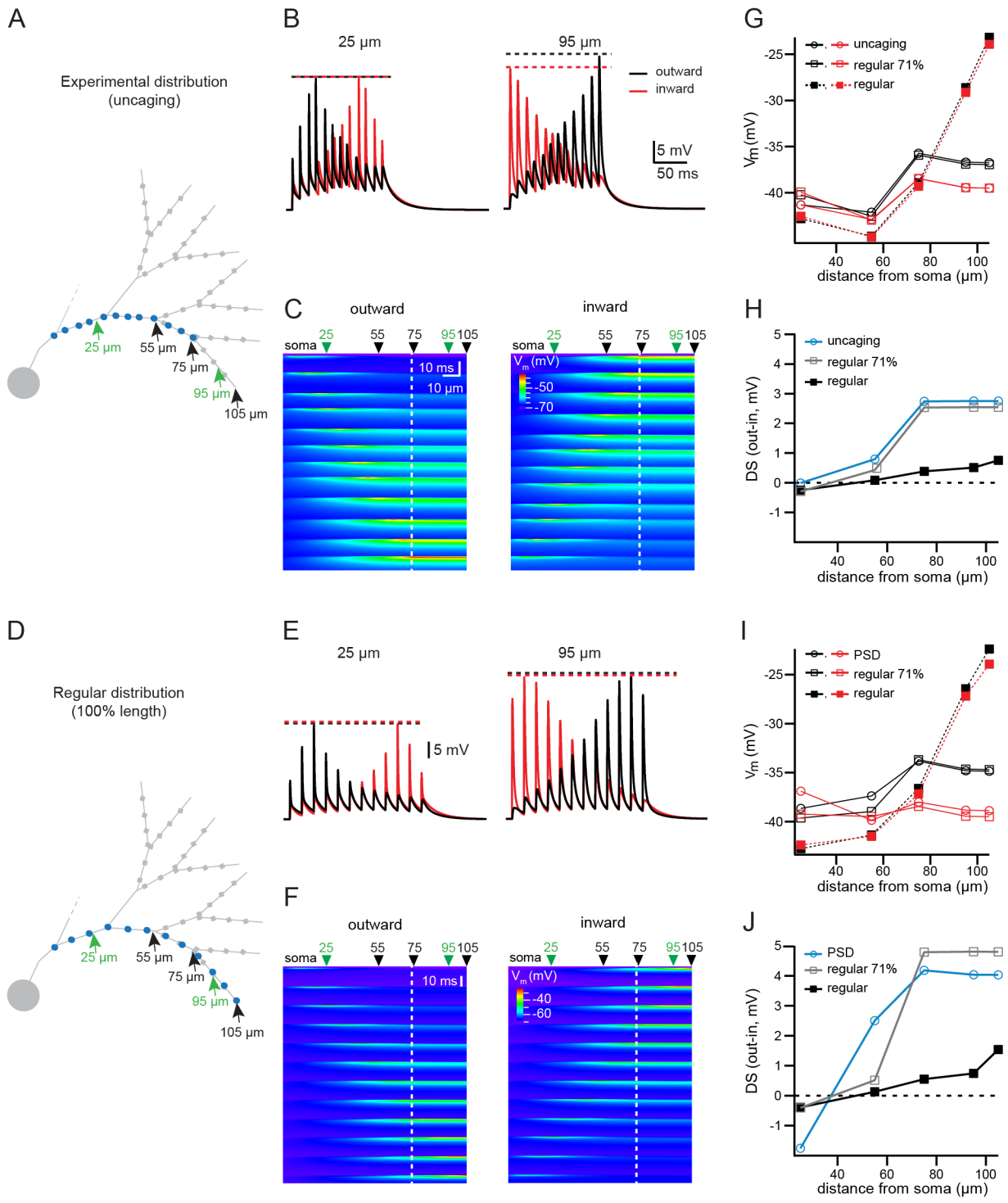

Figure 3.9 **Synaptic input distribution supports DS of simulated dendritic voltage.** A) Ball-and-stick representation of a partial SAC dendritic tree used for simulations of dendritic integration in a passive model. Blue circles, the location of synapses used in simulations, corresponding to the average distance from the soma of putative synapses determined from uncaging. Green arrows: locations where the dendritic voltage is plotted in B; black arrows: locations where the peak of the dendritic voltage is plotted in the summary in G-H. Grey squares: wider compartments of the distal dendrite representing varicosities. B) Simulated dendritic voltage at two locations (indicated by green arrows in A), in response to the outward (black traces) or inward (red traces) activation of the

synapses displayed in A at a speed of 500 µm/s. Dotted lines: amplitude of the peak of the synaptic response in each condition. C) Heat map of simulated dendritic voltage measured along the entire dendritic branch containing the activated synapses (x-axis) for the duration of the stimulus (y-axis). The color scale depicts the amplitude of the depolarization. *Left plot*: response to outward stimulation. *Right plot*: response to inward stimulation. At the peak of the activation of each synapse, the local voltage propagates with little electrotonic attenuation to the dendritic tip due to the end effect of the electrical cable. Green arrows: the two positions along the dendrite corresponding to the traces in B (25 and 95 µm from the soma); black arrows: locations where the peak of the dendritic voltage is plotted in the summary in G-H. The white dotted line indicates the location of the most distal synapse. D) Same as A, but blue circles indicate the location of regularly distributed synapses, the most distal synapse being located at the tip of the dendrite. For the regular distributions, the average density is the same as the experimental distribution determined with uncaging (0.09/µm). E) Same as B, for the gradient of regular synapses stopping at 100% of the dendritic length (displayed in D). F) Same as C, for the gradient of regular synapses stopping at 100% of the dendritic length (displayed in D). G) Plot of the maximum simulated dendritic voltage during inward (red) or outward (black) activation of synapses, measured at several dendritic locations, for the experimental distribution of synapses (circles, solid lines), a distribution of regularly spaced synapses with the most distal synapse located at 71% of the length of the dendrite as in the experimental distribution (open squares, solid lines), and the regular distribution stopping at the tip of the dendrite (closed squares, dotted lines). H) Summary plot showing the DS (defined as the difference of the peak dendritic voltage measured during outward and inward activation of inputs) at various dendritic locations for the different synaptic distributions (experimental distribution of synapses, circles, light blue; regularly spaced synapses with the most distal synapse located at 71% of the dendritic length, open squares, grey; regular distribution stopping at the tip of the dendrite, closed squared, black). I) Same as G, using synapse gradients determined from the average locations of PSD95 labeling (see Fig. 3.10). The regular distributions in this plot have the same average synaptic density as the experimental distribution from PSD95 labeling (0.2/µm). J) Same as H, using synapse gradients determined from the average locations of putative PSDs.

stimulated the retina with small moving squares, rather than circular gratings or stimuli larger than the size of the SAC dendritic field, to observe single motion-evoked events and isolate the contribution from a single dendrite. Second, we restricted the moving square to 75% of the dendritic radius to optimally stimulate the excitatory receptive field (Fig. 3.11A).

Similar to previous studies, we observed distal varicosities that responded with Ca2+ transients that were larger for outward compared to inward motion (Fig. 3.11B, C) and a large variance in the DS across varicosities (Euler et al., 2002; Hausselt et al., 2007; Lee and Zhou, 2006; Yonehara et al., 2013) (Fig. 3.11F-G). We believe this variance to be due to the complex dendritic structure being stimulated (Fig. 3.12) or to off-axis tuning of varicosities, as described previously (Euler et al., 2002; Yonehara et al., 2013).

Next, we examined how the DS of a varicosity related to its location along the SAC dendrite. Because our model predicts strong DS of varicosities over the last ~30% of the SAC dendrite, we split the imaged varicosities into two groups using the average path length to the last synapse predicted from uncaging (71% of the dendritic path from the soma, calculated from Fig. 3.4C). We found that varicosities located distal to the last synapse predicted from uncaging (examples in Fig. 3.11B, C) were significantly more direction selective than varicosities located within the region where synapses were detected (examples in Fig. 3.11D, E, summary in Fig. 3.11F, G; mean DSI = 0.34±0.23 for 25 varicosities outside receptive field and 0.11±0.18 for 8 varicosities inside receptive field; Student's t-test: $p<0.05$). These results demonstrate that the DSI of varicosity Ca2+ transients depends on location in a manner consistent with the voltage responses predicted by a purely passive dendrite model.

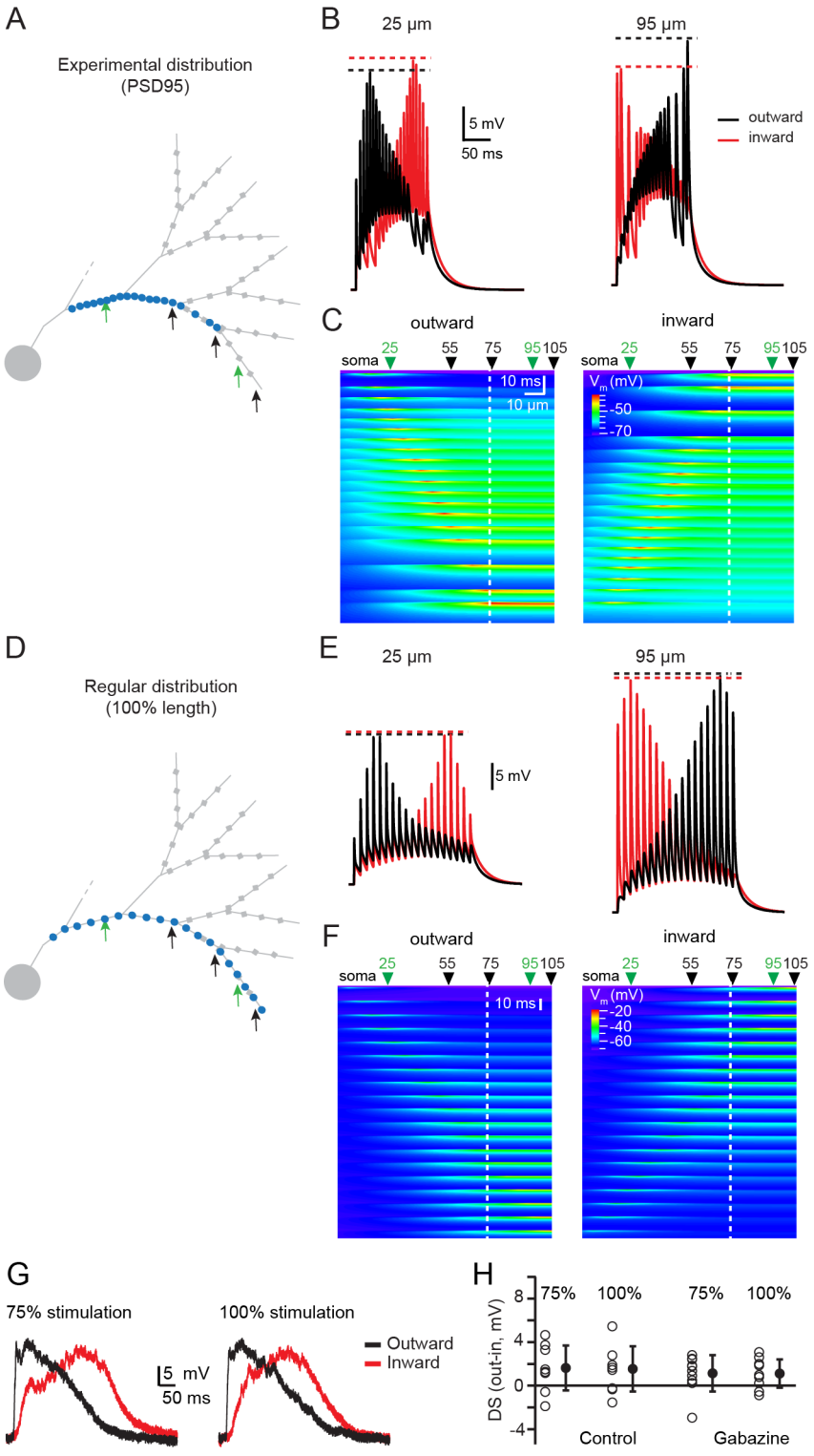

Figure 3.10 **Synaptic input distribution supports direction selectivity of simulated dendritic voltage (PSD95 gradient).** A) Ball-and-stick model of a partial SAC dendritic tree used for numerical simulations of dendritic integration. Blue circles indicate the location of synapses based on the distribution determined with PSD95 labeling (Fig. 3.7). Green arrows indicate locations where the dendritic voltage is measured. B) Dendritic voltage at two of the locations indicated by the green arrows in A, in response to the outward (black traces) or inward (red traces)

activation of the synapses displayed in A at a speed of 500 μm/s. Dotted lines indicate the amplitude of the peak of the synaptic response in each condition. C) Heat map of dendritic voltage measured along the entire dendritic branch (x-axis) for the duration of the stimulus (y-axis) during which synapses, placed according to the average location of putative synapses determined from PSD95 labeling, are activated. The color scale depicts the amplitude of the depolarization. The left plot represents the response to outward stimulation, and the right plot the response to inward stimulation. At the peak of the activation of each synapse, the local voltage propagates with little electrotonic attenuation to the dendritic tip due to the end effect of the electrical cable. The green arrows above the plot indicate the two positions along the dendrite corresponding to the traces in B (25 and 95 μm from the soma), and the black arrows indicate the other locations where peak dendritic voltage is plotted on the summary plot (Fig. 3.9I-J). D) Same as A, but blue circles indicate the location of regularly distributed synapses with the same average density as in A, the most distal synapse being located at the tip of the dendrite. E) Same as B, but for the regular distribution of synapses extending to the tip of the dendrite, as displayed in D. F) Same as C, but for the regular distribution of synapses extending to the tip of the dendrite, as displayed in D. G) Somatic current clamp recordings from SACs during stimulation with moving squares presented over 75% (left) or 100% (right) of the dendritic radius. Responses to motion outward from the soma to the distal dendrites (black) and inward from the distal dendrites to the soma (red) are shown. H) DS of the peak somatic voltage measured in current clamp during visual stimulation with moving squares traversing 75% or 100% of the dendritic radius. Data are from 9 cells in control conditions and 10 cells in the presence of 5 μM gabazine. Note the similarity between these recordings and the simulations of the voltage at 25 μm from the soma in B. Also note that the results shown in G and H here suggest that the SAC is not a passive cell, but rather has active conductances that alter the direction preference recorded at the soma.

Excitatory and inhibitory inputs cooperate to enhance direction selectivity

While we have demonstrated that the excitatory input distribution can enable a dendrite-intrinsic computation of motion direction, some studies have proposed that lateral inhibition from other SACs is the origin of DS in SAC dendrites (Lee and Zhou, 2006; Münch and Werblin, 2006). Note, lateral inhibition between SACs in adult mice is mostly provided by SAC processes oriented in antiparallel directions (Fig. 3.13, Kostadinov and Sanes, 2015; Lee and Zhou, 2006). Given this geometry, inward light stimulation for the SAC being recorded would correspond to outward motion for neighboring presynaptic SACs (Fig. 3.13). Hence, the dendrite-intrinsic computation described above would maximally drive GABA release from the neighboring SAC onto the SAC being recorded, enabling lateral inhibition, which we predict will enhance DS by suppressing responses to inward light stimulation.

To test this model, we conducted two manipulations. First we compared DS in distal varicosities in response to motion stimuli that ended at 75% of the dendritic radius (as in Fig. 3.11) to those that ended at 100% of the dendritic radius, which is likely to induce a more robust activation of inhibitory inputs because the stimulus travels over a larger portion of the neighboring SACs' dendrites (Fig. 3.13). Indeed, we observed larger DSIs in response to 100% stimulation compared to 75% stimulation (Fig. 3.14B, E; paired t-test: $p<0.05$ [Bonferroni corrected], n=22 varicosities). This difference is due primarily to a reduction in Ca2+ transients evoked by 100% inward stimulation (Fig. 3.14D).

Second, we repeated these experiments in the GABAA receptor antagonist, gabazine (5 μM). Though there was an overall reduction in DSI across varicosities (Fig. 3.14E; repeated measures ANOVA: $p<0.05$ for control vs. gabazine groups), the majority of varicosities still exhibited larger responses to outward motion compared to inward motion (e.g. Fig. 3.14C). The weakened DSI in the absence of GABAergic inhibition is primarily attributable to an increase in the response to inward motion (Fig. 3.14D), suggesting that in control conditions inhibition is more pronounced during inward stimulation. Notably, in the absence of GABAergic network interactions, the enhanced DS observed for 100% stimulation over 75% was eliminated (Fig.

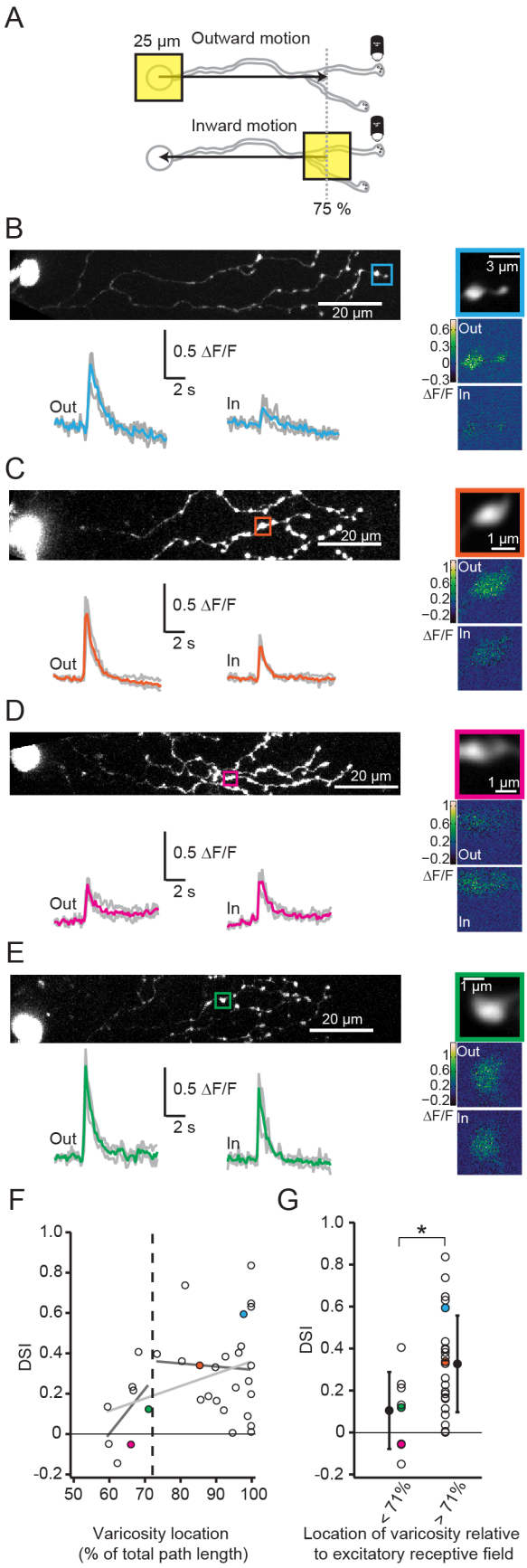

Figure 3.11 **Direction selectivity of varicosities depends on varicosity location** A) Schematic showing imaging of a distal varicosity from an OGB-1-filled SAC presented with a 25 µm square of light moving either outward from the soma toward the distal dendrites or inward from the distal dendrites toward the soma. The stimulus was restricted to 75% of the dendritic radius (grey dotted line). B-E) Four examples of Ca^{2+} responses to stimulation with moving squares. B is an example of an outward-preferring varicosity near the end of the dendrite. C is an example of a more proximal varicosity that is strongly direction selective for outward motion. D is an example of a slightly inward-preferring varicosity. E is an example of an untuned varicosity. *Top left*: 2-photon fluorescence image of SAC filled with OGB-1 (z-projection). The square indicates the imaged varicosity. The soma is on the left. *Top right*: Average intensity projection of the imaged varicosity during the entire experiment. *Bottom left*: ΔF/F (grey) following visual stimulation with a 25 µm moving square either outward from the soma toward the end of the dendrites ("out") or inward from the distal dendrites toward the soma ("in"). Colored traces: averages of the three trials. *Bottom right*: Maximal ΔF/F responses of the imaged varicosities to a single presentation of the moving square moving outward ("out") or inward ("in") along the dendritic radius. F) Direction selective index (DSI) for varicosities from 33 cells in response to inward vs. outward moving squares (black circles) as a function of the varicosity location normalized to the path length of the dendrite. A positive value for the DSI indicates a larger response for outward motion compared to inward motion. Colored dots are the DSIs for the example cells in B-E. Black dotted line: average length of the excitatory receptive field predicted from uncaging (see Fig. 3.4). Light grey line is a linear fit to the entire data set (slope = 0.006, r2 = 0.134) while dark grey lines are fits to the varicosities inside vs. outside of the receptive field detected from uncaging (inside: slope = 0.022, r2=0.248; outside: slope = -0.002, r2 = 0.002). G) DSI for varicosities from 33 cells (black circles) sorted by whether they are within (< 71%; 8 cells) or outside (> 71%; 25 cells) of the mean excitatory receptive field predicted from uncaging (black dotted line in F). Colored dots are the DSIs for the example cells in B-E. Open circles = means ;error bars = S.D. * = $p < 0.05$, Student's t-test.

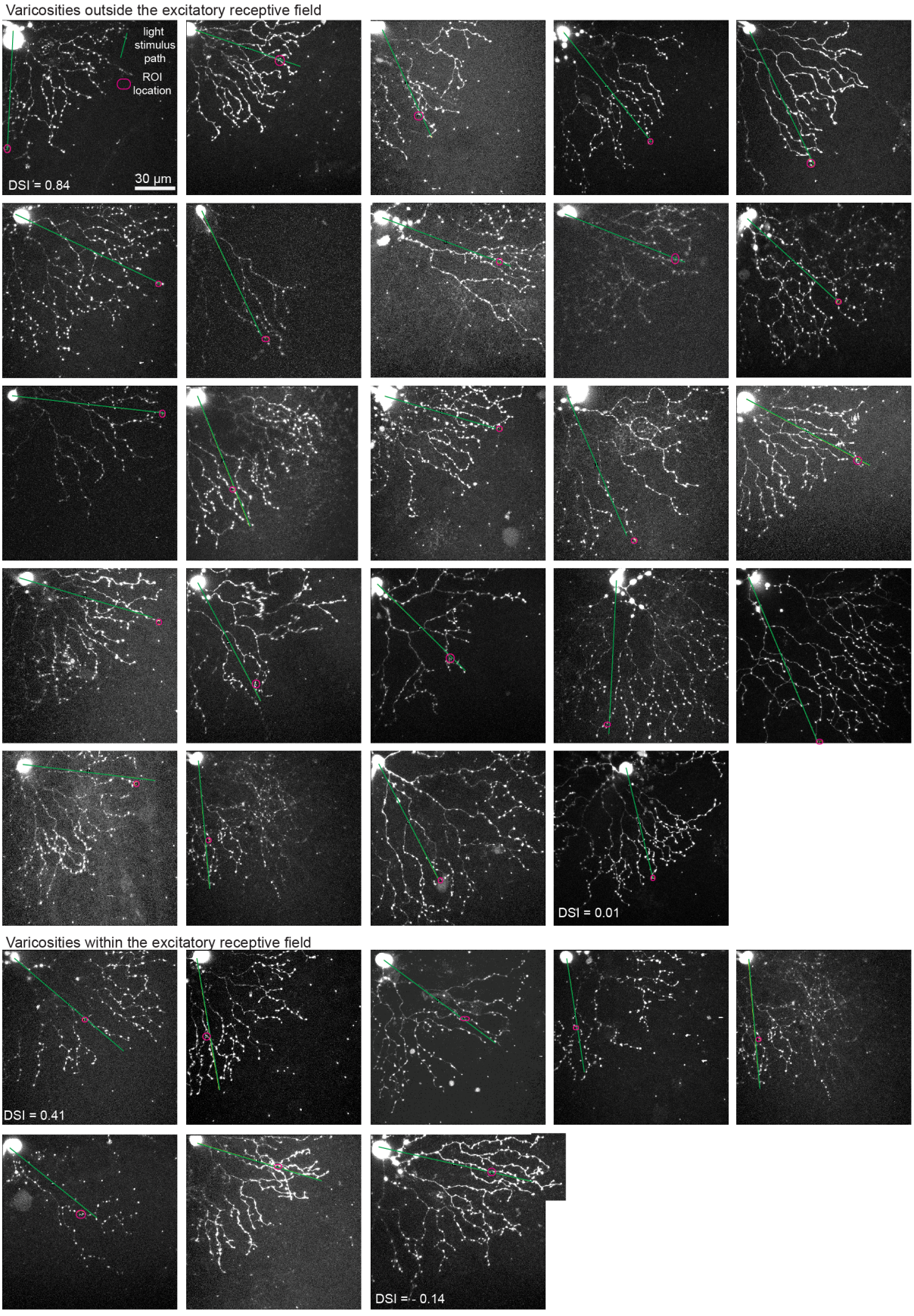
Varicosities outside the excitatory receptive field
light stimulus path
ROI location
DSI = 0.84
30 µm
DSI = 0.01
Varicosities within the excitatory receptive field
DSI = 0.41
DSI = 0.14

Figure 3.12 **Locations of visual stimulation and imaged varicosities.** Maximum intensity z-projections of 2-photon images of SACs filled with OGB-1 with the laser tuned to 800 nm. Images were acquired after measuring Ca^{2+} transients in the varicosities indicated (magenta circles) in response to visual stimulation (see Fig. 3.11). Squares of light (25 μm) were projected on the retina along either 75 or 100% (Fig. 3.14) of the path indicated in green. The exact extent of stimulation relative to the SAC arbor was determined post-hoc from these images and corrected if necessary (e.g. image in row 2, column 3). Images are divided into two groups: SACs for which the imaged varicosity was located outside of the SAC's predicted excitatory receptive field (top) and SACs for which the imaged varicosity was within the SAC's predicted excitatory receptive field (bottom). Images within groups are ordered from left to right by the DSI of the indicated varicosity, starting with the varicosity with the strongest preference for outward motion at the top left. The DS of varicosities was variable, as observed in previous studies (Euler et al., 2002; Hausselt et al., 2007; Lee and Zhou, 2006; Yonehara et al., 2013) (Fig 3.11), which may arise from the following factors: 1) inability to optimally stimulate along the SAC dendritic path due to sometimes tortuous dendritic morphology (see image in row 4, column 3) and 2) limiting the stimulation to inward vs. outward may sub-optimally activate a varicosity whose preferred direction is slightly off this axis, as seen in other studies (Euler et al., 2002; Yonehara et al., 2013).

3.14F; mean ΔDSIcontrol = 0.16±0.1; ΔDSIgabazine = 0.02±0.23). Thus, both excitatory and inhibitory inputs cooperate to compute motion direction in SAC dendrites, and both are greatly enhanced by the differential dendritic distributions of inputs and outputs. Taken together, our results suggest that DS is achieved through a dendrite-intrinsic computation, which determines the outward preference as well as the circuit-level lateral inhibition of the response to inward motion.

Discussion

Directly linking neural connectivity to neuronal computations is a major goal of contemporary neuroscience. We studied the relationship between excitatory input locations and the motion direction computation that SACs perform. We found that the excitatory inputs are localized to the proximal two-thirds of the dendritic tree, mostly segregated from output sites, and that their distribution can determine the region of the dendrite where varicosities are direction selective. This differential distribution enhances the mechanisms influencing DS; both the intrinsic dendritic mechanism and the lateral inhibition mechanism. These results allowed us to determine the relative contributions from dendrite-intrinsic and circuit-level mechanisms to DS in SAC dendrites. Our findings highlight the critical importance of synaptic input placement and distribution within the dendrite in determining the types of neuronal computations performed.

Excitatory inputs to SACs

We used several approaches to demonstrate that the excitatory input distribution is mostly separated from the varicosity-rich distal dendrites. We observed this distribution in three ways: as a restricted visual receptive field using either voltage clamp recordings from the soma (Fig. 3.1) or two-photon Ca2+ imaging in distal dendrites (Fig. 3.3), as a paucity of synapses in distal dendrites detected with glutamate uncaging (Fig. 3.4), and as a decreased density of PSD95-YFP expression in distal dendrites (Fig. 3.7). These findings are consistent with two SBEM studies that found fewer bipolar cell contacts in the most distal dendrites in both On- and Off-layer SACs (Greene et al., 2016; Kim et al., 2014).

Our results indicate that there may be a different distribution of glutamate receptors in mice than in rabbit, where several studies determined that excitatory inputs are present

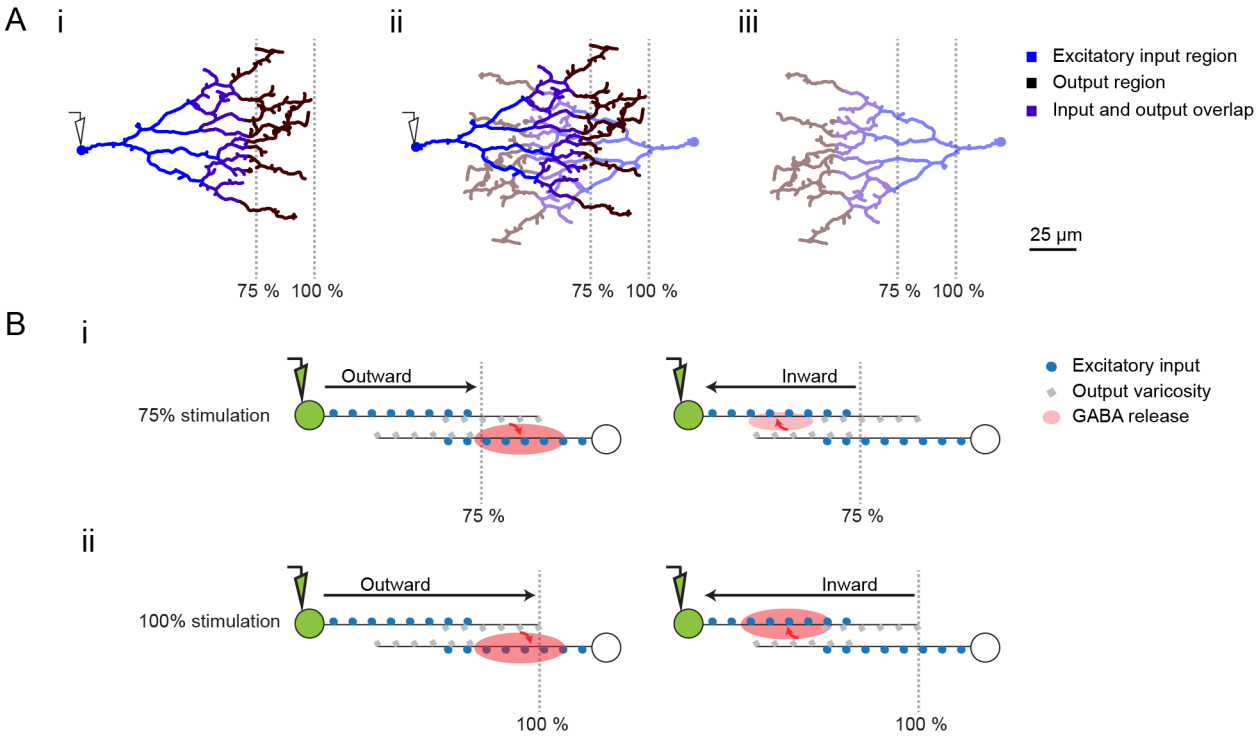

Figure 3.13 **Schematic of dendrite-autonomous contribution to circuit-level computation of motion direction.** A) i) Partial skeleton of a SAC showing the excitatory input region predicted from uncaging (blue), the varicosity-rich GABAergic output region (dark brown) and the overlapping region containing both (purple). The grey dotted lines show 75% and 100% of the dendritic radius. The details are based on reconstructions of SACs and therefore are proportional. ii) The dendrite in i overlaid with a neighboring SAC dendrite (the same dendrite rotated 180°), with somas offset by 150 µm. Their output regions overlap and provide opportunities for lateral inhibition. iii) The grey dotted lines are in the same positions as in i and ii, demonstrating the regions of the neighboring SAC stimulated when the SAC in i is stimulated over 75% vs. 100% of its dendritic radius. A much larger region of the neighboring SAC is stimulated during 100% stimulation, which could produce an increase in lateral inhibition for the recorded cell, particularly during inward stimulation (inward relative to the recorded cell). B) Schematic describing the enhancement of direction selectivity in SAC dendrites through SAC-SAC inhibitory interactions. Green cell indicates SAC filled with OGB via patch pipette (the recorded cell). White cell is a neighboring SAC. Excitatory bipolar cell inputs to SACs are blue circles, presynaptic GABA release sites on SACs are grey squares, and extent and direction of GABA release is indicated by size of red cloud and direction of red arrow, respectively. Extent of GABA release is assumed to correlate with the amplitudes of Ca^{2+} transients in putative release sites. i) SAC-SAC interactions minimally affect SAC intrinsic direction selectivity during 75% stimulation. *Left*: Outward stimulation of the recorded SAC produces a large calcium transient in its varicosities resulting in GABA release onto neighboring SACs. In contrast, the neighboring SAC experiences little excitation from this "inward" stimulation, which minimally enters its excitatory receptive field and does not induce strong summation of excitatory potentials at its varicosities. Therefore, no GABA is released onto the recorded SAC from the neighboring SAC and therefore there is minimal lateral inhibition. *Right*: Inward stimulation of the recorded SAC reduces summation of excitatory potentials in its varicosities, resulting in a smaller calcium transient compared to outward stimulation. In addition, despite the stimulation minimally entering the excitatory receptive field of the neighboring SAC, the neighboring SAC experiences greater summation of excitatory potentials due to the "outward" stimulation it receives, resulting in a small release of GABA onto the recorded SAC. The small GABA release suppresses the calcium response in the varicosities of the recorded SAC, increasing its direction selectivity. ii) SAC-SAC interactions enhance intrinsic SAC direction selectivity during 100% stimulation. *Left*: Outward stimulation of the recorded SAC produces a large calcium transient in its varicosities, resulting in GABA release onto neighboring SACs. In contrast, outward stimulation also enters a large portion of the neighboring SAC's excitatory receptive field, but the "inward" stimulation does not induce strong summation of excitatory potentials at its varicosities and inhibition from antiparallel SACs further suppresses the response. Therefore, even though the 100% stimulus causes increased excitation onto the neighboring SAC compared to the 75% stimulus, the varicosities of the neighboring

SAC still do not have enough Ca^{2+} influx to cause significant release of GABA onto the recorded SAC. *Right*: Inward stimulation of the recorded SAC reduces summation of excitatory potentials in its varicosities, resulting in a smaller Ca2+ transient compared to outward stimulation. In addition, the stimulation activates a larger portion of the neighboring SACs excitatory receptive field than during the 75% stimulation. This increased outward stimulation of the neighboring SAC results in a large release of GABA onto the recorded SAC. The large GABA release further reduces the Ca^{2+} response in the varicosities of the recorded SAC, enhancing its direction selectivity about two-fold (Fig. 3.14). In summary, SAC-SAC interactions serve to enhance the dendrite autonomous preference for outward motion we observe in SAC varicosities (Fig. 3.11). Importantly, dendrite autonomous direction selectivity also increases the importance of circuit level interactions; without the dendrite autonomous component of SAC direction selectivity, SAC-SAC signaling would cause GABA release onto a SAC even during outward motion, resulting in an overall reduction in SAC Ca^{2+} entry and a reduced preference for outward motion.

throughout the entire SAC dendritic tree. These studies also used a variety of methods, including visual receptive field mapping with ring stimuli and voltage clamp recordings (Lee and Zhou, 2006), electron microscopy (Famiglietti, 1991), and PSD95-GFP labeling (Koizumi et al., 2011). Hence, it appears that a different combination of excitatory and inhibitory distributions may account for DS in rabbit.

Mechanisms of dendritic integration in starburst amacrine cell dendrites

Overall, our findings suggest that the distribution of excitatory inputs in SACs can produce a dendrite-intrinsic DS response, with outward motion producing a larger depolarization in distal varicosities compared to inward motion (Fig. 3.9, 3.11). We found that DS was strongest for varicosities located outside of the excitatory receptive field and that more proximal varicosities are less direction selective (Fig. 3.11F,G). Two properties of SAC dendrites are the basis of this effect: the high input impedance of narrow diameter dendrites and the sealed-end of the distal dendritic compartment, which retards current flow (the "end effect", see Rall, 1964, 1967).

High input impedance of narrow diameter dendrites contributes to DS in the following way. In somatic recordings of uncaging-evoked currents, we observed a tendency of the rise time to increase and the amplitude to decrease with increasing distance along the dendrite (Fig. 3.5), although our simulations suggest that the filtering-induced reduction in amplitude is similar for inputs placed 85 or 150 μm from the soma (Fig. 3.6). Thus, it is highly unlikely that the decreased probability of detecting events in distal dendrites resulted from dendritic filtering. The narrow diameter of the dendrite (<0.3 μm) is likely to account for this filtering over the short distances in SAC dendrites (<150 μm). Numerical simulations indicate that dendritic filtering is critical for producing the slow-rising and -decaying EPSPs in varicosities during stimulation of inputs proximal to the soma (Fig. 3.9). This filtering produces the sensitivity to outward stimulation, in which larger peak depolarizations are achieved because the proximal inputs, which are distant from release sites, produce slow depolarizations in the release compartments. Outward DS results from activation of synapses progressively closer to release sites, which produces a depolarization that summates on previous EPSPs more distant from release sites, thus achieving a larger absolute peak depolarization, as opposed to stimulation in the inward direction (Rall, 1964). This effect is maximized when the output sites are not intermingled with inputs within the same compartment (Fig. 3.9D, E, I). If they were intermingled, the voltage drive of inputs close to the release sites dominates, thereby masking any slow accumulation of depolarization from more distal synapses. Thus, the separation of inputs and outputs is a global dendritic strategy used to compute motion direction (Fig. 3.1A).

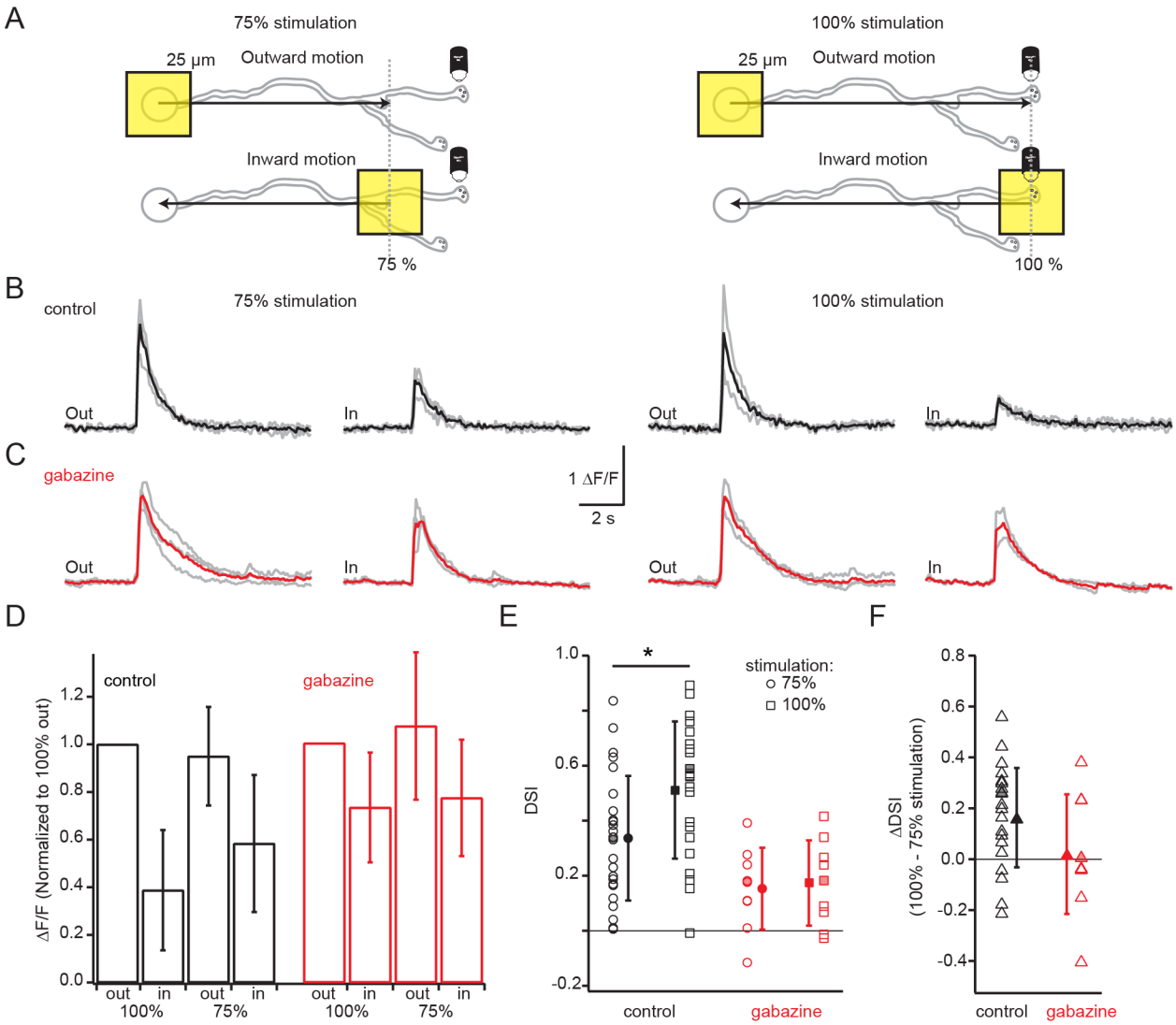

Figure 3.14 **GABAergic lateral inhibition enhances direction selectivity** A) Schematic showing imaging of a distal varicosity from an OGB-1-filled SAC presented with a 25 µm square of light moving either outward from the soma toward the distal dendrites or inward from the distal dendrites toward the soma. *Left*: Visual stimulation restricted to 75% of the dendritic radius (grey dotted line), which activated less of the lateral inhibition from neighboring SACs. *Right*: Visual stimulation of 100% of the dendritic radius (grey dotted line), which activated more of the lateral inhibition. B) Ca^{2+} responses (ΔF/F, grey) from a single varicosity following visual stimulation with a 25 µm moving square either outward from the soma toward the end of the dendrites ("out") or inward from the distal dendrites toward the soma ("in") in response to either the 75% stimulation (left traces) or the 100% stimulation (right traces) depicted in A. Black traces: averages of three trials. C) Same as B but showing the responses of a different varicosity from a different cell in the presence of 5 µm gabazine to block $GABA_a$ receptors. Red traces: averages of the three trials. D) The average maximum ΔF/F for varicosities in control conditions (black bars) in response to 100% (23 cells) or 75% (26 cells) outward and inward stimulation normalized to the response to 100% outward stimulation and in 5 µm gabazine (red, 9 cells for both 75% and 100% stimulation). The control and gabazine populations are separate. Error bars = S.D. E) Direction selective index (DSI) for the varicosities in D in response to 75% stimulation (circles) or 100% stimulation (squares) in control conditions (black) or 5 µM gabazine (red). Solid symbols = mean; error bars = S.D. * = paired t-test: $p<0.05$, n=22 varicosities for which both 75% and 100% stimulation was measured. Shaded-in symbols: example cells in B and C. F) The ΔDSI showing the difference between the DSI in response to 100% vs 75% stimulation in varicosities in control conditions (black triangles, 22 cells) and in 5 µm gabazine (red triangles, 9 cells). Solid triangles: means; error bars = S.D. Shaded-in symbols: example cells in B and C.

The second feature, the "end effect", is the property of the closed end of the dendritic compartment that essentially reflects current flow in the outward direction and leads to less voltage attenuation in the direction of the distal compartment. This is in contrast to locations near branch points or the soma, which act as current sinks. The end effect is critical for ensuring that large segments of dendrite containing release sites are subjected to a similar depolarization, despite the increased distance from the last activated input, which in turn leads to a large region of the dendrite exhibiting DS (Fig. 3.9). This could also be a mechanism for synchronizing release from varicosities at different distances from the end of the dendrite.

In this study, we created a simulation based on passive membrane properties to examine the role of the excitatory input distribution. The principle prediction is that direction selectivity of distal dendritic voltage is enhanced if inputs are segregated away from release sites (Fig. 3.9). We confirmed this enhancement by monitoring calcium responses to motion stimuli as a proxy for voltage integration at release sites (Fig. 3.11). However, it is difficult to test empirically whether the alternative case, the regular distribution of inputs located all along the dendrite, produces weaker DS at release sites. Therefore it remains to be shown directly that exclusion of synaptic inputs near release sites is necessary, as our simulations suggest, to produce DS at most of the release sites.

It is likely that non-linearities also contribute to DS. SACs express the voltage-gated potassium channel Kv3.1, which is localized to proximal dendrites and which probably enhances the electrical isolation of dendrites pointing in different directions (Ozaita et al., 2004). SACs also exhibit TTX-insensitive voltage-gated sodium channel conductances (Oesch and Taylor, 2010), which might amplify the direction selective voltage observed in our model (Fig. 3.9). Voltage-gated Ca2+ channels could also amplify direction selective voltage—both P/Q and N-type channels are expressed in SACs (Lee et al., 2010; Xu et al., 2003) and adding voltage-gated Ca2+ channels to the varicosities in our model resulted in a significant amplification of DS in SAC varicosities (data not shown). Our evidence of the presence of nonlinearities is that we observe an outward preference of the somatic voltage in response to moving square stimuli, while a purely passive model would predict a small inward direction preference for voltage recorded at the soma (Fig. 3.10; Euler et al., 2002; Gavrikov et al., 2003, 2006; Hausselt et al., 2007; Oesch and Taylor, 2010; Ozaita et al., 2004). Directly measuring voltage in SAC dendrites would provide a basis for determining the contribution of each non-linearity to the amplification of passive DS. Finally, the cooperative binding of neurotransmitter release sensors (e.g. Kochubey et al., 2009) will likely contribute to amplification of DS release of GABA onto DSGCs.

A unifying model of SAC direction selectivity

So far, three models of how DS arises in SAC dendrites have been proposed. First, the space-time wiring model by Kim et al. (2014) proposes that bipolar cells with phasic vs. sustained release kinetics synapsing onto different regions of the dendrite produce a delay-line computation of DS. As shown in Fig. 3.2, our voltage clamp recordings do not show detectable differences in bipolar cell release kinetics at different sites along the dendrite. However, the ideal experiment to test this model would be to record from bipolar cell-SAC pairs to test directly for differences in release kinetics.

Second, the lateral inhibition model postulates that DS in SACs arises due to lateral inhibition from other SACs. SACs release GABA onto one another (Kostadinov and Sanes,

2015; Lee and Zhou, 2006; Zheng et al., 2004) and a previous study demonstrated that the DS of Ca2+ responses in proximal varicosities requires surround stimulation in rabbit SACs (Lee and Zhou, 2006). This inhibition mechanism relies on the ability of GABA receptor activation to shunt excitation when inhibition arrives first (Münch and Werblin, 2006). However, other studies in rabbit retina have found that blocking GABA receptors did not affect direction selective responses in one example of dendritic Ca2+ imaging (Euler et al., 2002) or in direction selective responses as measured by voltage clamp recordings at the soma (Hausselt et al., 2007; Oesch and Taylor, 2010).

We found that lateral inhibition enhanced, but was not required for, DS in distal varicosities (Fig. 3.14). First, stimulating out to 100% of the dendritic tree, which maximally stimulates antiparallel presynaptic SAC dendrites, led to a larger DS than stimulation to 75% of the dendritic tree. Second, blockade of GABAA signaling reduced DS in distal varicosities, primarily by increasing the dendritic response to inward motion. It is important to note that a bath application of gabazine not only affects SAC-SAC interactions, but will also affect wide-field amacrine cell inputs to SACs (Hoggarth et al., 2015) as well as the amount of glutamate released from bipolar cells, due to a relief of presynaptic inhibition (Pei et al., 2015). However, GABA release from wide-field amacrine cells should not be DS, and the distribution of bipolar cell inputs on SACs allows them to maintain DS despite potential increases in glutamate release.

Our data are more in favor of a third model in which DS arises through a dendrite-intrinsic mechanism. In this model, the excitatory input distribution and passive cable properties described here contribute to the direction selectivity of dendritic voltage, and hence synaptic output. In addition, the differential distribution of inputs and outputs contributes to a circuit-based mechanism of DS in which lateral inhibition from neighboring SACs enhances DS. Overall, our findings suggest a model where the dendrite-intrinsic direction preference is enhanced by lateral inhibition from other SACs, a circuit-level interaction that itself requires the presence of the dendrite-intrinsic mechanism, leading to robust direction selectivity in SAC dendrites (Fig. 3.13).

Chapter IV

Development and Computational Properties of Starburst Amacrine Cell Dendrites: Preliminary Investigations

This Chapter comprises previously unpublished data collected with Ryan B. Morrie, Alexandra Tran-Van-Minh, Vasha DuTell, David A. DiGregorio, and Marla B. Feller. The work is included with permission from all collaborators.

Introduction

In previous chapters, I've argued that SACs provide the crucial direction selective signal for DSGCs to compute the direction of image motion. In Chapter 2, I showed that manipulating excitatory inputs to starburst amacrine cells by altering the inputs' polarity leads to a marked change in the tuning direction of direction selective ganglion cells (Vlasits et al., 2014). In Chapter 3, I demonstrated that the direction selective computation in the SAC dendrites originates from the passive properties of their dendrites and a precise distribution of excitatory inputs onto those dendrites, which combine with lateral inhibition to produce direction selective calcium transients in the dendrites (Vlasits et al., 2016). However, many details about the mechanism by which SAC dendrites compute the direction of image motion remain to be determined. In addition, revelations from recent studies have led to new questions in the field of direction selectivity.

For instance, two recent studies that described the tuning properties of DSGCs during development suggest that SACs' dendritic tuning may be optimized after eye-opening (postnatal day 14, P14)(Bos et al., 2016; Rosa et al., 2016). One of these studies recorded spikes from individual DSGCs at different ages and showed that DSGCs at P11-15 are more weakly tuned than in an adults (>P30) (Rosa et al., 2016). Another study showed that DSGCs are tuned at eye-opening, but that their tuning was not clustered around the four cardinal directions at this age (unlike in adults) (Bos et al., 2016). Given the crucial role of SACs in these computations and the proposed reliance on excitatory input location in their computation (see Chapter 3), one possible mechanism for weak, unclustered tuning of DSGCs is immature computational abilities of SACs because of unrefined targeting of excitatory inputs to their dendrites. I present some preliminary experiments in support of this theory in the first half of this chapter and discuss some future directions for research.

In the second half the chapter, I take a closer look at the computational properties of SAC dendrites using apparent motion stimuli, also called beta movement stimuli, which have been used as visual illusions to dissect motion detection in the optometry literature (Eagleman, 2001). Apparent motion stimuli, in which the amount of time between presentations of adjacent stationary spots is varied, can elucidate the supra- or sub-linearity of SAC computations and also allow for an evaluation of the velocity tuning of the dendrites. My preliminary experiments suggest that SAC dendrites may appear to behave sublinearly or supralinearly under certain stimulus conditions, and that their velocity tuning is very broad. I conclude the chapter with a discussion of some future directions for determining the importance of these features for the DS circuit.

Methods

Ethics statement

All animal procedures were approved by the UC Berkeley Institutional Animal Care and Use Committee and conformed to the NIH Guide for the Care and Use of Laboratory Animals, the Public Health Service Policy, and the SFN Policy on the Use of Animals in Neuroscience Research.

Animals and tissue preparation

Mice of either sex were anesthetized with isoflurane and decapitated. Retinas were dissected from enucleated eyes under infrared illumination and isolated retinas were mounted over a 1-2 mm^2 hole in filter paper (Millipore) with the photoreceptor layer side down. Mounted retinas were stored in oxygenated Ames' media (US Biological or Sigma) in the dark at room temperature prior to imaging and recording.

To target SACs for whole cell recordings and calcium imaging, we used two mouse lines that express fluorescent proteins in SACs: *mGluR2-GFP* mice that contain a transgene insertion of the interleukin-2 receptor fused to GFP under control of the mGluR2 promoter (Watanabe et al., 1998); and *ChAT-Cre/nGFP* mice generated by crossing a mouse in which *IRES-Cre* recombinase was knocked in downstream of the endogenous choline acetyltransferase gene (Ivanova et al., 2010) (B6.129S6-*ChAT*$^{tm2(cre)Lowl}$*/J*; Jackson Labs) (Chat-cre) with a mouse line containing a *loxP*-flanked STOP cassette upstream of the GFP gene containing a nuclear-localization sequence (Stoller et al., 2008) (B6.129-*Gt(ROSA)26Sor*^{tm1Joe}/J; Jackson Labs). For some experiments, ChAT-Cre mice without the nGFP transgene or wild-type (C57BL/6J; Jackson Labs) mice were used. In these experiments SAC identity was confirmed by fluorescence imaging of dye-filled cells at the end of the experiment. For studying development of SACs, adults (P30-80) were compared with mice at the age of eye-opening, P13-14. Some of the young mice had their eyes open while others' eyes were closed - no obvious differences were observed between these populations. For measuring receptive fields in Sema6a knockout mice, we generated a mouse line in which SACs were labeled using nGFP (as described above) crossed to obtain Sema6a(-/-) (see Sun et al. *Science*, 2013).

Receptive field mapping with stationary ring stimuli

Methods were previously described in Vlasits et al. (2016). In brief, SACs were targeted for voltage clamp recording in an external Ames media with a cesium internal solution containing Alexa-594. IR illumination and 2-photon microscopy were used to target cells for patching using a custom-built microscope with the laser tuned to 810 nm for Alexa-594 imaging and 930 for GFP imaging. Visual stimuli were generated using a DMD projector with an LED light source with 485 nm wavelength projected onto the photoreceptors. Stimuli were presented in pseudorandom order. Light intensity for comparing WT and Sema6a KO mice was 1.5 x 10^5 over a background of 6 x 10^3 R*/s/Rod. Light intensity for recordings comparing animals at eye opening and adulthood was brighter because dimmer stimuli produced variable results at young ages. The intensity was 5.6 x 10^5 R*/s/Rod over a background of 1.6 x 10^4 R*/s/Rod.

Calcium imaging of SAC release sites using sharp electrodes

These experiments were performed on the same setup as that used for receptive field mapping with rings (see above). The sharp electrode filling procedure was described in Ding et al. *Nature* (2016). One exception to this procedure was that SAC cell identity was determined using 2-photon imaging of labeled cells, then the sharp electrode was positioned on the cell and driven to puncture through the inner limiting membrane under IR illumination, and then imaging was switched back to 2-photon to fill the cell with OGB-1.

After a 30 minute incubation to allow cells to recover from sharp electrode puncture, fields of view of area ~40 μm^2 were imaged at 7.58 Hz during presentation of visual stimuli,

leading to collection of many small regions of interest (ROIs) within a field of view. Cells in which no noticeable light response was observed were discarded, as these cells were presumed to have died during filling. An attempt was made to image all of the dendrites in a quadrant of the SAC, and fields of view that were located more distally vs. proximally were noted during acquisition. Occasionally, the same field of view was imaged more than once – in this case the second dataset was discarded during analysis.

Visual stimuli consisted of moving bars (400 μm wide, 200 μm long) that traversed a diameter of 350 μm, with the SAC soma in the center. The bars moved in eight directions presented in pseudorandom order. The retina was allowed to adapt to the 2-photon laser scanning for 20 s before beginning visual stimulation.

Calcium imaging and apparent motion

Here, the imaging setup was the same as for receptive field mapping with rings (see above). Patch clamp electrodes were filled with an internal solution containing (in mM): 116 D-gluconic acid (K+ salt), 6 KCl, 2 NaCl, 20 HEPES, 4 adenosine 5'-triphosphate (magnesium salt), 0.3 guanosine 5'-triphosphate (trisodium salt), 10 phosphocreatine (disodium salt), 0.15 Oregon Green 488 BAPTA-1 hexapostassium salt (OGB-1; Life Technologies) and KOH to pH 7.25. Membrane potentials reported here are after correction for the liquid junction potential (-8.6mV). Cells were held in current clamp for calcium imaging experiments and recordings were acquired at 10kHz. Cells resting above -48 mV were injected with negative current (maximum -150 pA) to achieve a resting potential < -48mV. Cells that did not hyperpolarize below -48mV upon current injection were discarded from analysis.

OGB-1 visualization was performed at 930 nm to reduce the light response of the retina during scanning (Denk and Detwiler, 1999). After break-in, the distal end of a dendrite, as well as a single varicosity on that dendrite, were identified as quickly as possible with minimal exposure to the 2-photon laser (6±2 minutes after break in). A small region of interest (2-6 μm^2) that included the varicosity was imaged at either 11.84 Hz (64 x 64 pixels).

The apparent motion stimulus consisted of two 24 μm diameter spots presented for 16.7 ms at two positions at a known distance from the soma of the SAC (see Fig. 4.5A). The intensity of the light stimulus was 1.9 x 10^5 R*/s/Rod on a black background. Stimuli were presented either individually or in sequence to create apparent motion. The duration of time between presentation of the two spots was varied as follows in the table below. The total distance spanned by the spots was 65 μm, allowing for a calculation of the apparent velocity. Each stimulus location was presented three times.

Table 4.1 Spot timing for apparent velocities

Time between spots (s)	Apparent velocity (μm/s)
1.562	25
0.782	50
0.382	100
0.16	200
0.066	400
0.033	800
0.016	1200

Current clamp recordings and apparent motion

Current clamp recordings were performed on a custom-built 2-photon microscope previously described in Wei et al. (2010). 2-photon imaging was used to target cells for whole-cell recording. External solution was Ames media. Internal solution consisted of (in mM): 116 D-gluconic acid (K+ salt), 6 KCl, 2 NaCl, 20 HEPES, 4 adenosine 5'-triphosphate (magnesium salt), 0.5 EGTA, 0.3 guanosine 5'-triphosphate (trisodium salt), 10 phosphocreatine (disodium salt), and KOH to pH 7.25. Cells were evaluated to have a holding current of less than 100 pA and discarded if the holding current required to keep the cell at -60 mV changed dramatically.

The visual stimuli for apparent motion was similar to that described for calcium imaging, with the following differences. Here, spots were adjacent to one another and 40 μm diameter, spanning a total distance of 80 μm (Fig. 4.4E). Both the time between spots and the amount of time the spot was presented were altered to achieve the velocities measured here (326 and 544 μm/s). For the slow velocity, the spot was on for 58 ms and the time between spots was 58 ms. For the fast velocity, the spot was on for 35 ms and the time between spots was 35 ms.

Measuring integration using glutamate uncaging

Glutamate uncaging methods and microscope were previously described in Vlasits et al. *Neuron* (2016 – see extended experimental procedures). In brief, retinas were prepared as described above except that dissections of wild-type mice were done in ambient light and tissue was stored in oxygenated ACSF. Voltage and current clamp recordings were performed in a potassium-based internal solution. Dendritic arbors were imaged using a 2-photon microscope tuned to 810 nm. Caged MNI-glutamate (4-methoxy-7-nitroindolinyl-caged L-glutamate, Tocris Bioscience) was bath applied at a concentration of 2 mM (in ACSF) and glutamate was uncaged using a 405 nm laser with power = 2.55 mW.

Analysis

Data analysis was performed in IgorPro (WaveMetrics) running Neuromatic functions and custom procedures, ImageJ, FIJI, Excel, and MATLAB running custom programs. Receptive field mapping analysis was performed as described in Vlasits et al. (2016).

For calcium imaging in development, image processing was performed as described in Vlasits et al. (2016). A threshold above background was used to detect the presence of ROIs automatically using MATLAB. ROIs were then hand-selected from images if they had a noticeable light response to at least some of the visual stimuli. For each ROI, the maximum amplitude of the average response to each of eight directions was calculated. The normalized vector sum of these responses was used to determine the preferred angle and magnitude of the vector sum, calculated as:

$$\sum_{i=1}^{n} \frac{\max(i)}{\sum \max(i)}$$

where *n* is the number of directions and max describes the maximum amplitude response to a given direction. Cells were grouped as distal vs. proximal based on post-hoc viewing of field-of-view locations in projection images of the entire cell. For example, if a field-of-view was

primarily proximal, all of the ROIs in that field of view were labeled proximal. The example ROIs shown in Fig. 4.2B-C were chosen because they had vector sum magnitudes values near the average vector sum magnitude for proximal vs. distal ROIs respectively.

For apparent motion and glutamate uncaging experiments, the predicted response based on summing individual responses was calculated by adding a delay to each individual response based on the stimulus timing and summing the resulting arrays.

The linearity index for current clamp recordings in response to apparent motion (Fig. 4.4G) was computed by measuring the max amplitude of the summed response (sum) and comparing to the amplitude of the apparent motion trace at the same time (real), then computing [real – sum]/[real+sum].

The direction selective index for measuring apparent velocity (Fig. 4.5E) is the maximum amplitude for outward (out) vs. inward (in) stimulation calculated as [out – in]/[out].

Results and Discussion

Preliminary comparison between SAC receptive fields at eye-opening and in adults

Previously, experiments examining the development of the direction selective circuit have focused on the wiring of SACs to DSGCs (Morrie and Feller, 2015; Wei et al., 2011) and the participation of these circuit elements spontaneous retinal waves (Zheng et al., 2004). These studies showed that SACs are already forming connections with DSGCs at P8 and that the number of connections between SAC dendrites oriented in a DSGCs' null direction increases dramatically from P8 to P14. Mice open their eyes between P13-4, and thus, DSGCs would be expected to be tuned at this age. However, as mentioned in the Introduction, DSGCs appear to be more weakly tuned and their clustering around the cardinal directions has not yet matured (Bos et al., 2016; Rosa et al., 2016). Because connections between bipolar cells and their post-synaptic partners is still maturing at eye-opening, one possibility is that excitatory connections to SACs that are necessary for detection of image motion direction have not yet refined to be restricted from the distal dendrites.

To begin to examine whether SACs at eye-opening have the mature wiring with their excitatory presynaptic partners, we measured the excitatory receptive field of SACs at either P13-14 or in adults. We presented stationary ring stimuli projected onto the photoreceptors and recorded the excitatory and inhibitory currents by recording in voltage clamp from the SAC soma (Holding potentials of -72 mV and 0 mV, respectively; Fig. 4.1A-B). As observed previously (Vlasits et al., 2016), SACs in adulthood have a clearly defined On response to ring stimulation, with the response getting smaller and smaller as the rings are presented at radii further from the soma (Fig. 4.1B, right). At P13-14, SACs also showed a clear On response in their excitatory current, but the measured current tended to be larger in amplitude and the On response was present at radii farther from the soma (Fig 4.1B, left). The kinetics of inhibitory currents also appeared to differ between young mice and adults, however we did not explore that difference further here.

We observed two physiological properties of SACs that were different between eye-opening and adulthood. First, spontaneous activity when recording at -72 mV, which has been previously shown to be quite active in adult SACs , was almost absent in cells from young animals (Fig. 4.1C). This suggests that bipolar cell release is less active, possibly due to chronically hyperpolarized bipolar cells, at eye-opening. Thus, SACs might have higher

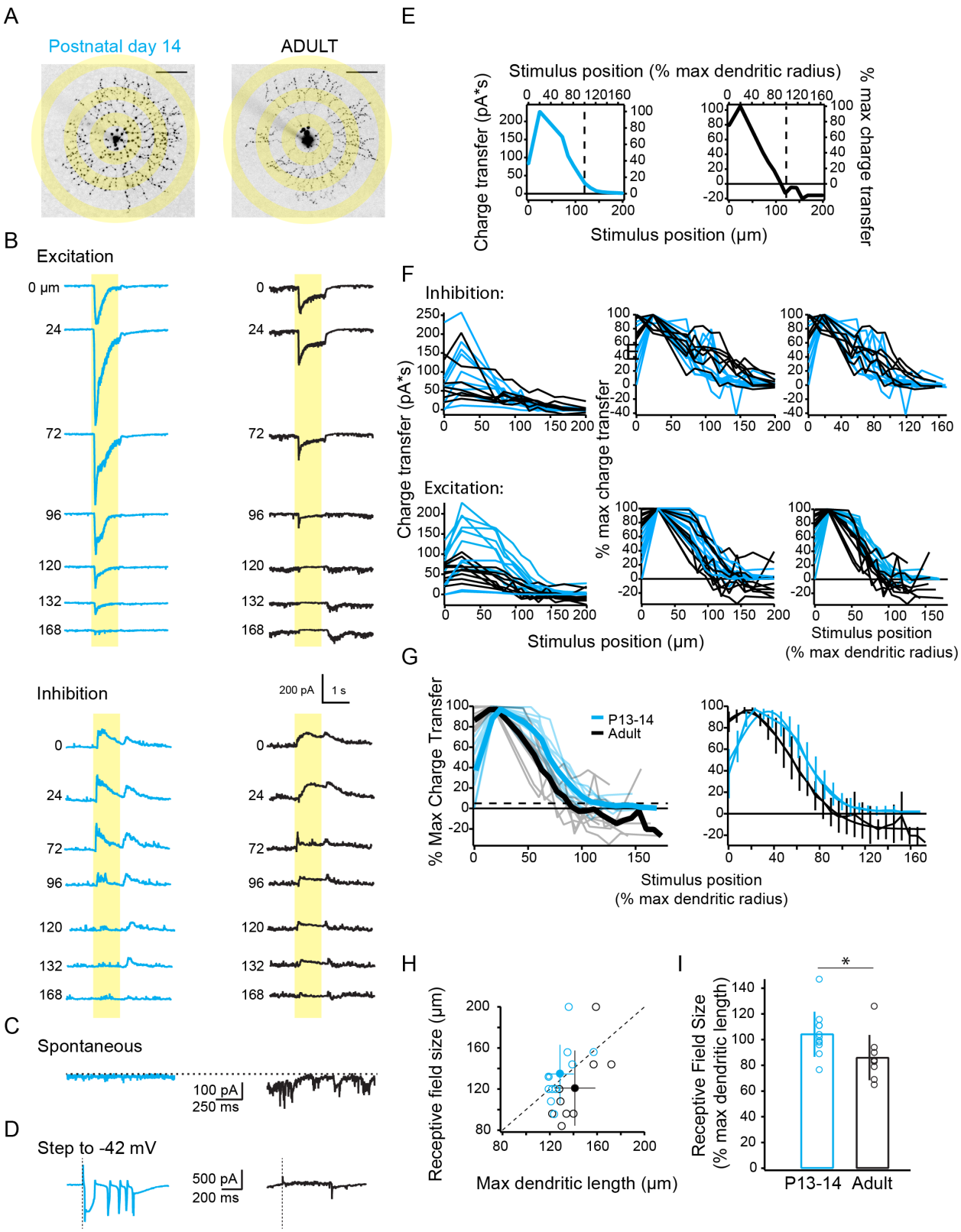

Figure 4.1 **Preliminary comparison between SAC receptive fields at eye-opening and in adults.** A) Schematic showing 2-photon fluorescence projections of SACs filled with Alexa-594 via patch pipet at eye-opening (left) and adult ages (right). Yellow rings demonstrate position of stationary ring stimuli with inner radii of 24, 72 and 132 µm that were projected over the photoreceptors. Rings were 24 µm thick. Scale bar: 50 µm. B) Voltage clamp

recordings of excitatory (holding potential -72 mV) and inhibitory (holding potential 0 mV) currents recorded from the SACs in A during presentation of 1 s stationary ring stimuli at the distances from the soma to inner radius of the ring indicated to the left of each trace. Eye opening: left, blue traces. Adult: right, black traces. Yellow boxes: period when the stimulus was presented. C) Voltage clamp recordings from the cells in A measuring spontaneous excitatory currents (holding potential -72 mV) at eye-opening (blue, left) and in adult (black, right). D) Voltage clamp recordings from the cells in A showing the response to a step from -72 mV to -42 mV. SACs at eye-opening (left, blue) exhibit unclamped voltage activated currents, while adult SACs (right, black) do not. Dotted line indicates beginning of step. E) Excitatory receptive fields of the cells in A measured as the charge transfer during the period when the stimulus was present as a function of the stimulus position. Top axis normalizes the stimulus position to the maximum dendritic radius measured from the projecting image (dotted line). Right axis normalizes the charge transfer to the maximum value measured. F) Excitatory and inhibitory receptive fields for all cells in the experiment. Left shows charge transfer as a function of stimulus position, middle shows normalized charge transfer as a function of stimulus position, and right shows normalized charge transfer as a function of normalized stimulus position. Eye opening (blue): n=11. Adult (black): n=9. G) Left: average excitatory receptive field for SACs at eye-opening (thick blue line) and in adults (thick black line). Thin traces are individual cells as show in F (bottom right plot). The dotted line shows the 5% of maximum charge transfer used to calculate the receptive field size for each cell. Right: Average traces plotted with standard deviation and Gaussian fits. H) Each cells receptive field size plotted against its maximum dendritic length (open circles). Filled circles show averages and standard deviations for adults (black) and eye-opening (blue). Dotted line is the unity line. I) Average receptive field size as a % of the maximum dendritic radius for SACs at eye-opening (blue) and in adults (black). Error bar is standard deviation. Open circles are individual cells. * = $p < 0.05$, Wilcoxon rank test (two-tailed).

membrane resistance and a lower resting membrane potential at eye-opening, which could alter how they integrate their inputs. Further experiments that determine the resting membrane potential, for instance with a voltage sensitive fluorescent indicator, would be necessary to further explore this.

Second, when stepping from -72 mV to -42 mV (Δ+30 mV), unclamped voltage-gated conductances were observed in SACs at P13-14 (Fig. 4.1D). Unclamped voltage-gated conductances are not observed in adult SACs. These results suggest that, during late development, SACs are electrically distinct from adults. One possibility is that the smaller dendritic lengths of these cells (combined with the higher membrane resistance because of lower spontaneous excitatory input described above) leads to differences in the ability to clamp SACs at eye opening. In addition, there may be distinct voltage activated conductances, or voltage activated conductances located closer to the soma, in SACs at eye-opening.

Next we quantified the receptive field sizes using the charge transfer measured from the voltage clamp recordings in Fig. 4.1B and the dendritic field radii determined using projection images of the dye-filled SACs imaged with a 2-photon microscope following stimulation (Fig. 4.1E). From this, we could clearly see in the example cells that the excitatory receptive field is smaller than the dendritic field in adult (as previously describe), but that the excitatory receptive field is about the same size as the dendritic field at eye-opening. We measured the excitatory receptive field relative to dendritic field in populations of SACs in each age group and found that, in general, the excitatory receptive field was larger at eye opening when normalized to the maximum dendritic radius (Fig. 4.1F-G). The receptive field size for inhibition was more equivalent across ages and no further analysis was performed (Fig. 4.1F). When we defined the extent of the excitatory receptive field as the point where the charge transfer reaches 5% of the maximum charge transfer for a given cell, we found that SACs at eye opening tended to have larger receptive fields (135 ± 29 μm for P13-4 SACs vs. 121 ± 37 μm for adult) even when the size of their dendritic fields trended smaller (129 ± 12 μm for P13-14 SACs vs. 141 ± 17 μm for adult) (Fig. 4.1H). Normalized to the max dendritic radius, the receptive fields of SACs at eye

opening are significantly larger than receptive fields of SACs at eye-opening (105 ± 18% for P13-14 SACs vs. 86 ± 18% for adults, Wilcoxon Rank test $p<0.05$) (Fig. 4.1I).

Overall, these results suggest that there are substantial differences in the physiology of SACs at eye opening. In particular, it appears that there are excitatory inputs targeted to distal dendrites. One possibility is that these inputs are pruned during the first few weeks after eye-opening which would optimize the SAC for computing image direction. Further research should confirm these results by observing the anatomical distribution of excitatory inputs (Ding et al., 2016; Kim et al., 2014; Koizumi et al., 2011; Vlasits et al., 2016). In addition, it would be interesting to perform these experiments at several intermediate ages in order to determine how the receptive field progresses from the eye-opening state to the adult state, which may give hits about the mechanism of refinement. Because visual input has been observed to play a role in the clustering of DSGCs along the cardinal axes (Bos et al., 2016), measuring the excitatory receptive field in dark-reared adult mice may also be interesting. A further exploration of how the inhibitory connections to SACs develop is also warranted, given these inputs important role in shaping the strength of dendritic direction selectivity in mice (Chen et al., 2016; Ding et al., 2016; Vlasits et al., 2016).

Preliminary examination of tuning of distal and proximal varicosities in SACs at eye-opening

Previously, it was demonstrated in a simulation that restricting the excitatory inputs from the distal dendrites of SACs resulted in more consistent direction selectivity at putative release sites. Given the differences in excitatory receptive field described in Fig. 4.1, we wanted to determine whether SAC dendrites are tuned at eye-opening. To measure this, we performed calcium imaging during visual stimulation with moving bars in eight directions and measured the tuning of varicosities across an entire quadrant of the SACs' dendrites (method from Ding et al. 2016; Fig. 4.2A). We observed that varicosities had a range of tuning strengths, with proximal varicosities being less tuned than distal varicosities (Fig. 4.2B-C), similar to previously observed proximal-distal differences using a different measure in adults (Vlasits et al., 2016). To further examine this, we plotted the preferred angle and vector sum for each varicosity measured in the quadrant for two cells, separating the ROIs into proximal and distal based on whether the whole field of view was primarily over a proximal or distal region of the dendritic arbor (Fig. 4.2D). This analysis revealed that, on average, proximal ROIs are less strongly tuned than distal ROIs (vector sum for proximal = 0.097 ± 0.05 vs. distal = 0.18 ± 0.07; Wilcoxon rank sum test $p<0.001$). In addition, proximal ROIs appeared to have a wider spread of preferred angles than distal ROIs, suggesting that proximal ROIs lack a consistent preference for outward motion along the dendrite. There is a clear difference in the distribution of tuning between proximal and distal ROIs in this preliminary dataset, with distal ROIs have markedly larger vector sum magnitudes (Fig. 4.2E).

Overall, these results suggest that at least some SAC varicosities are tuned at eye-opening. There is a range of tuning strength that can be at least partially explained by the position of the varicosities on the SAC dendrites, with distal dendritic regions being more strongly tuned than proximal regions. Without a direct comparison to the tuning of adult dendrites treated in the exact same manner, making conclusions about whether SACs are less well tuned at eye-opening than in adults is not possible. However, based on comparison to a recent paper that used the same stimulus and dye-filling method to measure distal dendrites of SACs (Ding et al., 2016), the ROIs measured here are in general more weakly tuned than in that

study, in which a large proportion of ROIs had direction selective index values above 0.5. Thus, these preliminary data suggest that comparison of the relative tuning strength of young and adult SACs provide relevant information for the mechanism of DSGC tuning maturation. Ideally, these future experiments would more measure the relative positions of varicosities on the SAC dendrites and perform pharmacology to isolate the contribution of the excitatory inputs to the computation from the inhibitory inputs (as in Ding et al., 2016; Vlasits et al., 2016).

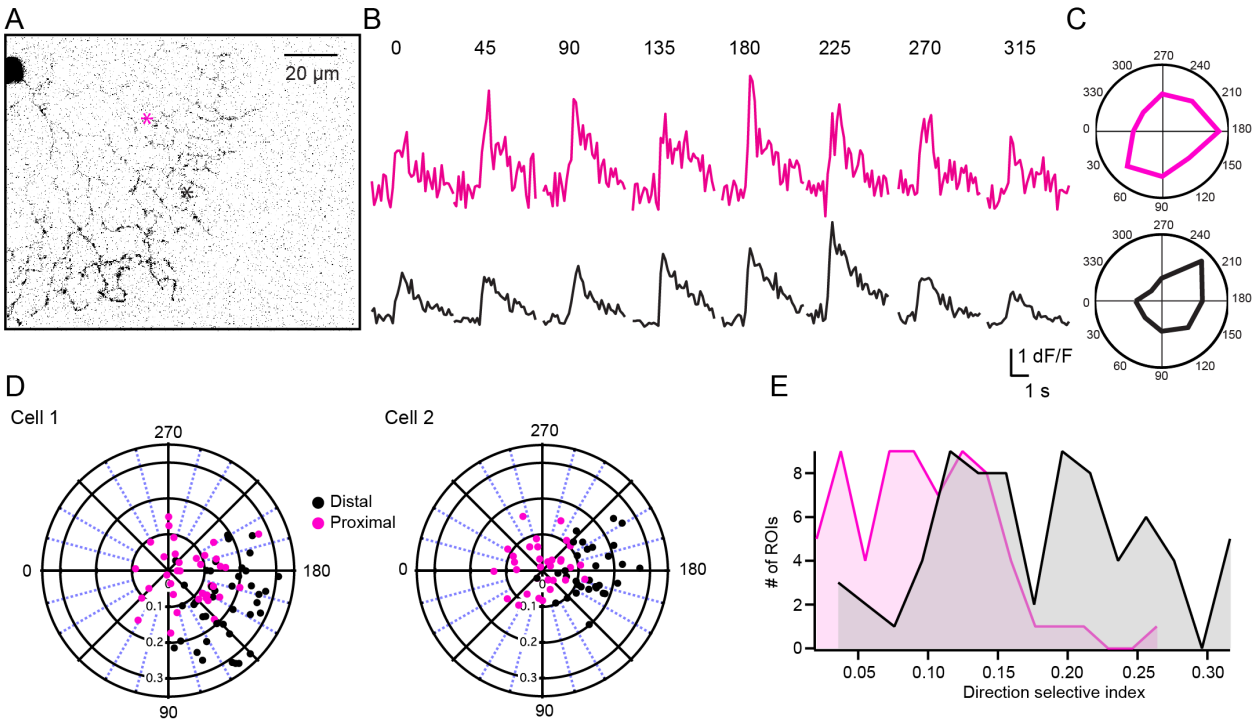

Figure 4.2 **Preliminary comparison of tuning of distal and proximal varicosities in SACs at eye-opening.** A) 2-photon fluorescence projection image of a SAC from a P13 mouse filled with Oregon Green BAPTA via electroporation with a sharp electrode. Asterisks indicate locations of varicosities (pink = proximal, black = distal) imaged in B. The cell's soma is at the top left. B) Calcium transients recorded from the regions of interest indicated by asterisks in A in response to moving bar stimulus presented in 8 directions indicated above the traces. C) Polar plots showing the maximum amplitudes of the calcium transients in B. The proximal region of interest (pink, top) has a vector sum magnitude of 0.11 and the distal region (black, bottom) has a vector sum magnitude of 0.22. D) Polar plots showing the vector sum magnitude (radius) and preferred angle for regions of interest (filled circles) from two different SACs from the same P13 animal. Regions were grouped into proximal to the soma (pink) vs. distal to the soma (black) based on whether the field of view of each ROI was mostly proximal or distal. E) Histograms of vector sum magnitudes of proximal (pink) and distal (black) regions of interest.

Preliminary description of excitatory receptive fields of adult Sema6a starburst amacrine cells

To further explore how SAC maturation relates to the refinement of the direction selective computation, we explored the physiology of SACs in adult animals in which normal development is altered by mutating a crucial signaling molecule. Sema6a is a membrane-bound signaling molecule expressed in SACs that is involved in dendritic self-avoidance (Morrie and Feller, 2016; Sun et al., 2013). SACs in mice lacking Sema6a have smaller dendritic arbors, dendrites that cross abnormally, and are generally not radially-symmetric. A previous study

showed that DSGCs in a Sema6a knockout mouse (Sema6a KO) had reduced tuning of the On response(Sun et al., 2013). One mechanism for this reduced tuning could be reduced tuning and altered excitatory receptive fields of SACs.

To explore this possibility, we measured the excitatory receptive fields of SACs in wild type and Sema6a KO mice using the ring stimulation and voltage clamp recordings (as described in Fig. 4.1; Fig. 4.3A). We observed excitatory and inhibitory On responses (Fig. 4.3B) and found that the excitatory receptive field was about the same size in KO and wild type SACs (Fig. 4.3C), despite the fact that KO SACs have significantly smaller dendritic radii (Fig. 4.3D). When we normalized the receptive field size to the maximum dendritic radius, we found that the average excitatory receptive field in the KO SACs extended beyond the dendritic field, in contrast to wild types (Fig. 4.3E, left). These results suggest that in addition to the substantial morphological differences observed in these KO mice, bipolar cell targeting to SAC dendrites is altered.

These results lead to more questions than answers. A more precise method of determining where the excitatory inputs arise, for instance using anatomical mapping of bipolar cell inputs to SACs in combination with glutamate uncaging (Vlasits et al., 2016) would clear up how the receptive field could be larger than the dendritic field in these cells. Furthermore, connecting the difference in excitatory receptive field size in Sema6a KO to the differences observed in DSGC tuning requires first determining whether SAC varicosities in the Sema6a KO are tuned in a similar manner as was done in Fig. 4.2. In addition, determining whether the altered tuning in DSGCs is a result of poorly tuned inhibition will be necessary as well.

Glutamatergic integration is more sublinear during outward apparent motion when measured from the soma

In this second half of Chapter IV, I transition to dissecting additional properties of SAC dendrites that may enable them to robustly compute motion direction. In particular, we utilized apparent motion stimuli to inquire about spatiotemporal computations. For this section, the apparent motion stimuli were useful for determining how multiple stationary inputs are integrated together when presented in a specific temporal sequence, and whether that integration is different when the apparent motion direction is changed. This allows for analysis of how multiple inputs are "added up" by the SAC dendrite.

First, we sought to measure the contributions of excitatory inputs on the dendrites, individually or in sequence, to the membrane potential of a SAC as measured at the soma. To do this, we performed glutamate uncaging along SAC dendrites and measured current clamp recordings from the SAC soma. We measured responses to individual uncaging locations and responses to ten uncaging locations activated in sequence 10 ms apart, either outward along the dendrite or inward toward the soma. We found that, in this preliminary result from one cell, sequential activation of the inputs in the outward direction (centrifugal) resulted in a smaller response than inward apparent motion (centripetal) (Fig. 4.4A, green traces). When we compared these responses to the linear sum of the responses (Fig. 4.4A, black trace) to individual uncaging locations (Fig. 4.4A-B, grey traces), we observed that both outward and inward sequential stimulation resulted in somewhat sublinear excitatory post-synaptic potentials. This result is complimentary to simulated results with a passive cable model for thin dendrites (Vlasits et al., 2016), suggesting that, at least with small depolarizations, the SAC dendrites behave passively. That these are exclusively passive inputs in this experiment is also borne out by the fact that the

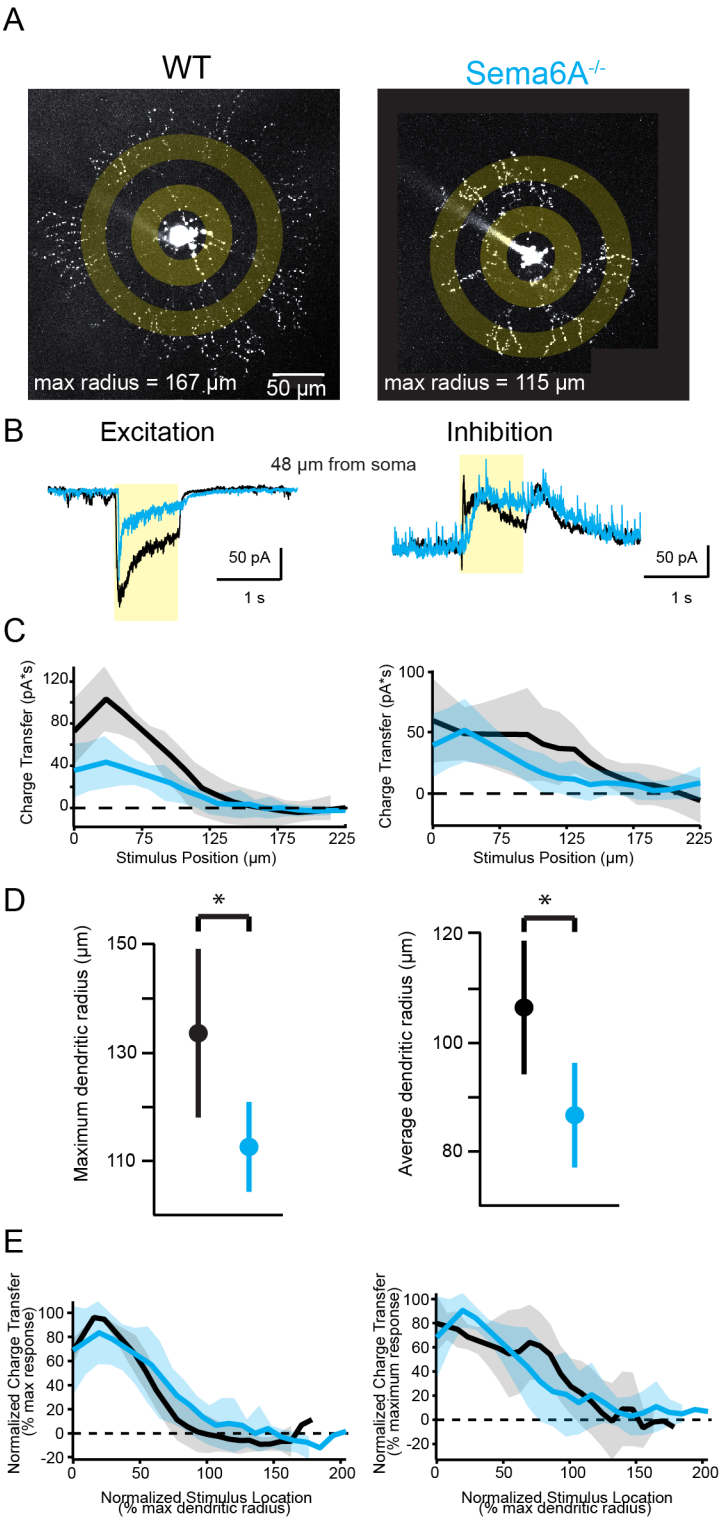

Figure 4.3 **Preliminary description of excitatory receptive fields of adult Sema6a starburst amacrine cells** A) Schematic showing 2-photon fluorescence images of SACs from wild-type (WT) and Sema6a knockout (KO) animals together with the position of stationary ring stimuli (yellow rings) presented to the photoreceptors at inner radii 24 and 72 µm from the soma of the SAC. B) Excitatory and inhibitory currents measured from the cells in A in response to a stationary ring with inner radius at 48 µm from the soma. Yellow bar indicates the timing of the presentation of the ring. Black: WT, blue: Sema6a KO. C) Plot of the average excitatory (left) and inhibitory (right) charge transfer in response to stationary ring stimuli for a population of WT (black, n=6 cells) and Sema6a KO (blue, n=7 cells) SACs as a function of inner radius of ring stimuli. Shaded area is standard deviation. D) The maximum and average dendritic radii for SACs represented in C. * = wilcoxon rank test with $p < 0.05$. E) Plot of the average excitatory charge transfer normalized to the maximum charge transfer for each cell as a function of the stimulus position normalized to the maximum dendritic radius. Shaded area is the standard deviation. Colors and sample sizes as in C.

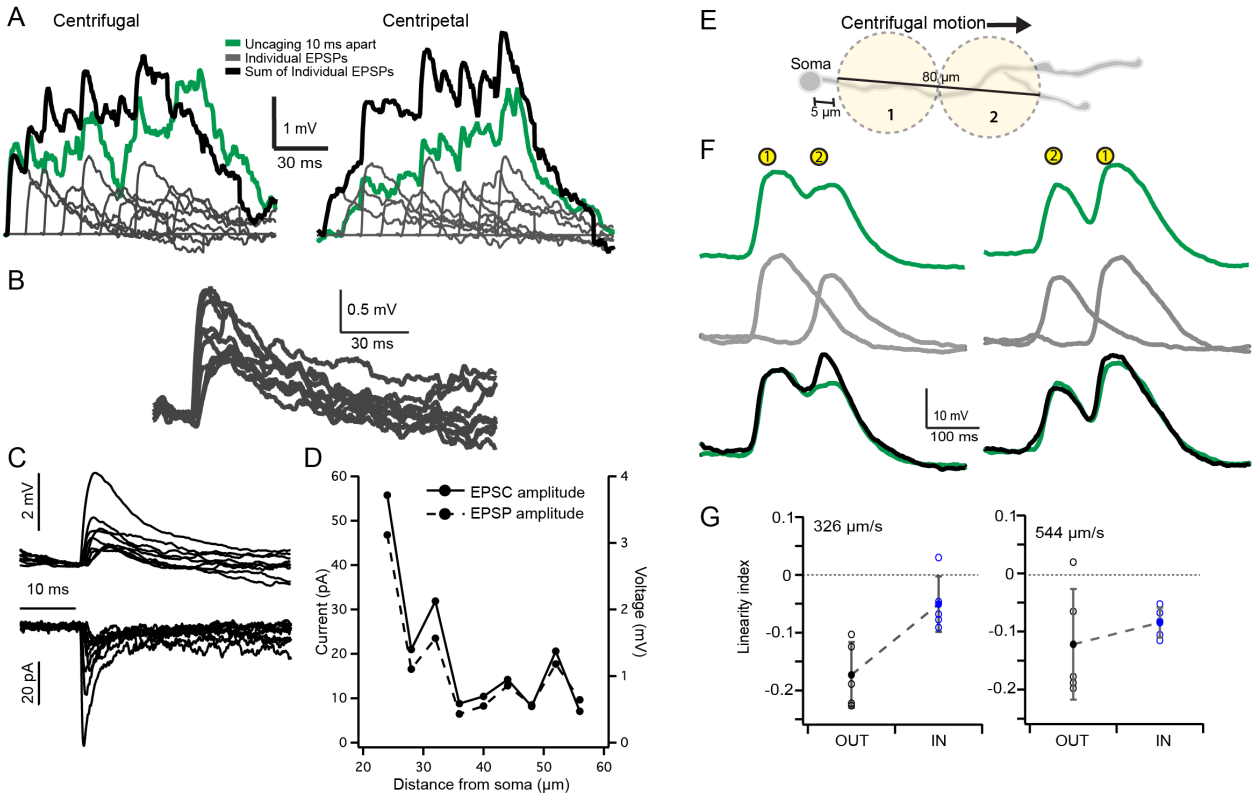

Figure 4.4 **Glutamatergic integration is more sublinear during outward apparent motion when measured from the soma.** A) Current clamp recordings of 10 uncaging-evoked EPSPs at sites 3 µm apart occurring individually (grey traces) or in sequence 10 ms apart (green trace). The sum of the individual grey traces is also plotted (black trace). B) The individual EPSPs from A aligned in time. C) Current clamp and voltage clamp recordings from the same 10 uncaging sites. D) Amplitudes of EPSPs and EPSCs from C as a function of distance from the soma. E) The approximate location of two light spots presented in sequence to simulate either outward (1 then 2) or inward (2 then 1) apparent motion over SAC dendrites while recording in current clamp from the soma. F) Green: Responses to apparent motion with velocity 503µm/s with spot numbers indicating the order of spot presentation either outward (left column) or inward (right column). Grey: response to spots presented individually, offset to align to the timing of the apparent motion sequence. Black: Sum of responses to individual spots. G) Linearity index for cells stimulated with outward vs. inward apparent motion stimuli. Open circle = individual cells, closed circle = mean. Error bars = SD. Index was computed by measuring the maximum amplitude of the summed response and comparing to the amplitude of the apparent motion trace at the same time. Positive = supralinear, negative = sublinear.

amplitude of currents recorded in voltage clamp for the same inputs are linearly correlated (Fig. 4.4C-D).

These results are distinct from what's been previously observed with somatic membrane potential using visual stimulation, in which an outward preference and supralinear responses have been observed under certain stimulus conditions (and have been used as a proxy for measuring DS signals in the distal dendrites in some cases) (Oesch and Taylor, 2010). To explore whether visual stimuli can evoke sublinear integration in a SAC, we used visual apparent motion stimuli with current clamp recordings (Fig. 4.4E). We found that both outward (centrifugal) and inward (centripetal) stimulation resulted in sublinearity of the maximum responses, with inward stimulation being less sublinear than outward stimulation at two different

velocities (Fig. 4.4F-G). Once again, this is consistent with passive integration of inputs, which would theoretically produce a centripetal preference at the soma.

SACs are known to contain voltage-gated conductances in addition to their passive elements. Because these results are different from what's been observed previously, it seems likely that voltage-gated conductances are contributing to the centrifugal preference observed at the soma in previous studies. However, because the samples sizes presented here are small, additional experiments are needed to verify these results. It would also be ideal to perform experiments in the presence of voltage-gated channel blockers and to determine precisely under what conditions the voltage-gated conductances become activated.

SAC release sites prefer outward motion at a large range of velocities

Apparent motion stimuli consist of presentation of spatially adjacent stimuli with varying time between presentation, which allows one to mimic a motion stimulus and vary the velocity of that stimulus. Mice are known to have a rather low flicker-fusion frequency (Nathan et al., 2006) and are thus likely to perceive apparent motion as motion at fairly slow velocities. Indeed, their DSGCs are direction selective at both low and high velocities(Trenholm et al., 2011), and a recent study showed that SACs are tuned across a wide range of velocities as well (Ding et al., 2016). Here, we confirmed the findings from Ding et al. (2016) using an apparent motion stimulus, which also allowed us to make several additional observations about SAC input integration.

To measure the velocity tuning of SACs' dendrites, we presented two stationary spots for a short amount of time (12.5 ms) (Fig. 4.5A) and recorded the calcium responses using 2-photon imaging of OGB-1 filled via patch pipet. We interlaid sequential stimulation of the two spots with varying time between spots (in order to mimic motion at different velocities) with presentation of each spot presented individually. Responses to the two spots presented individually showed that the response to the more proximal stimulation location resulted in a larger calcium transient at the end of the dendrite (Fig. 4.5B), as expected from our previous work (Vlasits et al., 2016). Sequential presentation of the two spots in the outward vs. inward direction resulted in a marked difference in the size of the calcium transient, with a clear preference for outward motion at a wide range of velocities (Fig. 4.5C-D). Thus, these stimuli appear to be sufficient to evoke similar physiological responses to an actual moving stimulus (i.e. Fig. 4.2). We calculated the direction selective index for a population of cells and found that the outward preference spanned from 200-1200 μm/s, and that there was also a preference for outward motion at the slowest speed tested (25 μm/s) (Fig. 4.5E).

One interesting feature of this dataset is that it corroborates the observations in Fig. 4.4 that, in some stimulus conditions, the SAC dendrite behaves quite sublinearly. In particular, looking at responses to inward apparent motion in Fig. 4.5C at 480 μm/s, it's noteworthy how much smaller the calcium transient is than the response to the proximal spot (spot 1 in Fig. 4.5A-B) on its own. In fact, the response to the proximal spot appears to be completely suppressed when preceded by the distal spot (spot 2 in Fig. 4.5A-B). Exploring the mechanism of this sublinear response would be an interesting avenue for further research. For instance, it may be the case that inhibitory inputs near the soma shunt the response. Inhibitory inputs are dense on the proximal dendrites, making this a likely possibility (Ding et al., 2016). Another possibility (not mutually-exclusive) is that some voltage-activated non-linearities are activated specifically in the outward direction, which are able to counteract the passive sublinearity of the dendrites

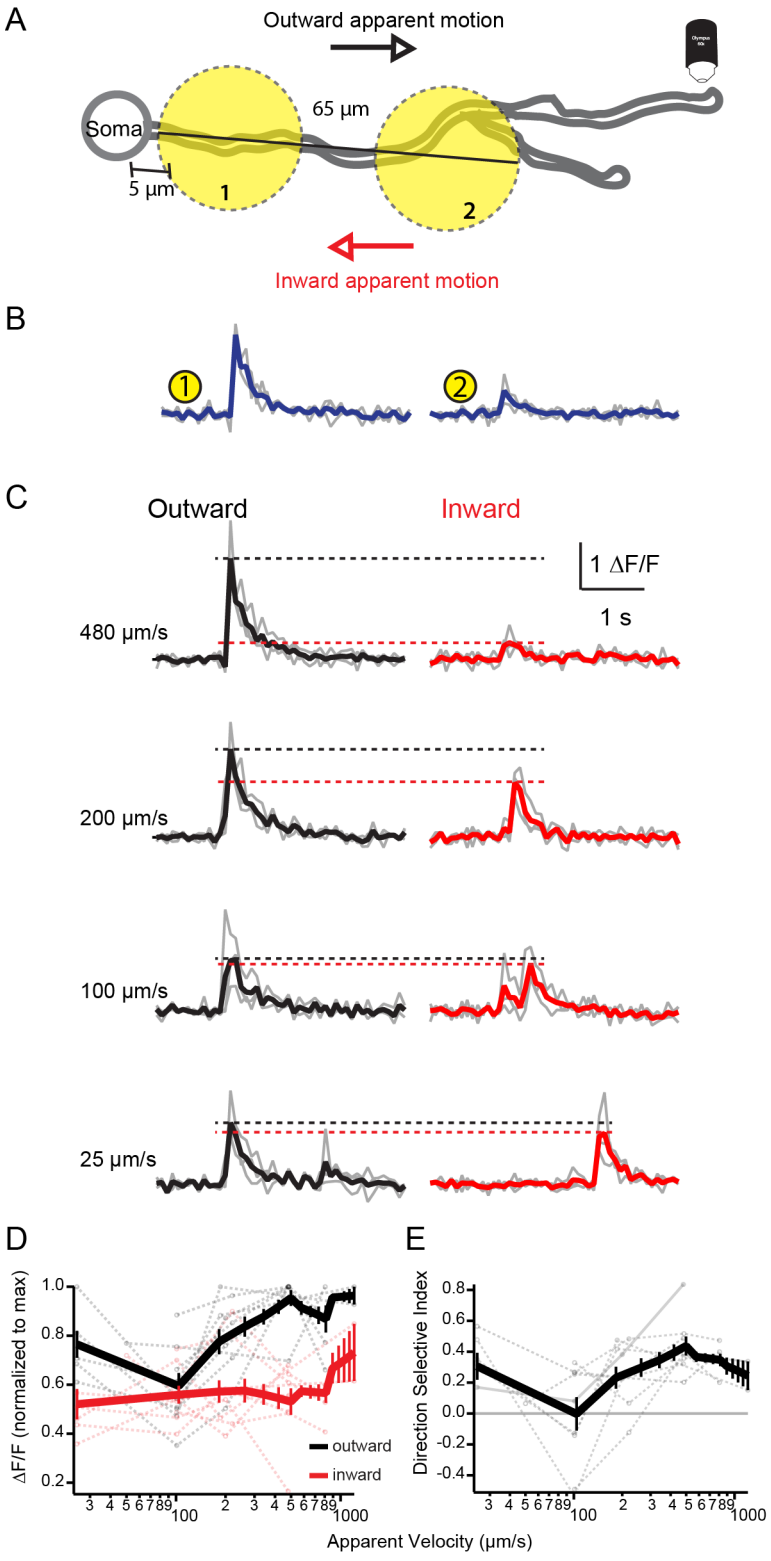

Figure 4.5 **SAC release sites prefer outward motion at a large range of velocities.** A) Schematic showing apparent motion stimulus used to measure velocity tuning of SAC release sites using calcium imaging of Oregon Green BAPTA-1 (OGB-1). Spots were presented either individually or in sequence in the outward direction (1 then 2) or the inward direction (2 then 1) for 12.5 ms each with varying time between spot presentation to change the apparent velocity. Spots were 25 µm diameter with 10 µm spacing in between them. Objective indicates location of 2-photon calcium imaging. Cells were filled with OGB-1 via patch pipet. B) Calcium transients in a SAC release site in response to spot 1 (left) and spot 2 (right) from A presented individually. Grey traces are individual trials and blue trace is the average of three trials. C) Calcium transients in response to outward (black) and inward (red) apparent motion at different apparent velocities for the same cell as in B. Grey traces are individual trials and thick traces are averages of three trials. Dotted lines indicate the peak response. D) Plot of the peak calcium response for each velocity normalized to the maximum calcium response as a function of apparent velocity for 8 regions of interest (ROIs) from 6 cells (dotted lines) on a log scale. Not all velocities were presented for all ROIs. Thick lines represent population averages for outward (black) and inward (red) apparent motion. E) Direction selective index for the responses from D (dotted lines) as a function of apparent velocity on a log scale. Index is [out – in]/[out], where positive is an outward preference and negative is an inward preference. Black trace is the average. Solid line indicates the example cell in B-C. Error bars are standard deviation.

(Fig. 4.4) and allow the response to approach linearity. This is also likely given the presence of such conductances in the SAC and the fact that at least some voltage-gated calcium channels are opening to produce release from the varicosities imaged here. Overall, this experiment is tantalizing as it suggests a method for dissecting the computational properties of SACs in fine detail, which could be used in conjunction with pharmacological or genetic manipulations to determine key non-linear components of the SAC dendrite's computational properties.

Bibliography

Abrahamsson, T., Cathala, L., Matsui, K., Shigemoto, R., and Digregorio, D.A. (2012). Thin dendrites of cerebellar interneurons confer sublinear synaptic integration and a gradient of short-term plasticity. Neuron 73, 1159–1172.

Ackert, J.M., Farajian, R., Volgyi, B., and Bloomfield, S.A. (2009). GABA blockade unmasks an OFF response in ON direction selective ganglion cells in the mammalian retina. J. Physiol. (Lond.) 587, 4481–4495.

Ala-Laurila, P., Greschner, M., Chichilnisky, E.J., and Rieke, F. (2011). Cone photoreceptor contributions to noise and correlations in the retinal output. Nat. Neurosci. 14, 1309–1316.

Amthor, F.R., Keyser, K.T., and Dmitrieva, N.A. (2002). Effects of the destruction of starburst-cholinergic amacrine cells by the toxin AF64A on rabbit retinal directional selectivity. Vis. Neurosci. 19, 495–509.

Applebury, M.L., Antoch, M.P., Baxter, L.C., Chun, L.L., Falk, J.D., Farhangfar, F., Kage, K., Krzystolik, M.G., Lyass, L.A., and Robbins, J.T. (2000). The murine cone photoreceptor: a single cone type expresses both S and M opsins with retinal spatial patterning. Neuron 27, 513–523.

Babai, N., and Thoreson, W.B. (2009). Horizontal cell feedback regulates calcium currents and intracellular calcium levels in rod photoreceptors of salamander and mouse retina. J. Physiol. (Lond.) 587, 2353–2364.

Baden T, Berens P, Bethge M, Euler T. (2013). Spikes in mammalian bipolar cells support temporal layering of the inner retina. Curr. Biol. 23(1):48--52

Bargmann, C.I., and Marder, E. (2013). From the connectome to brain function. Nat. Methods 10, 483–490.

Barlow HB, Hill RM. (1963). Selective sensitivity to direction of movement in ganglion cells of the rabbit retina. Science 139(3553):412--14

Barlow HB, Levick WR. (1965). The mechanism of directionally selective units in rabbit's retina. J. Physiol. 178(3):477--504

Beier, K.T., Borghuis, B.G., El-Danaf, R.N., Huberman, a. D., Demb, J.B., and Cepko, C.L. (2013). Transsynaptic Tracing with Vesicular Stomatitis Virus Reveals Novel Retinal Circuitry. J. Neurosci. 33, 35–51.

Berntson, A., and Taylor, W.R. (2000). Response characteristics and receptive field widths of on-bipolar cells in the mouse retina. J. Physiol. 524, 879–889.

Borg-Graham LJ. 2001. The computation of directional selectivity in the retina occurs presynaptic to the ganglion cell. Nat. Neurosci. 4(2):176--83

Borghuis, B.G., Marvin, J.S., Looger, L.L., and Demb, J.B. (2013). Two-photon imaging of nonlinear glutamate release dynamics at BC synapses in the mouse retina. J. Neurosci. 33, 10972–10985.

Borst A, Helmstaedter M. (2015). Common circuit design in fly and mammalian motion vision. Nat. Neurosci. 18(8):1067--76

Bos, R., Gainer, C., and Feller, M.B. (2016). Role for visual experience in the development of direction-selective circuits. Curr. Biol. 26, 1367–1375.

Breuninger, T., Puller, C., Haverkamp, S., and Euler, T. (2011). Chromatic BC pathways in the mouse retina. J. Neurosci. 31, 6504–6517.

Briggman, K.L., and Euler, T. (2011). Bulk electroporation and population calcium imaging in the adult mammalian retina. J. Neurophysiol. 105, 2601–2609.

Briggman, K.L., Helmstaedter, M., and Denk, W. (2011). Wiring specificity in the direction-selectivity circuit of the retina. Nature 471, 183–188.

Calderone, J.B., and Jacobs, G.H. (1995). Regional variations in the relative sensitivity to UV light in the mouse retina. Vis. Neurosci. 12, 463–468.

Carnevale, N.T., and Hines, M.L. (2006). The NEURON book (Cambridge, UK: Cambridge University Press).

Chen M, Lee S, Park SJH, Looger LL, Zhou ZJ. (2014). Receptive field properties of bipolar cell axon terminals in direction-selective sublaminas of the mouse retina. J. Neurophysiol. 112(8):1950--62

Chen, M., Lee, S., Park, S.J.H., Looger, L.L., and Zhou, Z.J. (2014). Receptive field properties of bipolar cell axon terminals in the direction-selective sublaminas of the mouse retina. J. Neurophysiol.

Chen, Q., Pei, Z., Koren, D., and Wei, W. (2016). Stimulus-dependent recruitment of lateral inhibition underlies retinal direction selectivity. Elife 5, e21053.

Cruz-Martín, A., El-Danaf, R.N., Osakada, F., Sriram, B., Dhande, O.S., Nguyen, P.L., Callaway, E.M., Ghosh, A., and Huberman, A.D. (2014). A dedicated circuit links direction-selective retinal ganglion cells to the primary visual cortex. Nature 507, 358–361.

Dalkara, D., Byrne, L.C., Klimczak, R.R., Visel, M., Yin, L., Merigan, W.H., Flannery, J.G., and Schaffer, D.V. (2013). In vivo-directed evolution of a new adeno-associated virus for therapeutic outer retinal gene delivery from the vitreous. Sci Transl Med 5, 189ra76.

Dalkara, D., Byrne, L.C., Lee, T., Hoffmann, N.V., Schaffer, D.V., and Flannery, J.G. (2012). Enhanced gene delivery to the neonatal retina through systemic administration of tyrosine-mutated AAV9. Gene Ther. 19, 176–181.

Deans, M.R., Volgyi, B., Goodenough, D.A., Bloomfield, S.A., and Paul, D.L. (2002). Connexin36 is essential for transmission of rod-mediated visual signals in the mammalian retina. Neuron 36, 703–712.

Denk, W., and Detwiler, P. (1999). Optical recording of light-evoked calcium signals in the funtionally intact retina. Proc. Natl. Acad. Sci. 96, 7035–7040.

DiGregorio, D.A., Rothman, J.S., Nielsen, T.A., and Silver, R.A. (2007). Desensitization properties of AMPA receptors at the cerebellar mossy fiber granule cell synapse. J. Neurosci. 27, 8344–8357.

Ding, H., Smith, R.G., Poleg-Polsky, A., Diamond, J.S., and Briggman, K.L. (2016). Species-specific wiring for direction selectivity in the mammalian retina. Nature 535, 105–110.

Dmitriev AV, Gavrikov KE, Mangel SC. (2012). GABA-mediated spatial and temporal asymmetries that contribute to the directionally selective light responses of starburst amacrine cells in retina. J. Physiol. 590(7):1699--720

Dvorak DR, Bishop LG, Eckert HE. 1975. On the identification of movement detectors in the fly optic lobe. J. Comp. Physiol. A. 100(1):5--23

Eagleman, D.M. (2001). Visual illusions and neurobiology. Nat. Rev. Neurosci. 2, 920–926.

Ekesten, B., and Gouras, P. (2005). Cone and rod inputs to murine retinal ganglion cells: evidence of cone opsin specific channels. Vis. Neurosci. 22, 893–903.

El-Husseini, A., Schnell, E., Chetkovich, D., Nicoll, R.A., and Bredt, D.S. (2000). PSD-95 involvement in maturation of excitatory synapses. Science (80-.). 290, 1364–1369.

Enroth-Cugell, C., and Shapley, R.M. (1973). Adaptation and dynamics of cat retinal ganglion cells. The Journal of Physiology 233, 271–309.

Euler, T., Detwiler, P.B., and Denk, W. (2002). Directionally selective calcium signals in dendrites of starburst amacrine cells. Nature 418, 845–852.

Exner S. (1894). Entwurf zu einer physiologischen Erklärung der psychischen Erscheinungen. I. Theil. Deuticke, Leipzig & Wien, pp. 179--202.

Famiglietti, E. V (1991). Synaptic organization of starburst amacrine cells in rabbit retina: analysis of serial thin sections by electron microscopy and graphic reconstruction. J. Comp. Neurol. 309, 40–70.

Farajian, R., Pan, F., Akopian, A., Volgyi, B., and Bloomfield, S.A. (2011). Masked excitatory crosstalk between the ON and OFF visual pathways in the mammalian retina. J. Physiol. (Lond.) 589, 4473–4489.

Farrow, K., Teixeira, M., Szikra, T., Viney, T.J., Balint, K., Yonehara, K., and Roska, B. (2013). Ambient illumination toggles a neuronal circuit switch in the retina and visual perception at cone threshold. Neuron 78, 325–338.

Flannery, J.G., and Visel, M. (2013). Adeno-associated viral vectors for gene therapy of inherited retinal degenerations. Methods Mol. Biol. 935, 351–369.

Fried, S.I., Münch, T. a, and Werblin, F.S. (2002). Mechanisms and circuitry underlying directional selectivity in the retina. Nature 420, 411–414.

Fried, S.I., Münch, T. a, and Werblin, F.S. (2005). Directional selectivity is formed at multiple levels by laterally offset inhibition in the rabbit retina. Neuron 46, 117–127.

Gao, F., Pang, J.-J., and Wu, S.M. (2013). Sign-preserving and sign-inverting synaptic interactions between rod and cone photoreceptors in the dark-adapted retina. J. Physiol. (Lond.) 591, 5711–5726.

Gavrikov, K.E., Dmitriev, A. V, Keyser, K.T., and Mangel, S.C. (2003). Cation-chloride cotransporters mediate neural computation in the retina. Proc. Natl. Acad. Sci. U. S. A. 100, 16047–16052.

Gavrikov, K.E., Nilson, J.E., Dmitriev, A. V, Zucker, C.L., and Mangel, S.C. (2006). Dendritic compartmentalization of chloride cotransporters underlies directional responses of starburst amacrine cells in retina. Proc. Natl. Acad. Sci. U. S. A. 103, 18793–18798.

Geffen, M.N., de Vries, S.E.J., and Meister, M. (2007). Retinal ganglion cells can rapidly change polarity from Off to On. PLoS Biology 5, e65.

Greene, M.J., Kim, J.S., and Seung, H.S. (2016). Analogous Convergence of Sustained and Transient Inputs in Parallel On and Off Pathways for Retinal Motion Computation. Cell Rep.

Grimes, W.N., Schwartz, G.W., and Rieke, F. (2014). The synaptic and circuit mechanisms underlying a change in spatial encoding in the retina. Neuron 82, 460–473.

Grimes, W.N., Zhang, J., Graydon, C.W., Kachar, B., and Diamond, J.S. (2010). Retinal parallel processors: more than 100 independent microcircuits operate within a single interneuron. Neuron 65, 873–885.

Hassenstein B, Reichardt W. (1956). Systemtheoretische Analyse der Zeit-, Reihenfolgen- und Vorzeichenauswertung bei der Bewegungsperzeption des Rüsselkäfers Chlorophanus. Z. Naturforsch. B. 11(9--10):513--24

Hausselt, S.E., Euler, T., Detwiler, P.B., and Denk, W. (2007). A dendrite-autonomous mechanism for direction selectivity in retinal starburst amacrine cells. PLoS Biol. 5, e185.

Helmstaedter, M., Briggman, K.L., Turaga, S.C., Jain, V., Seung, H.S., and Denk, W. (2013). Connectomic reconstruction of the inner plexiform layer in the mouse retina. Nature 500, 168–174.

Hoggarth, A., McLaughlin, A.J., Ronellenfitch, K., Trenholm, S., Vasandani, R., Sethuramanujam, S., Schwab, D., Briggman, K.L., and Awatramani, G.B. (2015). Specific Wiring of Distinct Amacrine Cells in the Directionally Selective Retinal Circuit Permits Independent Coding of Direction and Size. Neuron 86, 276–291.

Hubel DH. 1959. Single unit activity in striate cortex of unrestrained cats. J. Physiol. 147(2):226--38

Huberman, A.D., Wei, W., Elstrott, J., Stafford, B.K., Feller, M.B., and Barres, B.A. (2009). Genetic identification of an On-Off direction-selective retinal ganglion cell subtype reveals a layer-specific subcortical map of posterior motion. Neuron 62, 327–334.

Ivanova, E., Hwang, G.S., and Pan, Z.H. (2010). Characterization of transgenic mouse lines expressing Cre recombinase in the retina. Neuroscience 165, 233–243.

Ivanova, E., Lee, P., and Pan, Z.-H. (2013). Characterization of multiple bistratified retinal ganglion cells in a purkinje cell protein 2-Cre transgenic mouse line. J. Comp. Neurol. 521, 2165–2180.

Jackman, S.L., Choi, S.-Y., Thoreson, W.B., Rabl, K., Bartoletti, T.M., and Kramer, R.H. (2009). Role of the synaptic ribbon in transmitting the cone light response. Nature Neuroscience 12, 303–310.

Ke, J.-B., Wang, Y.V., Borghuis, B.G., Cembrowski, M.S., Riecke, H., Kath, W.L., Demb, J.B., and Singer, J.H. (2014). Adaptation to background light enables contrast coding at rod BC synapses. Neuron 81, 388–401.

Kim, J.S., Greene, M.J., Zlateski, A., Lee, K., Richardson, M., Turaga, S.C., Purcaro, M., Balkam, M., Robinson, A., Behabadi, B.F., et al. (2014). Space–time wiring specificity supports direction selectivity in the retina. Nature 509, 331–336.

Kochubey, O., Han, Y., and Schneggenburger, R. (2009). Developmental regulation of the intracellular Ca2+ sensitivity of vesicle fusion and Ca2+-secretion coupling at the rat calyx of Held. J. Physiol. 587, 3009–3023.

Kohn, A., and Movshon, J.A. (2004). Adaptation changes the direction tuning of macaque MT neurons. Nat. Neurosci. 7, 764–772.

Koizumi, A., Jakobs, T.C., and Masland, R.H. (2011). Regular mosaic of synaptic contacts among three retinal neurons. J. Comp. Neurol. 519, 341–357.

Kostadinov, D., and Sanes, J.R. (2015). Protocadherin-dependent dendritic self-avoidance regulates neural connectivity and circuit function. Elife 4, 1–23.

Lee, S., and Zhou, Z.J. (2006). The synaptic mechanism of direction selectivity in distal processes of starburst amacrine cells. Neuron 51, 787–799.

Lee, S., Kim, K., and Zhou, Z.J. (2010). Role of ACh-GABA cotransmission in detecting image motion and motion direction. Neuron 68, 1159–1172.

Lipin MY, Taylor WR, Smith RG. (2015). Inhibitory input to the direction-selective ganglion cell is saturated at low contrast. J. Neurophysiol. 114(2):927--41

Livingstone M, Hubel D. (1988). Segregation of form, color, movement, and depth: anatomy, physiology, and perception. Science. 240(4853):740--49

Magnus, C.J., Lee, P.H., Atasoy, D., Su, H.H., Looger, L.L., and Sternson, S.M. (2011). Chemical and genetic engineering of selective ion channel-ligand interactions. Science 333, 1292–1296.

Manookin, M.B., and Demb, J.B. (2006). Presynaptic mechanism for slow contrast adaptation in mammalian retinal ganglion cells. Neuron 50, 453–464.
Masland RH. (1969). Visual motion perception: experimental modification. Science 165(3895):819--21
Masland, R.H. (2012). The neuronal organization of the retina. Neuron 76, 266–280.
Morgan, J.L., and Kerschensteiner, D. (2012). Coating gold particles with DNA (biolistics). Cold Spring Harb. Protoc. 2012, 114–117.
Morgan, J.L., Schubert, T., and Wong, R.O.L. (2008). Developmental patterning of glutamatergic synapses onto retinal ganglion cells. Neural Dev. 3, 8.
Morrie, R.D., and Feller, M.B. (2015). An Asymmetric Increase in Inhibitory Synapse Number Underlies the Development of a Direction Selective Circuit in the Retina. J. Neurosci. 35, 9281–9286.
Morrie, R.D., and Feller, M.B. (2016). Development of synaptic connectivity in the retinal direction selective circuit. Curr. Opin. Neurobiol. 40, 45–52.
Münch, T. a, and Werblin, F.S. (2006). Symmetric interactions within a homogeneous starburst cell network can lead to robust asymmetries in dendrites of starburst amacrine cells. J. Neurophysiol. 96, 471–477.
Münch, T.A., da Silveira, R.A., Siegert, S., Viney, T.J., Awatramani, G.B., and Roska, B. (2009). Approach sensitivity in the retina processed by a multifunctional neural circuit. Nat. Neurosci. 12, 1308–1316.
Nathan, J., Reh, R., Ankoudinova, I., Ankoudinova, G., Chang, B., Heckenlively, J., and Hurley, J.B. (2006). Scotopic and photopic visual thresholds and spatial and temporal discrimination evaluated by behavior of mice in a water maze. Photochem. Photobiol. 82, 1489–1494.
Nikolaev, A., Leung, K.-M., Odermatt, B., and Lagnado, L. (2013). Synaptic mechanisms of adaptation and sensitization in the retina. Nat. Neurosci. 16, 934–941.
Nirenberg, S., and Meister, M. (1997). The light response of retinal ganglion cells is truncated by a displaced amacrine circuit. Neuron 18, 637–50.
Oesch N, Euler T, Taylor WR. (2005). Direction-selective dendritic action potentials in rabbit retina. Neuron 47(5):739--50
Oesch, N.W., and Taylor, W.R. (2010). Tetrodotoxin-resistant sodium channels contribute to directional responses in starburst amacrine cells. PLoS One 5, e12447.
Olveczky, B.P., Baccus, S.A., and Meister, M. (2007). Retinal adaptation to object motion. Neuron 56, 689–700.
Ozaita, A., Petit-Jacques, J., Völgyi, B., Ho, C.S., Joho, R.H., Bloomfield, S. a, and Rudy, B. (2004). A unique role for Kv3 voltage-gated potassium channels in starburst amacrine cell signaling in mouse retina. J. Neurosci. 24, 7335–7343.
Pang, J.-J., Gao, F., and Wu, S.M. (2012). Ionotropic glutamate receptors mediate OFF responses in light-adapted ON BCs. Vision Res. 68, 48–58.
Park, S.J.H., Kim, I.-J., Looger, L.L., Demb, J.B., and Borghuis, B.G. (2014). Excitatory synaptic inputs to mouse on-off direction-selective retinal ganglion cells lack direction tuning. J. Neurosci. 34, 3976–3981.
Pei, Z., Chen, Q., Koren, D., Giammarinaro, B., Acaron Ledesma, H., and Wei, W. (2015). Conditional Knock-Out of Vesicular GABA Transporter Gene from Starburst Amacrine Cells Reveals the Contributions of Multiple Synaptic Mechanisms Underlying Direction Selectivity in the Retina. J. Neurosci. 35, 13219–13232.

Petit-Jacques, J., Völgyi, B., Rudy, B., and Bloomfield, S. (2005). Spontaneous oscillatory activity of starburst amacrine cells in the mouse retina. J. Neurophysiol. 94, 1770–1780.

Poleg-Polsky A, Diamond JS. (2011). Imperfect space clamp permits electrotonic interactions between inhibitory and excitatory synaptic conductances, distorting voltage clamp recordings. PLoS ONE. 6(4):e19463

Poleg-Polsky A, Diamond JS. (2016a). Retinal circuitry balances contrast tuning of excitation and inhibition to enable reliable computation of direction selectivity. J. Neurosci. 36(21):5861--76

Poleg-Polsky A, Diamond JS. (2016b). NMDA receptors multiplicatively scale visual signals and enhance directional motion discrimination in retinal ganglion cells. Neuron 89(6):1277--90

Prange, O., Wong, T.P., Gerrow, K., Wang, Y.T., and El-Husseini, A. (2004). A balance between excitatory and inhibitory synapses is controlled by PSD-95 and neuroligin. Proc. Natl. Acad. Sci. 101, 13915–13920.

Priebe NJ, Ferster D. (2008). Inhibition, Spike Threshold, and Stimulus Selectivity in Primary Visual Cortex. Neuron. 57(4):482--97

Priebe, N.J., Lampl, I., and Ferster, D. (2010). Mechanisms of direction selectivity in cat primary visual cortex as revealed by visual adaptation. J. Neurophysiol. 104, 2615–2623.

Rall, W. (1964). Theoretical significance of dendritic trees for neuronal input-output relations. Neural Theory Model. 73–97.

Rall, W. (1967). Distinguishing theoretical synaptic potentials computed for different soma-dendritic distributions of synaptic input. J. Neurophysiol. 30, 1138–1168.

Rentería, R.C., Tian, N., Cang, J., Nakanishi, S., Stryker, M.P., and Copenhagen, D.R. (2006). Intrinsic ON responses of the retinal OFF pathway are suppressed by the ON pathway. J. Neurosci. 26, 11857–11869.

Rieke, F., and Rudd, M.E. (2009). The challenges natural images pose for visual adaptation. Neuron 64, 605–616.

Rivlin-Etzion, M., Wei, W., and Feller, M.B. (2012). Visual stimulation reverses the directional preference of direction-selective retinal ganglion cells. Neuron 76, 518–525.

Rosa, J.M., Morrie, R.D., Baertsch, H.C., and Feller, M.B. (2016). Contributions of Rod and Cone Pathways to Retinal Direction Selectivity Through Development. J. Neurosci. 36, 9683–9695.

Sagdullaev, B.T., McCall, M.A., and Lukasiewicz, P.D. (2006). Presynaptic inhibition modulates spillover, creating distinct dynamic response ranges of sensory output. Neuron 50, 923–35.

Sanes JR, Zipursky SL. 2010. Design principles of insect and vertebrate visual systems. Neuron 66(1):15--36

Schindelin, J., Arganda-Carreras, I., and Frise, E. (2012). Fiji: an open-source platform for biological-image analysis. Nat. Methods 9, 676–682.

Sethuramanujam S, McLaughlin AJ, deRosenroll G, Hoggarth A, Schwab DJ, Awatramani GB. (2016). A central role for mixed acetylcholine/GABA transmission in direction coding in the retina. Neuron 90(6):1243--56

Singer, J.H., Lassová, L., Vardi, N., and Diamond, J.S. (2004). Coordinated multivesicular release at a mammalian ribbon synapse. Nat. Neurosci. 7, 826–833.

Sivyer B, Williams SR. (2013). Direction selectivity is computed by active dendritic integration in retinal ganglion cells. Nat. Neurosci. 16(12):1848--56

Sivyer, B., van Wyk, M., Vaney, D.I., and Taylor, W.R. (2010). Synaptic inputs and timing underlying the velocity tuning of direction-selective ganglion cells in rabbit retina. J. Physiol. 588, 3243–3253.

Slaughter, M.M., and Miller, R.F. (1981). 2-amino-4-phosphonobutyric acid: a new pharmacological tool for retina research. Science 211, 182–185.

Stincic T, Smith RG, Taylor WR. (2016). Time course of EPSCs in ON-type starburst amacrine cells is independent of dendritic location. J. Physiol. 594(19):5685--94

Stoller, J.Z., Degenhardt, K.R., Huang, L., Zhou, D.D., Lu, M.M., and Epstein, J. a (2008). Cre reporter mouse expressing a nuclear localized fusion of GFP and beta-galactosidase reveals new derivatives of Pax3-expressing precursors. Genesis 46, 200–204.

Sun, L.O., Jiang, Z., Rivlin-Etzion, M., Hand, R., Brady, C.M., Matsuoka, R.L., Yau, K.-W., Feller, M.B., and Kolodkin, A.L. (2013). On and off retinal circuit assembly by divergent molecular mechanisms. Science (80-.). 342, 1241974.

Taylor WR, He S, Levick WR, Vaney DI. (2000). Dendritic computation of direction selectivity by retinal ganglion cells. Science 289(5488):2347--50

Taylor WR, Vaney DI. (2002). Diverse synaptic mechanisms generate direction selectivity in the rabbit retina. J. Neurosci. 22(17):7712--20

Taylor, W.R., and Smith, R.G. (2012). The role of starburst amacrine cells in visual signal processing. Vis. Neurosci. 29, 73–81.

Taylor, W.R., and Vaney, D.I. (2002). Diverse synaptic mechanisms generate direction selectivity in the rabbit retina. J. Neurosci. 22, 7712–7720.

Tjepkes DS, Amthor FR. (2000). The role of NMDA channels in rabbit retinal directional selectivity. Vis. Neurosci. 17(2):291--302

Torborg, C.L., and Feller, M.B. (2004). Unbiased analysis of bulk axonal segregation patterns. J. Neurosci. Methods 135, 17–26.

Trenholm S, McLaughlin AJ, Schwab DJ, Turner MH, Smith RG, et al. (2014). Nonlinear dendritic integration of electrical and chemical synaptic inputs drives fine-scale correlations. Nat. Neurosci. 17(12):1759--66

Trenholm, S., Johnson, K., Li, X., Smith, R.G., and Awatramani, G.B. (2011). Parallel mechanisms encode direction in the retina. Neuron 71, 683–694.

Tukker, J.J., Taylor, W.R., and Smith, R.G. (2004). Direction selectivity in a model of the starburst amacrine cell. Vis. Neurosci. 21, 611–625.

Vaney, D.I., Sivyer, B., and Taylor, W.R. (2012). Direction selectivity in the retina: symmetry and asymmetry in structure and function. Nat. Rev. Neurosci. 13, 194–208.

Veruki, M.L., and Hartveit, E. (2002). Electrical synapses mediate signal transmission in the rod pathway of the mammalian retina. J. Neurosci. 22, 10558–66.

Vessey, J.P., Lalonde, M.R., Mizan, H.A., Welch, N.C., Kelly, M.E., and Barnes, S. (2004). Carbenoxolone inhibition of voltage-gated Ca channels and synaptic transmission in the retina. J. Neurophysiol. 92, 1252–1256.

Vlasits, A.L., Bos, R., Morrie, R.D., Fortuny, C., Flannery, J.G., Feller, M.B., and Rivlin-Etzion, M. (2014). Visual Stimulation Switches the Polarity of Excitatory Input to Starburst Amacrine Cells. Neuron 83, 1172–1184.

Vlasits, A.L., Morrie, R.D., Tran-Van-Minh, A., Bleckert, A., Gainer, C.F., DiGregorio, D.A., and Feller, M.B. (2016). A Role for Synaptic Input Distribution in a Dendritic Computation of Motion Direction in the Retina. Neuron 89, 1317–1330.

Wang, Y.V., Weick, M., and Demb, J.B. (2011). Spectral and temporal sensitivity of cone-mediated responses in mouse retinal ganglion cells. J. Neurosci. 31, 7670–7681.

Wassle, H. (2004). Parallel processing in the mammalian retina. Nat. Rev. Neurosci. 5, 747–757.

Watanabe, D., Inokawa, H., Hashimoto, K., Suzuki, N., Kano, M., Shigemoto, R., Hirano, T., Toyama, K., Kaneko, S., Yokoi, M., et al. (1998). Ablation of Cerebellar Golgi Cells Disrupts Synaptic Integration Involving GABA Inhibition and NMDA Receptor Activation in Motor Coordination. Cell 95, 17.

Wei, W., and Feller, M.B. (2011). Organization and development of direction-selective circuits in the retina. Trends Neurosci. 34, 638–645.

Wei, W., Elstrott, J., and Feller, M.B. (2010). Two-photon targeted recording of GFP-expressing neurons for light responses and live-cell imaging in the mouse retina. Nat. Protoc. 5, 1347–1352.

Wei, W., Hamby, A.M., Zhou, K., and Feller, M.B. (2011). Development of asymmetric inhibition underlying direction selectivity in the retina. Nature 469, 402–6.Epub2010Dec5.

Werblin, F.S. (2010). Six different roles for crossover inhibition in the retina: correcting the nonlinearities of synaptic transmission. Vis. Neurosci. 27, 1–8.

Xu, H.., Zhao, J.., and Yang, X.. (2003). Cholinergic and dopaminergic amacrine cells differentially express calcium channel subunits in the rat retina. Neuroscience 118, 763–768.

Yonehara, K., Balint, K., Noda, M., Nagel, G., Bamberg, E., and Roska, B. (2011). Spatially asymmetric reorganization of inhibition establishes a motion-sensitive circuit. Nature 469, 407–410.

Yonehara, K., Farrow, K., Ghanem, A., Hillier, D., Balint, K., Teixeira, M., Jüttner, J., Noda, M., Neve, R.L., Conzelmann, K.-K., et al. (2013). The First Stage of Cardinal Direction Selectivity Is Localized to the Dendrites of Retinal Ganglion Cells. Neuron 79, 1078–1085.

Yoshida, K., Watanabe, D., Ishikane, H., Tachibana, M., Pastan, I., and Nakanishi, S. (2001). A Key Role of Starburst Amacrine Cells in Originating Retinal Directional Selectivity and Optokinetic Eye Movement. Neuron 30, 771–780.

Zheng, J., Lee, S., and Zhou, Z. (2004). A Developmental Switch in the Excitability and Function of the Starburst Network in the Mammalian Retina. Neuron 44, 851–864.